

A SEARCH FOR ASTROPHYSICAL ELECTRON ANTI-NEUTRINOS

AT KAMLAND

by

KEVIN SCOTT MCKINNY

A DISSERTATION

Submitted in partial fulfillment of the requirements
for the degree of Doctor in Philosophy in the
Department of Physics & Astronomy
in the Graduate School of
The University of Alabama

TUSCALOOSA, ALABAMA

2003

Copyright Kevin Scott McKinny 2003
ALL RIGHTS RESERVED

Submitted by Kevin Scott McKinny in partial fulfillment of the requirements
for the degree of Doctor of Philosophy specializing in Physics.

Accepted on behalf of the Faculty of the Graduate School by the dissertation
committee:

Louis J. Clavelli, Ph.D.

Anthony M. J. Davis, Ph.D.

William C. Keel, Ph.D.

Andreas Piepke, Dr. Rer. Nat.

Jerome K. Busenitz, Ph.D.
Chairperson

Date

Stan Jones, Ph.D.

Department Chairperson

Date

Ronald Rogers, Ph.D.

Dean of the Graduate School

ACKNOWLEDGMENTS

The efforts of many people have contributed to the work presented here. I would like to give great thanks and recognition to a select few who have been particularly influential on me and my work over the years leading to the completion of this thesis.

Let me begin by thanking my research advisor, Jerry Busenitz, who introduced me to neutrino physics as a member of the Palo Verde Neutrino Oscillation Experiment, and allowed me to follow him into the KamLAND Experiment. His knowledge, patience, and support were crucial to my ability to complete this work. I would like to also give special thanks to Andreas Piepke, for taking time to review my analyses on several occasions and providing valuable insight and correction.

I would like to thank Petr Vogel, Giorgio Gratta, and Bob Svoboda, for their encouragement and suggestions from the time this work was first proposed. I would also thank Yoshi Uchida, Glenn Horton-Smith, Patrick Dekowski, Karsten Heeger, Nikolai Tolich, and Jason Detwiler for their suggestions during the development of this analysis. I would also like to thank Brian Fujikawa, for his work on the statistical analysis of the data, and Sandip Pakvasa for his development of the theoretical interpretation of the results. Every member of the KamLAND collaboration touched this work in some way, and to each of them I am grateful.

Lastly, and most importantly, I would like to thank my wife, Jeanne, and our children, Caysi, C.J., and Scott, who have unselfishly made every sacrifice over the years to support me and have been endless sources of motivation. I never could have done it without them.

CONTENTS

ACKNOWLEDGMENTS	iii
LIST OF TABLES	vii
LIST OF FIGURES	ix
ABSTRACT	xv
1 INTRODUCTION	1
1.1 A Brief History of the Neutrino	1
1.2 Neutrino Properties	5
1.3 Astrophysical Electron Anti-Neutrinos	14
1.3.1 WIMP Annihilation Neutrinos	15
1.3.2 Relic Supernova Neutrinos	15
1.3.3 Electron Anti-Neutrinos from the Sun	17
2 DETECTOR	23
2.1 Detector Description	23
2.2 Trigger and Data Acquisition	24
2.3 Calibration	26
2.3.1 Source Deployment System	26
2.3.2 Gamma Sources	26
2.3.3 AmBe Source	27

2.3.4	Spallation Neutrons	28
2.3.5	Laser System	29
2.4	Monte Carlo Simulation	29
3	EVENT RECONSTRUCTION	32
3.1	Waveform Analysis	32
3.2	Vertex Reconstruction	33
3.3	Energy Estimation	36
4	ELECTRON ANTI-NEUTRINO DETECTION	43
4.1	Inverse Beta-Decay	43
4.1.1	Cross Section	44
5	HIGH ENERGY ELECTRON ANTI-NEUTRINO ANALYSIS	46
5.1	Events Selection	46
5.2	Background Estimates	48
5.2.1	Uncorrelated Background	49
5.2.2	Cosmogenic Backgrounds	51
5.2.3	Atmospheric Neutrinos	58
5.2.4	Reactor Neutrinos	59
5.2.5	Neutrons from Cosmic Muons	62
5.2.6	Summary of Backgrounds	70
5.3	Electron Anti-Neutrino Flux Calculation	70
5.3.1	$\bar{\sigma}$ Calculations	72
5.3.2	Detection Efficiency	73
5.3.3	Target Protons: $N_p \times f_v$	73
5.3.4	Experimental Livetime (T)	77
5.3.5	N_{signal}	77
5.3.6	Calculation of the Flux Limit	77

6	INTERPRETING THE FLUX LIMIT	85
7	CONCLUSIONS	87
A	WAVEFORM ANALYSIS	88
B	GAMMA CALIBRATION SOURCES	93
	BIBLIOGRAPHY	110

LIST OF TABLES

1.1	Flux of neutrinos on Earth from the solar pp-cycle and hep reaction.	6
1.2	Comparison of measured solar ν_e rates and rates predicted by the standard solar model [12]. Homestake, GALLEX, and SAGE rates are in units of events atoms ³⁶ s ⁻¹ (1 SNU), while Kamiokande, Super-Kamiokande, and SNO fluxes are given in units of 10 ⁶ cm ⁻² s ⁻¹ .	8
2.1	Summary of source energies used for the calibration of the KamLAND energy scale.	27
5.1	Data reduction for prompt energy between 8.0 MeV and 16.2 MeV.	47
5.2	High energy cosmogenic products.	50
5.3	Li ⁹ and He ⁸ delayed neutron β decays.	52
5.4	Muon shower rates for varying muon shower threshold energies. The coincidence probability indicates the probability that a real $\bar{\nu}_e$ event will be eliminated by the 2 second post shower cut, given the muon shower rate listed.	56
5.5	Fit parameters for neutron penetration in scintillator	66
5.6	Fit parameters for neutron penetration in scintillator	70
5.7	Summary of backgrounds for the solar $\bar{\nu}_e$ analysis, with prompt energies of 8.8 - 17.0 MeV, and higher energy analyses, with prompt energies of 17.0 - 30.0 MeV.	70

5.8	The ratio of the number of ^{12}B events inside the fiducial volume to the number of events inside the entire detector for various fiducial volume cuts. A value of the ratio of the observed to expected not equal to 1 indicates a bias in the vertex fitter.	75
5.9	Summary of quantities used in the calculation of the solar $\bar{\nu}_e$ flux and their uncertainties.	79
5.10	Example calculation of confidence level belt for a Poisson distribution of $\mu=0.5$, and background $b=3$ [44].	82
B.1	KamLAND γ sources (energies in keV).	95
B.2	Energy scale, resolution, and peak statistics (f_p) are compared for fit values and known values. The fit values shown were taken from a gaussian + 2^{nd} order polynomial, fit to the largest range studied.	100
B.3	University of Alabama sealed gamma sources. Energies are given in keV. Activities quoted are contained activities and were calibrated to $\pm 3\%$ at 95% C.L. on 1 July 2001 by AEA Technology.	100
B.4	NaI detector response for full absorption of gammas. Note that a different high voltage was used for the ^{65}Zn measurement.	102
B.5	Exposure time and counting times for the sealed sources. ^{60}Co and ^{137}Cs were exposed at different times to the same cell. The cell was counted only once.	106
B.6	Maximum leak rates for the KamLAND sealed gamma sources based on the Feldman & Cousins 95% C.L. interval for the gaussian amplitudes. For ^{60}Co , both peaks were fit and the sum was used.	107

LIST OF FIGURES

1.1	The energy spectrum of electrons emitted in the β -decay of tritium (^3H) [1].	3
1.2	The pp-cycle of solar fusion.	6
1.3	The spectra of solar neutrinos on Earth due to the solar pp-cycle and hep reaction, predicted by the Standard Solar Model.	7
1.4	The ratio of observed to expected number of events for reactor neutrinos. The dotted line indicated the prediction based on the oscillation parameters obtained from an analysis of solar neutrino data.	11
2.1	Schematic of the KamLAND Detector	23
2.2	The reconstructed energy spectrum for spallation neutrons throughout the KamLAND fiducial volume.	28
2.3	The simulated KamLAND geometry.	30
2.4	The simulated and measured ^{60}Co spectrum normalized to the number of events in the full absorption peaks. The heavy solid line is the measured spectrum, and the grey filled area is the simulated spectrum.	31
2.5	The neutron capture time for the GEANT3 simulation. The mean capture time is 200 μs	31
3.1	From top to bottom: Raw waveform, pedestal waveform, pedestal subtracted waveform, pedestal subtracted renormalized and smoothed waveform. The x-axis is time bins (~ 1.5 ns/bin), and the y-axis is ADC counts.	34

3.2	Vertical lines indicate the t_1 , t_2 , and tof_q found for a PMT waveform.	35
3.3	Performance of the Diamond Time Fitter as a function of z-position for ^{60}Co . Error bars indicate the width of the distributions, which include detector position resolution and the effects of the mean free path of ^{60}Co γ 's in scintillator.	36
3.4	The positron energy scale function obtained from Monte Carlo simulation.	40
3.5	The gamma ray energy scale function obtained from Monte Carlo simulation.	41
3.6	^{60}Co source energy reconstruction for positions along the z-axis of the detector.	42
3.7	The energy reconstruction for ^{12}B decays in the KamLAND scintillator [34]. The solid line represents the results over the region included in the fit, while the dotted line represents an extrapolation of the fit function.	42
4.1	The cross section for inverse beta decay.	45
5.1	$\bar{\nu}_e$ candidate events with all cuts applied except the prompt and delayed energy cuts. The dark grey region, which contains one event, represents the region of interest to the search for $\bar{\nu}_e$'s from ^8B ν_e transitions. The light grey area represents the region of interest to the study of relic super nova $\bar{\nu}_e$'s and $\bar{\nu}_e$'s from WIMP annihilation. The cluster of events below 8.0 MeV are reactor $\bar{\nu}_e$'s.	48
5.2	The decay schemes for ^8He and ^9Li .	52
5.3	The left panel shows the prompt energy deposited by events that have been tagged as ^9Li or ^8He events in the scintillator. The right panel shows the energy spectrum of the delayed neutron capture, with the characteristic 2.2 MeV peak.	53
5.4	The time since muon shower distribution for events occurring within 2 seconds after a muon shower.	54

5.5	The prompt energy deposit from the β -decay of cosmogenics. A qualitative comparison of the data to expected ${}^9\text{Li}$ and ${}^8\text{He}$ spectra suggests the signal in KamLAND is primarily due to ${}^9\text{Li}$ decays. .	55
5.6	The time difference between muons and singles events with energies between 8 MeV and 20 MeV is fit to determine decay constant for the distribution of muon/ $\bar{\nu}_e$ time differences.	57
5.7	${}^9\text{Li}$ and $\bar{\nu}_e$ events as a function of muon shower threshold. The dotted line indicates a linear fit to the ${}^9\text{Li}$ curve, and has a y-intercept of 45.61 events.	58
5.8	The flux of atmospheric $\bar{\nu}_e$'s at the Kamioka site. Error bars represent the 20% uncertainty in the flux normalization, and do not include model uncertainties.	60
5.9	The reactor $\bar{\nu}_e$'s spectrum at KamLAND assuming LMA oscillations. The log scale is used in order to visualize the the extremely small signal above 8.8 MeV.	61
5.10	The background expected above the anti-neutrino energy of 8 MeV from reactor $\bar{\nu}_e$'s at KamLAND as a function of neutrino mixing parameters.	62
5.11	The background expected above the prompt energy of 8 MeV from reactor $\bar{\nu}_e$'s at KamLAND, histogrammed for the entire range of mixing parameters. The mean of the distribution is taken as the expected background contribution. An error is assigned which includes the entire range of possible background values.	63
5.12	Penetration into scintillator for neutrons generated in water. The fit results shown are for a simple $\exp(\text{constant} + \text{slope} \times x)$	65
5.13	The calculated number of events inside the 550 cm fiducial volume, for 20 million events generated in water.	67
5.14	Penetration into scintillator for neutrons generated in rock. The fit results shown are for a simple $\exp(\text{constant} + \text{slope} \times x)$	69
5.15	The calculated number of events inside the 550cm fiducial volume, for 40 million events generated in rock.	71

5.16	The detection efficiency for inverse beta decay in KamLAND as a function of positron energy. The dotted line represents the average value, and the grey region indicates the uncertainty.	74
5.17	Event distributions in r^3 , $\cos\theta$, and ϕ for ^{12}B decays in the scintillator. The solid lines represent all events, dotted lines are backgrounds, and points with error bars are all events minus backgrounds [34].	76
5.18	Points indicate the Feldman & Cousins 90% C.L. upper limit on number of signal events for one observed event in the presence of known background. The line represents a fit to a second order polynomial which is used to interpolate to this studies values of the expected background.	78
5.19	Histogram showing the flux limits obtained in 100,000 simulated measurements. The line at $1111 \text{ cm}^{-2} \text{ s}^{-1}$ indicates the value for which 90% of the experiments measure a smaller value.	80
5.20	90% confidence belts for the solar $\bar{\nu}_e$ calculated according to the method of Ref. [44], with statistical uncertainties included according to Ref. [45] and Ref. [46]. The observation of one events leads to an upper limit on the $\bar{\nu}_e$ flux of $\Phi_{\bar{\nu}_e} \leq 9.4 \times 10^2 \text{ cm}^{-2} \text{ s}^{-1}$. . .	84
A.1	The residual bias due to the pedestal renormalization scheme used in the KamLAND waveform analysis.	91
A.2	The relative contribution of individual pulses within a waveform to the sum of all positive pulses.	92
B.1	Cutaway view of source capsule. Dimension units are mm.	97
B.2	Spectra of KamLAND gamma sources.	98
B.3	The ^{137}Cs peak is fit with a gaussian, while the background is fit to a 2nd order polynomial. In this study, 2nd and 3rd order polynomials were used to fit the background, and the range of the fit was varied.	101

B.4	Leak test experimental setup. A The setup is the same for both the coincidence and non-coincidence measurements, although no scintillator data is taken for the ^{65}Zn measurement.	102
B.5	The ^{60}Co spectrum was fit to a gaussian + gaussian + 1st order polynomial in order to find the center and width of the absorption lines.	103
B.6	The energy response of the liquid scintillator cells for backscattered 511 keV, 662 keV, and 1332 keV gammas with compton edges at 341 keV, 478 keV, and 1118.1 keV, respectively.	104
B.7	The NaI fit to search for ^{137}Cs decays. P1 is the amplitude of the gaussian, P2 and P3 are coefficients of the polynomial intended to fit the background.	105
B.8	The NaI fit to search for ^{60}Co decays. P1 is the amplitude of the first gaussian, P2 is the amplitude of the second gaussian, P3 and P4 are coefficients of the polynomial intended to fit the background.	106
B.9	The unexpected peak a 159 keV.	108
B.10	The energy spectrum is fit with a gaussian with center and width fixed to the known values of ^{137}Cs	109
B.11	The background energy spectrum is fit with a gaussian with center and width fixed to the known values of ^{137}Cs	109

ABSTRACT

A search has been carried out using 149 days of data taken between March, 2003, and December, 2003, at the KamLAND detector for a flux of astrophysical anti-neutrinos due to Supernova Relic Neutrinos (SRN), and solar $\bar{\nu}_e$ resulting from the transformation of ^8B ν_e 's into $\bar{\nu}_e$'s through the process of Spin Flavor Precession (SFP) or neutrino decay. A search for the SRN $\bar{\nu}_e$ flux in the range of 16.2 - 30 MeV yielded zero candidates, where $1.72 \pm .12$ are expected from background. An upper limit is placed on the flux of SRN $\bar{\nu}_e$ of $74 \text{ cm}^{-2} \text{ s}^{-1}$ in the energy range of 16.2 - 30 MeV. This limit does not compete with the current limit of $1.2 \text{ cm}^{-2} \text{ s}^{-1}$ reported by the Super-Kamiokande Experiment. The search for solar $\bar{\nu}_e$'s resulted in one candidate event in the energy range of 8.0 - 16 MeV, where the signal from background is expected to $0.94 \pm .45$ events. The results are consistent with no signal, and an upper limit on the solar $\bar{\nu}_e$ flux between 8.0 and 16.2 MeV is found to be $9.4 \times 10^2 \text{ cm}^{-2} \text{ s}^{-1}$, which corresponds to a transition probability of 0.00077 for $\nu_e \rightarrow \bar{\nu}_e$, assuming no spectral deformation. This value improves by a factor of 10 on the previous limit of 0.008 obtained by the Super-Kamiokande Experiment. The new limit is used to further improve on the current limits for the product of the neutrino magnetic moment with the transverse solar magnetic field, and the neutrino lifetime for non-radiative decays.

CHAPTER 1

INTRODUCTION

The study of neutrino physics represents one of the most challenging fields of high energy experimental physics today. The ghostly character of the neutrino makes studying its properties exceedingly difficult. To compensate for this difficulty, very large detectors, with target masses ranging from a few tons to 50 metric kilo-tons (50,000,000 kg) have been constructed deep underground in sites around the world. In neutrino physics, the focus of these large detectors has been to determine the mass and mixing characteristics of the neutrino; however, other properties, such as the Majorana or Dirac nature of neutrinos, the magnetic moment and lifetime of the neutrino can also be studied by analyzing neutrino data.

1.1 A Brief History of the Neutrino

Beta (β) -decay is the process by which unstable nuclei decay by emission of an electron or positron, changing the atomic number by one unit (see eq. 1.1), while conserving charge. In this notation, (A,Z) represents the parent nucleus, atomic number A , and proton number Z . $(A,Z\pm 1)$ is referred to as the daughter nucleus.

$$(A, Z) \rightarrow (A, Z \pm 1) + e^{\mp} \quad (1.1)$$

For example, a free neutron decays into a proton with the emission of an electron as shown in 1.2.

$$n \rightarrow p + e^{-} \quad (1.2)$$

This picture of β -decay is, of course, incomplete, since lepton number is not conserved in equations 1.1 and 1.2. In the 1920's, however, particle physics had not advanced to the point where Lepton number conservation was known. Nevertheless, it was known that there was a problem with the theory of β -decay. Equation 1.1 is a illustration of a simple two-body decay. When the nucleus decays at rest, conservation of momentum requires that the daughter nucleus and the electron (or positron) are produced back-to-back with equal momenta:

$$\vec{p}_{daughter} + \vec{p}_e = \vec{p}_{parent} = 0 \quad (1.3)$$

$$\vec{p}_{daughter} = -\vec{p}_e \quad (1.4)$$

Since the mass of the daughter nucleus is always thousands of times that of the electron, it is reasonable to approximate the mass of the parent and daughter nuclei are infinite. In this approximation, the daughter carries away all the kinetic energy of the decay, and the conservation of energy fixes the energy of the electron:

$$E_e = M_{parent} - M_{daughter} \quad (1.5)$$

where M denotes the particle masses and E is the total energy. The energy of the electron is, therefore, equal to the mass difference between the parent and daughter nuclei (Δ).

According to this model, the β -decay of a nucleus should produce mono-energetic electrons; however, the measured spectrum of electron energies from β -decay is a continuum with an upper limit (or endpoint) equal to the mass

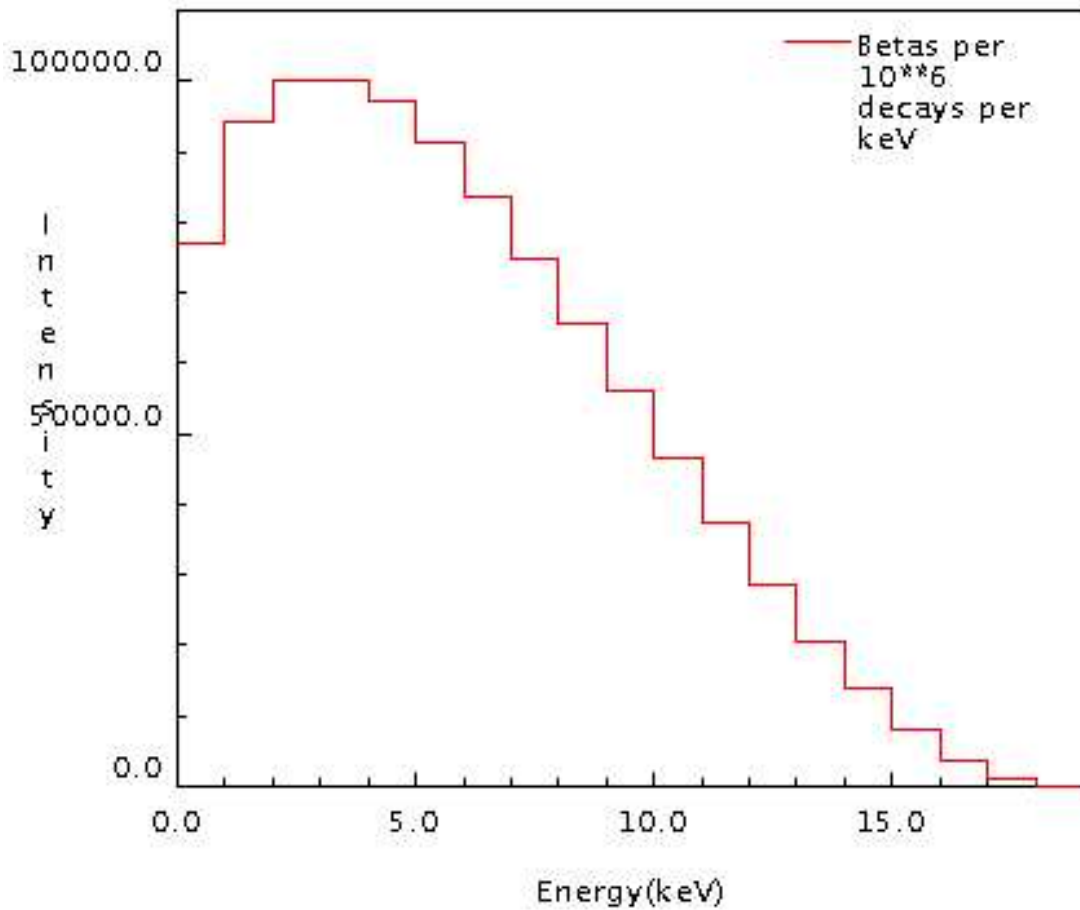


FIG. 1.1.: The energy spectrum of electrons emitted in the β -decay of tritium (^3H) [1].

difference of the parent and daughter nuclei. Figure 1.1 shows the true energy spectrum for electrons emitted in tritium decay.

One famous explanation of the continuous β spectrum was proposed by Niehls Bohr, who suggested that energy is not conserved exactly in subatomic processes. Wolfgang Pauli, eager to save the principle of conservation of energy, suggested another possible explanation for the observed energy spectrum. In a letter dated December 4th, 1930, Pauli proposed that in the β -decay of nuclei, in addition to the electron, a light particle with no charge is also emitted. This new particle was dubbed the “neutron” by Pauli, but was later renamed “neutrino” (little neutral

one) by Enrico Fermi in his model of weak interactions. In weak interaction theory, the range of the weak force is a very small fraction of the radius of a nucleon (neutron or proton); therefore, the interaction probability is very small. The addition of the neutrino (ν) and its antiparticle ($\bar{\nu}$) lead to following expressions for β -decay of the neutron and proton:

$$n \rightarrow p + e^- + \bar{\nu} \quad (1.6)$$

$$p \rightarrow n + e^+ + \nu. \quad (1.7)$$

The inverse reactions

$$\bar{\nu} + p \rightarrow n + e^+ \quad (1.8)$$

$$\nu + n \rightarrow p + e^- \quad (1.9)$$

are also allowed, and serve as means of detecting neutrinos. In 1955, Fred Reines and Clyde Cowan built an neutrino detector at the Savannah River nuclear power plant, which produced a flux of 10^{13} ν 's $\text{cm}^{-2} \text{s}^{-1}$. The large flux of neutrinos was necessary to their detection since the interaction cross section for these reactions is on the order of 10^{-42} cm^2 . The detector consisted of CdCl_2 dissolved in water. The hydrogen nuclei in water served as a target for the $\bar{\nu} + p \rightarrow n + e^+$ reaction, while the CdCl_2 captured the neutron. Scintillation counters detected the energy of the annihilation of the e^+ , followed microseconds later by the release of energy accompanying the capture of the neutron. The neutrino signal obtained was correlated with the operation of the reactor, and in 1956 the detection of the neutrino was announced [2].

In the 1930's, the muon (μ) was discovered. Like the electron, the muon was found to participate in electromagnetic and weak interactions, but not in the strong interactions (which are forces that bind nuclei). Unlike the electron, the

muon is unstable, and decays into an electron and what we now know to be two neutrinos with an average lifetime of about $\sim 10^{-6}$ s. Muons are produced by the decay of pions according to the reaction:

$$\pi^+ \rightarrow \mu^+ + \nu. \quad (1.10)$$

Neutrinos resulting from this decay were collided with neutrons in an effort to produce both muons and electrons. Only muons were found to result from the collisions [3]. It was determined that these results could be explained if there are two types of neutrinos: a type that couples only to electrons, denoted ν_e , and a type that couples only to muons, denoted ν_μ , and their antiparticles $\bar{\nu}_e$ and $\bar{\nu}_\mu$.

In 1977, the third lepton, called the tau, or τ , was discovered, and the existence of its neutrino partner, the ν_τ was inferred. Measurements of the decay width of the Z-boson [4] and astrophysical measurements [5] suggest that there are no light neutrinos beyond the three known flavors and their anti-matter counterparts.

1.2 Neutrino Properties

Despite the fact that the neutrino has been studied for several decades, very little is known about its fundamental properties. For example, the mass of the neutrino, its magnetic moment, and its Dirac or Majorana nature all remain unanswered.

Attempts to measure the mass of the neutrino directly through the analysis of the endpoint of Tritium β -decay, and observations of the neutrino signal from super nova 1987A have resulted in upper limits on the mass, which cannot exclude the possibility of massless neutrinos; however, the question of the existence of massive neutrinos became fundamental to the understanding of Solar physics, as well as neutrino physics, after the measurement of the flux of electron neutrinos from the sun at several detectors around the world.

Source	E_{ν}^{max} (MeV)	Flux ($10^{10} \text{ cm}^{-2} \text{ s}^{-1}$)
pp	0.42	5.95
^7Be	0.86	0.480
	0.36	
^8B	14.06	5.15×10^{-4}
hep	18.8	9.3×10^{-7}

TABLE 1.1.: Flux of neutrinos on Earth from the solar pp-cycle and hep reaction.

According to the Standard Solar Model (SSM), solar energy is produced by the conversion of fusion of protons in to ^4He , and 98% of these reactions occur through the pp-cycle, which is illustrated in Fig. 1.2. Neutrinos are also produced by the reaction $^3\text{He} + p \rightarrow ^4\text{He} + e^+ + \nu_e$ (called “hep”), at a rate many orders of magnitude below the pp-cycle neutrino rate. The resulting solar neutrino spectra are shown in Fig. 1.3, with the absolute fluxes given in Table 1.1.

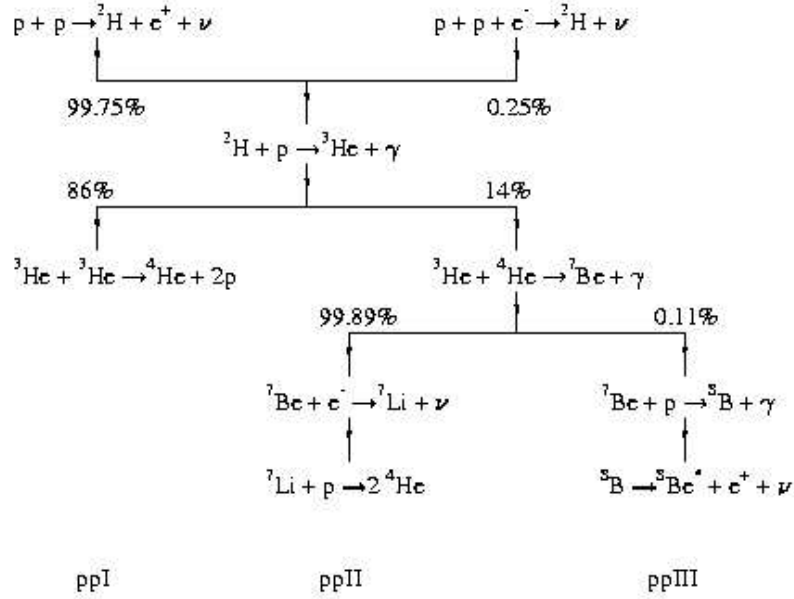


FIG. 1.2.: The pp-cycle of solar fusion.

The solar neutrino flux detected on Earth was found to be roughly 50% of the flux predicted by the SSM (see Table 1.2). This effect became known as the

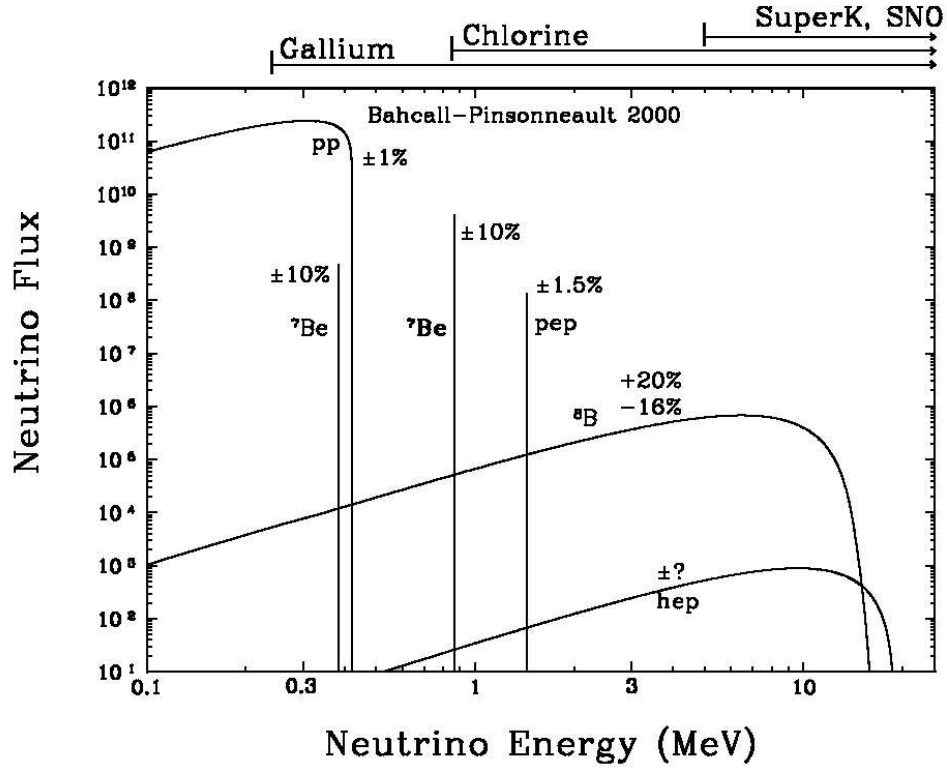


FIG. 1.3.: The spectra of solar neutrinos on Earth due to the solar pp-cycle and hep reaction, predicted by the Standard Solar Model.

“Solar Neutrino Problem”. Due to the success of the SSM at predicting other solar quantities, the prediction was believed to be accurate.

Further evidence of interesting neutrino physics was found in measurements of the atmospheric neutrino flux. Neutrinos are produced in the atmosphere from the decay of pions and kaons, which are themselves produced by the cosmic ray interactions with the atmosphere. Equation 1.11 shows the decay chain leading to neutrino production for positive kaons.

$$N_{cr} + N_{air} \rightarrow \pi^{\pm}, K^{\pm}, K^0, \dots$$

$$K^+ \rightarrow \mu^+ + \nu_{\mu}, \pi^+ + \pi^0$$

	Measured Rate	Expected Rate [12]	Measured/Expected
Homestake [6]	2.56 ± 0.23	$7.6^{+1.3}_{-1.1}$	0.34 ± 0.002
Gallex [7]	$74.1^{+7.8}_{-6.7}$	128^{+9}_{-7}	$0.58^{+0.070}_{-0.064}$
Sage [8]	$75.4^{+7.8}_{-7.4}$	128^{+9}_{-7}	0.59 ± 0.07
Kamiokande [9]	2.80 ± 0.39	$5.05^{+1.01}_{-0.81}$	$0.55^{+0.13}_{-0.12}$
Super-Kamiokande [10]	2.32 ± 0.07	$5.05^{+1.01}_{-0.81}$	$0.46^{+0.09}_{-0.07}$
SNO [11]	2.39 ± 0.81	$5.05^{+1.01}_{-0.81}$	$0.47^{+0.12}_{-0.11}$

TABLE 1.2.: Comparison of measured solar ν_e rates and rates predicted by the standard solar model [12]. Homestake, GALLEX, and SAGE rates are in units of events atoms³⁶ s⁻¹ (1 SNU), while Kamiokande, Super-Kamiokande, and SNO fluxes are given in units of 10⁶ cm⁻² s⁻¹.

$$\begin{aligned}
\pi^+ &\rightarrow \mu^+ + \nu_\mu \\
\mu^+ &\rightarrow e^+ + \nu_e + \bar{\nu}_\mu \\
&etc.
\end{aligned}
\tag{1.11}$$

The decays leading to production of the neutrinos in the atmosphere are expected to produce approximately twice as many muon neutrinos as electron neutrinos according to current atmospheric neutrino production models; however measurements of the ratio of muon neutrinos to electron neutrinos in the atmospheric neutrino flux was found to be closer to 1:1 than 2:1 [13, 14]. This discrepancy became known as the ‘‘Atmospheric Neutrino Anomaly’’.

The solution to the Solar Neutrino Problem and Atmospheric Neutrino Anomaly lies in the theory of neutrino flavor oscillations. In oscillation theory, the three neutrino flavors, ν_e , ν_μ , and ν_τ , are actually linear combinations of three mass eigenstates ν_1 , ν_2 , and ν_3 , with masses m_1 , m_2 , and m_3 , respectively. The mixing of mass eigenstates into flavor eigenstates can be described in terms of a 3×3 unitary mixing matrix (U) as:

$$\begin{pmatrix} \nu_e \\ \nu_\mu \\ \nu_\tau \end{pmatrix} = U \begin{pmatrix} \nu_1 \\ \nu_2 \\ \nu_3 \end{pmatrix}
\tag{1.12}$$

where,

$$U = \begin{pmatrix} c_{12}c_{13} & s_{12}c_{13} & s_{13}e^{i\delta_{13}} \\ -s_{12}c_{23} - c_{12}s_{23}s_{13}e^{i\delta_{13}} & c_{12}c_{23} - s_{12}s_{23}s_{13}e^{i\delta_{13}} & s_{23}c_{13} \\ s_{12}s_{23} - c_{12}c_{23}s_{13}e^{i\delta_{13}} & -c_{12}s_{23} - s_{12}c_{23}s_{13}e^{i\delta_{13}} & c_{23}s_{13} \end{pmatrix} \quad (1.13)$$

where c_{ij} and s_{ij} are shorthand for $\cos\theta_{ij}$ and $\sin\theta_{ij}$, respectively, and θ_{ij} is referred to as the mixing angle between mass eigenstates i and j . If the three mass eigenstates have different masses, they will have different wavelengths. As the neutrino propagates through space, the relative contribution of the three mass eigenstates will change, resulting in a decrease in the flux of neutrinos of a particular flavor.

The effect of neutrino oscillation can be more easily illustrated using the two-flavor mixing scenario. In two flavor mixing, the above expression can be written:

$$\begin{pmatrix} \nu_e \\ \nu_\mu \end{pmatrix} = \begin{pmatrix} \cos\theta & \sin\theta \\ -\sin\theta & \cos\theta \end{pmatrix} \begin{pmatrix} \nu_1 \\ \nu_2 \end{pmatrix} \quad (1.14)$$

The wave function for an electron neutrino at the time of its production in the sun can be written as:

$$|\psi(t=0)\rangle = |\nu_e\rangle = \cos\theta|\nu_1\rangle + \sin\theta|\nu_2\rangle, \quad (1.15)$$

and the wave-function for a muon neutrino can be written:

$$|\nu_\mu\rangle = -\sin\theta|\nu_1\rangle + \cos\theta|\nu_2\rangle, \quad (1.16)$$

The mass eigenstates are the eigenstates of the Hamiltonian, and therefore propagate through time (and space) according to:

$$|\psi(t)\rangle = \cos\theta|\nu_1\rangle e^{-iE_1t} + \sin\theta|\nu_2\rangle e^{-iE_2t}, \quad (1.17)$$

where

$$E_i = \sqrt{p^2 + m_i^2} \simeq p + \frac{m_i^2}{2E_i}, \quad (1.18)$$

where $i=1,2$ and assuming that neutrinos are light with mass eigenstates created with equal momenta, p . These results are presented in “natural units”, where $\hbar = c = 1$, and the speed of the neutrino is assumed to be nearly c , so $x \simeq ct = t$.

The probability that an electron neutrino becomes a muon neutrino is given by the square of the inner product of 1.16 and 1.17, which can be expressed as:

$$P(\nu_e \rightarrow \nu_\mu) = \sin^2 2\theta \sin^2 \left(1.27 \frac{\Delta m^2 (\text{eV}^2) L (\text{m})}{E (\text{MeV})} \right), \quad (1.19)$$

where Δm^2 is the difference in the squared masses of the two mass eigenstates in eV^2 , L is the distance between the point of production and the point of detection in meters, and E is the neutrino energy in MeV.

The results of solar neutrino flux measurements, which are summarized in Table 1.2, are consistent with neutrino oscillations for values of $\sin^2 2\theta \simeq 0.83$ and $\Delta m^2 \simeq 5.5 \times 10^{-5} \text{ eV}^2$. This solution for the solar neutrino problem has been verified under laboratory conditions using a known source of reactor $\bar{\nu}_e$'s at the KamLAND experiment [15]. KamLAND measured the flux of neutrinos from reactors at an average distance of 180 km. The measured flux was consistent with that expected if $\bar{\nu}_e$'s oscillate with the mixing angle and Δm^2 predicted by the solar neutrino problem. Figure 1.4 shows the results of KamLAND, as well as other reactor neutrino experiments, plotted with the predicted reactor neutrino flux given neutrino oscillations with parameters given by the solar neutrino solution.

The atmospheric neutrino anomaly is identified by calculating the double ratio of ν_μ to ν_e , which is defined as:

$$R = \frac{(\nu_\mu/\nu_e)_{\text{observed}}}{(\nu_\mu/\nu_e)_{\text{predicted}}}, \quad (1.20)$$

and

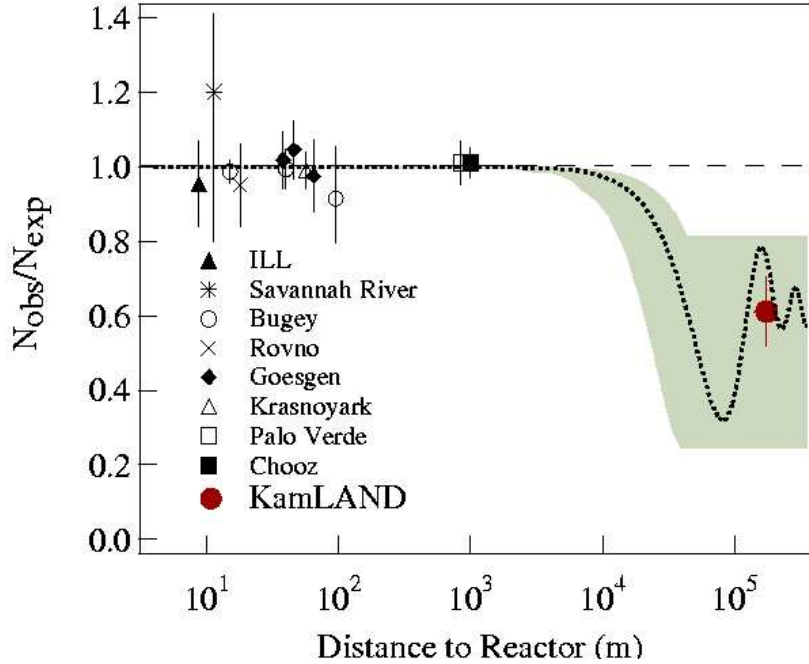


FIG. 1.4.: The ratio of observed to expected number of events for reactor neutrinos. The dotted line indicated the prediction based on the oscillation parameters obtained from an analysis of solar neutrino data.

$$R = \frac{(\bar{\nu}_\mu/\bar{\nu}_e)_{\text{observed}}}{(\bar{\nu}_\mu/\bar{\nu}_e)_{\text{predicted}}}, \quad (1.21)$$

A value of 1 would indicate the expected ratio of ν_μ to ν_e , while a value of .5 is found experimentally. Neutrino oscillations with a mass squared difference of $\Delta m^2 \simeq 10^{-3} \text{ eV}^2$ are consistent with the measured value of the double ratio. The effect can be explained by either a deficit of ν_μ resulting from oscillations of $\nu_\mu \rightarrow \nu_\tau$, or an increase in the ν_e flux and decrease in the ν_μ flux resulting from $\nu_\mu \rightarrow \nu_e$ oscillations. The latter possibility is highly disfavored by the results of the Palo Verde [16] and Chooz [17] reactor neutrino experiments; therefore oscillations between ν_μ and ν_τ are expected to be the leading cause of the atmospheric neutrino anomaly.

The existence of neutrino oscillations provides valuable information about the

nature of neutrinos that can be seen in the oscillation probability given in eq. 1.19. Neutrino oscillations require that the neutrino is massive; however only the differences in the squared masses can be probed, so the absolute masses of the neutrino mass eigenstates remain unknown. Neutrino oscillations also require that the flavor eigenstates $(\nu_e, \nu_\mu, \nu_\tau)$ are mixtures of mass eigenstates (labeled above as ν_1, ν_2, ν_3).

Another interesting property of the neutrino is its handedness, or “chirality”. The chirality of a particle is defined as right-handed if the direction of its spin vector is the same as the direction of its momentum vector. A particle with left-handed chirality, therefore, is defined as one in which the spin vector points in the opposite direction of the momentum vector. According to the Standard Model, only left-handed neutrinos can interact with matter, and only right-handed anti-neutrinos can interact with matter.

A closely related issue is whether the anti-neutrino is a distinct anti-particle counterpart to the neutrino. Inverse β -decay reactions:

$$\bar{\nu}_e + p \rightarrow n + e^+ \quad (1.22)$$

$$\nu_e + n \rightarrow p + e^- \quad (1.23)$$

are known to occur in nature, while the reactions:

$$\nu_e + p \rightarrow n + e^+ \quad (1.24)$$

$$\bar{\nu}_e + n \rightarrow p + e^- \quad (1.25)$$

do not occur. Therefore it appears the ν_e and $\bar{\nu}_e$ are distinct particles, which are referred to as Dirac particles; however, the exact handed-ness of neutrinos and anti-neutrinos discussed above can also explain these results if the neutrino

is a Majorana particle, i.e. it is its own anti-particle, and they differ only by handedness as illustrated in eq. 1.26.

$$\nu_e = \nu_e^{LH} \text{ and } \bar{\nu}_e = \nu_e^{RH} \quad (1.26)$$

In this case, eq. 1.24 and 1.25 are not forbidden by any conservation law, but are suppressed by helicity for massive neutrinos.

An interesting consequence of Majorana neutrinos is the phenomenon of neutrinoless double β -decay. Double β -decay is known to occur in nature in nuclei that β -decay through an intermediate virtual nucleus with greater mass than the parent, with emission of an electron and an anti-neutrino. The virtual nucleus immediately β -decays with emission of another electron and anti-neutrino. Equation 1.27 illustrates the 2 neutrino double beta decay ($2\nu\beta\beta$ -decay) of ^{136}Xe .

$$^{136}\text{Xe} \rightarrow ^{136}\text{Ba} + e^- + e^- + \bar{\nu}_e + \bar{\nu}_e. \quad (1.27)$$

If neutrinos are Majorana particles, then neutrinoless double beta-decay ($0\nu\beta\beta$ -decay) is also possible. In $0\nu\beta\beta$ -decay, the intermediate virtual nucleus absorbs the neutrino emitted by the parent nucleus and emits a second electron, as illustrated in eq. 1.28 for ^{136}Xe .

$$^{136}\text{Xe} \rightarrow ^{136}\text{Ba} + e^- + e^-. \quad (1.28)$$

The observation of $0\nu\beta\beta$ -decay would demonstrate that neutrinos are Majorana particles, and the measurement of the rate of this decay can be used to determine the absolute mass of the neutrino. Several experiments are currently underway to examine this subject [18].

The magnetic moment and life time of neutrinos are other properties that have thus far remained unmeasured, though limits have been made. The limit on the magnetic moment of the neutrino is on the order of $10^{-10} \mu_B$ for electron

and muon neutrinos, and of order 10^{-7} for tau neutrinos (where μ_B is the Bohr magneton, which is approximately the magnetic moment of the electron) [19].

In short, the properties of neutrinos have been studied diligently for decades. As a result, it is known that:

1. There appear to be three flavors of neutrino.
2. The three flavor eigenstates interact only through the weak interaction or neutral current, and couple only to their respective lepton partner.
3. The three flavors are mixtures of three mass eigenstates with different masses.

Some of the remaining uncertainties include (but are certainly not limited to):

1. The absolute mass of the neutrino mass eigenstates is unknown.
2. The magnetic moment of the neutrino has not been successfully measured.
3. The life-time of the neutrino is unknown.
4. The Dirac/Majorana nature of the neutrino is unknown.

The multitude of open questions regarding the nature and interactions of neutrinos makes neutrino physics one of the most important and interesting fields of elementary particle physics today.

1.3 Astrophysical Electron Anti-Neutrinos

The study of electron anti-neutrinos ($\bar{\nu}_e$'s) from astrophysical sources can help address some unanswered questions regarding the nature of neutrinos, and the structure and history of the universe. Although there are many possible astrophysical sources of neutrinos, here we will discuss three likely sources:

1. WIMP annihilation

2. Solar neutrino \rightarrow anti-neutrino conversion

3. Supernova neutrinos

1.3.1 WIMP Annihilation Neutrinos

Studies of the Cosmic Microwave Background (CMB) have determined that approximately 23% of the energy density of the universe is comprised of non-baryonic “Dark Matter” [20], which is generally thought to be made up of Weakly Interactive Massive Particles (WIMP’s). A likely candidate for WIMP’s are neutralinos, the lightest supersymmetric particle. If neutralinos (χ , $\bar{\chi}$) exist, they will be gravitationally trapped in the sun and Earth, where they can annihilate, producing particles such as fermion-antifermion pairs, gauge bosons, Higgs bosons and gluons, etc. according to:

$$\chi\bar{\chi} \rightarrow l^+l^-, q\bar{q}, gg, q\bar{q}g, W^+W^-, Z^0Z^0, Z^0H^0, W^\pm H^\mp, H^0H^0. \quad (1.29)$$

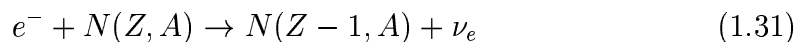
Decay of these annihilation products leads to the production of neutrinos and anti-neutrinos in the sun and Earth. The flux of electron anti-neutrinos from these processes has been calculated in [21] and [22]. The expected event rate for KamLAND from WIMP annihilation $\bar{\nu}_e$ is on the order of 0.01-0.1 events per year. Due to the low event rate, this source of astrophysical neutrinos is not considered in this study.

1.3.2 Relic Supernova Neutrinos

With every gravitational collapse that has occurred since the formation of galaxies in the early universe the flux of all flavors of neutrinos has increased. The flux density and spectral shape of the neutrino spectrum due to these Supernova Relic Neutrinos (SRN) contains information related to the amount of matter contained in neutron stars and black holes, as well as the rate of stellar formation in the universe [23].

Core collapse supernovae is believed to be the final stage in stellar evolution for stars with masses between 8 and 60 solar masses. At the end of the star's evolution, all lighter elements have fused to iron in the core of the sun, where the density has reached $\sim 10^{10} \text{ g cm}^{-3}$, while the lighter elements form onion-like shells of decreasing atomic mass surround the iron core.

The weight of the core is supported by the pressure of degenerate electrons. Photo-dissociation of iron (see eq. 1.30) absorbs $\sim 124 \text{ MeV}$ of energy, decreasing the kinetic energy and pressure of the electrons, while electron capture on nuclei and free protons (see eq. 1.31, 1.32) reduces the number of electrons, and thus the electron pressure.



The ν_e 's produced during this phase (the “capture phase”) escape the core with energies averaging from 12 to 16 MeV, and carry $\sim 10^{53}$ ergs of energy out of the core for a star of 25 solar masses.

As energy is carried out of the core and the electron density is reduced, the density of the core increases. When the density exceeds $\sim 3 \times 10^{11} \text{ g cm}^{-3}$, neutrinos cannot escape from the collapsing core. When the density reaches $10^{14} \text{ g cm}^{-3}$, the pressure of degenerate nucleons stops the collapse. and produces a shock wave that travels outward through the outer core, which is still collapsing. As the shock wave meets the infalling material, its energy is dissipated by photo-dissociation of nuclei into neutrons and protons. The protons left behind the shock wave are converted to neutrons by electron capture, producing electron neutrinos.

As material (in the form of protons, neutrons and electrons) falls into the the core through the shock wave, the density and energy of the core increases.

Neutrinos of all flavors are produced through the following processes:

$$e^+ + e^- \rightarrow \nu + \bar{\nu}, \quad (1.33)$$

$$e^\pm + N \rightarrow e^\pm + N + \nu + \bar{\nu}, \quad (1.34)$$

$$N + N \rightarrow N + N + \nu + \bar{\nu}, \quad (1.35)$$

$$\gamma \rightarrow \nu + \bar{\nu}, \quad (1.36)$$

$$\gamma + e^\pm \rightarrow e^\pm + \nu + \bar{\nu}. \quad (1.37)$$

The majority of the binding energy of the star ($\sim 3 \times 10^{53}$ ergs) is released in the form of all neutrino flavors, with average energies of $\langle E_{\nu_e} \rangle \simeq 10$ MeV, $\langle E_{\bar{\nu}_e} \rangle \simeq 15$ MeV, and $\langle E_{\nu_x} \rangle \simeq 20$ MeV, where ν_x indicates all muon and tau neutrino flavors; however, the average energies of neutrinos in the SRN flux will be redshifted depending upon the distance between the source and the earth. A more complete explanation of supernova physics can be found in Ref. [24].

An attempt to measure the flux of supernova relic neutrinos has been reported in Ref. [25] for neutrino energies above 19.3 MeV. No events were found in excess of the expected background in a ~ 1500 day measurement. For various theoretical models of cosmic evolution, upper limits were placed on the flux of SRN's between 20 and $130 \bar{\nu}_e \text{ cm}^{-2} \text{ s}^{-1}$. In all cases, the obtained upper limit was much larger than the theoretical prediction; therefore, no models of cosmic evolution could be excluded by the measurement. In addition, a model independent upper limit on the SRN flux with energy $E_\nu > 19.3$ MeV of $1.2 \bar{\nu}_e \text{ cm}^{-2} \text{ s}^{-1}$ was obtained.

In the presence of a SRN flux equal to the upper limit quoted above of $1.2 \bar{\nu}_e \text{ cm}^{-2} \text{ s}^{-1}$, the expected rate event rate in KamLAND will be $\sim 0.1 \text{ yr}^{-1}$ assuming 100% detection efficiency.

1.3.3 Electron Anti-Neutrinos from the Sun

Although neutrino flavor oscillations are strongly favored as the dominant mechanism responsible for the solar neutrino problem (see section 1.2), the

limited precision of current measurements does not exclude the possibility that other processes occur at a subdominant level. Understanding these processes is important to an understanding of the nature of neutrinos and solar physics.

1.3.3.1 Spin Flavor Precession

One possible sub-dominant process is spin-flavor precession (SFP). In SFP, the neutrino transition (flavor off-diagonal) moments interaction with the magnetic field of the sun converts left handed ν_e into right-handed $\bar{\nu}_\mu$ or $\bar{\nu}_\tau$. The $\bar{\nu}_\mu$'s produced in the sun by SFP will then undergo ordinary flavor oscillations between the sun and Earth, resulting in a flux of $\bar{\nu}_e$'s on Earth from the sun. Only Majorana neutrinos can have transition magnetic moments; therefore the detection of a $\bar{\nu}_e$ flux from the sun would demonstrate the Majorana nature of the neutrino, as well as its non-zero magnetic moment.

The solar $\bar{\nu}_e$ production probability is calculated in detail in Ref. [26]. For the combined effects of SFP and neutrino flavor oscillations, there are two possible scenarios. In one case, ν_{eL} produced in the sun undergo flavor oscillations into $\nu_{\mu L}$ followed by SFP into $\bar{\nu}_{eR}$ (eq. 1.38). In the second case, SFP transforms ν_{eL} into $\bar{\nu}_{\mu R}$, which then oscillate into $\bar{\nu}_{eR}$ (eq. 1.39).

$$\nu_{eL} \rightarrow \nu_{\mu L} \rightarrow \bar{\nu}_{eR} \quad (1.38)$$

$$\nu_{eL} \rightarrow \bar{\nu}_{\mu R} \rightarrow \bar{\nu}_{eR} \quad (1.39)$$

The magnetic fields between the sun and the earth are negligibly small so the process represented by eq. 1.38 is unlikely and will be neglected here. Hereafter we will assume the transition is of the form of eq. 1.39, where SFP transforms ν_{eL} to $\bar{\nu}_{\mu R}$ at the point of ν_e production ($0.05 \times R_s$, where R_s is the radius of the sun), and vacuum oscillations transform $\bar{\nu}_{\mu R}$ to $\bar{\nu}_{eR}$ between the sun and earth. In the following discussion, “natural units” are used, i.e. $\hbar = c = 1$, and the neutrino

velocity is assumed to approximately equal to the speed of light, c , so $dx = cdt \simeq dt$.

Combining the effects of SFP with neutrino flavor oscillations, the probability that solar ν_e will transform into $\bar{\nu}_e$ between the sun and earth is given by:

$$P(\nu_{eL} \rightarrow \bar{\nu}_{eR}) = P(\nu_{eL} \rightarrow \bar{\nu}_{\mu R}; R_s) P(\bar{\nu}_{\mu R} \rightarrow \bar{\nu}_{eR}; R_{es}). \quad (1.40)$$

Substituting the neutrino flavor oscillation probability, this becomes:

$$P(\nu_{eL} \rightarrow \bar{\nu}_{eR}) = P(\nu_{eL} \rightarrow \bar{\nu}_{\mu R}; R_s) \sin^2 2\theta \sin^2 \left(\frac{\Delta m^2}{4E} R_{es} \right), \quad (1.41)$$

where R_s is the solar radius, R_{es} is the distance between the sun and the earth, and Δm^2 is the neutrino mass squared difference and $\sin^2 2\theta$ is the neutrino mixing parameter. The calculation of the SFP probability, $P(\nu_{eL} \rightarrow \bar{\nu}_{\mu R}; R_s)$, remains to be calculated.

The evolution of the neutrino system under the effects of SFP can be described by the following expression [26, 27]:

$$\begin{pmatrix} i\nu'_{eL} \\ i\bar{\nu}'_{eR} \\ i\nu'_{\mu L} \\ i\bar{\nu}'_{\mu R} \end{pmatrix} = \begin{pmatrix} (V_e - c_2\delta) & 0 & s_2\delta & \mu B_\perp \\ 0 & -(V_e + c_2\delta) & \mu B_\perp & s_2\delta \\ s_2\delta & -\mu B_\perp & (V_\mu + c_2\delta) & 0 \\ \mu B_\perp & s_2\delta & 0 & -(V_\mu - c_2\delta) \end{pmatrix} \begin{pmatrix} \nu_{eL} \\ \bar{\nu}_{eR} \\ \nu_{\mu L} \\ \bar{\nu}_{\mu R} \end{pmatrix} \quad (1.42)$$

where $V_e = \sqrt{2}G_F[N_e(r) - N_n(r)/2]$ and $V_\mu = \sqrt{2}G_F[-N_n(r)/r]$ are the matter induced potentials for electron and muon neutrinos, respectively, N_e and N_n are the number densities of electrons and neutrons, $s_2 = \sin 2\theta$, $c_2 = \cos 2\theta$, and $\delta = \Delta m^2/4E$. B_\perp and μ are the value of the solar magnetic field and the magnetic moment of the neutrino, respectively. The term relevant to the transition probability of $\nu_{eL} \rightarrow \bar{\nu}_{\mu R}$ is:

$$i\bar{\nu}_{\mu R} = \mu B_\perp \nu_{eL} + s_2\delta \bar{\nu}_{eR} - (V_\mu - c_2\delta)\bar{\nu}_{\mu R}, \quad (1.43)$$

however, the $\bar{\nu}_{eR}$ can be neglected due to cancellations between the amplitudes of the processes in eq. 1.38 and 1.39. The amplitude for $\nu_{eL} \rightarrow \bar{\nu}_{\mu R}$ transitions is then:

$$A(\nu_{eL} \rightarrow \bar{\nu}_{\mu R}; R_s) = \int_{r_i}^{R_s} \mu B_{\perp}(r) \nu_{eL}(r) e^{-i \int_{r_i}^r (V_{\mu} - c_2 \delta) dr'} dr, \quad (1.44)$$

where r_i is the radius at which the ν_{eL} is produced and $\nu_{eL}(r)$ is determined by neutrino flavor oscillations. In the adiabatic approximation,

$$\nu_{eL}(r) = \cos\theta(r_i) \cos\theta(r) e^{-i \int_{r_i}^r E_1 dr'} + \sin\theta(r_i) \sin\theta(r) e^{-i \int_{r_i}^r E_2 dr'}, \quad (1.45)$$

where

$$E_{1,2} = \frac{V_e + V_{\mu}}{2} \mp \omega \quad (1.46)$$

$$\omega = \sqrt{\left(\frac{V_e - V_{\mu}}{2} - c_2 \delta\right)^2 + (s_2 \delta^2)}, \quad (1.47)$$

and $\theta(r)$ is the mixing angle in matter at the point r , defined as:

$$\cos 2\theta(r) = \frac{c_2 \delta - \frac{V_e - V_{\mu}}{2}}{\omega}. \quad (1.48)$$

Substituting 1.45 into 1.44, the transition amplitude becomes:

$$A(\nu_{eL} \rightarrow \bar{\nu}_{\mu R}; R_s) = \int_{r_i}^{R_s} \mu B_{\perp} [\cos\theta(r_i) \cos\theta(r) e^{-ig_1(r)} + \sin\theta(r_i) \sin\theta(r) e^{-ig_2(r)}] dr, \quad (1.49)$$

where

$$g_{1,2}(r) = \int_{r_i}^r \left(\frac{V_e + 3V_{\mu}}{2} - c_2 \delta \mp \omega \right) dr'. \quad (1.50)$$

For energies in the range of solar ^8B neutrinos, the solution of the integral in eq. 1.49 can be evaluated to yield:

$$A(\nu_{eL} \rightarrow \bar{\nu}_{\mu R}; R_s) \simeq \left[\frac{\sin^2 \theta(r_i) \mu B_{\perp}(r_i)}{g_2'(r_i)} \right] \Big|_{r_i=0.05 R_s} \quad (1.51)$$

To first approximation, the amplitude may be replaced with its average value and substituted into eq. 1.41 to find the transition probability:

$$P(\nu_{eL} \rightarrow \bar{\nu}_{eR}) \simeq 1.8 \times 10^{-10} \sin^2 2\theta \left[\frac{\mu}{10^{-12} \mu_B} \frac{B_{\perp}(0.05 R_s)}{10 kG} \right]^2, \quad (1.52)$$

which describes the transition probability for solar $\nu_{eL} \rightarrow \bar{\nu}_{eR}$ in the presence of SFP occurring at the point of ν_{eL} production at 0.05 solar radii followed by LMA vacuum oscillations between the sun and the earth.

Measurements of the solar $\bar{\nu}_e$ flux have been reported in Ref. [28, 29], with the current best limit on the transition $\nu_{eL} \rightarrow \bar{\nu}_{eR}$ set by [28] at 0.8% at the 90% confidence level. This corresponds to a total ${}^8\text{B}$ solar $\bar{\nu}_e$ flux on earth of $4.4 \times 10^4 \text{ cm}^{-2} \text{ s}^{-1}$. Such a flux would produce in KamLAND a signal rate of $\sim 500 \text{ yr}^{-1}$ over the entire ${}^8\text{B}$ energy range; a signal which is far above the expected backgrounds. The sensitivity of KamLAND to $\bar{\nu}_e$ in this energy range should allow for a more sensitive search for the solar $\bar{\nu}_e$ flux.

1.3.3.2 Neutrino Decay

A flux of $\bar{\nu}_e$'s from the sun could also be related to the life time of the neutrino if neutrinos decay between the sun and the earth [30].

According to the LMA solution to the solar neutrino problem, the ${}^8\text{B}$ solar neutrinos in the energy range of $\sim 8 - 15 \text{ MeV}$ are created as nearly pure ν_2 eigenstates. Since m_{ν_2} is greater than m_{ν_1} , ν_2 may decay via a reaction:

$$\nu_{2L} \rightarrow \bar{\nu}_{1R} + X, \quad (1.53)$$

where X is some light or massless particle such as a Majoron. This type of decay is referred to as non-radiative, since no photons are produced. If the neutrino masses are quasi-degenerate and the mass of the Majoron is negligible compared with the mass of the neutrinos, the daughter neutrino carries almost the full energy of the parent, and the energy spectrum of the decay neutrinos will be nearly identical to that of the parent neutrinos.

In this case, the transition probability for $\nu_e \rightarrow \bar{\nu}_e$ can be written as:

$$P(\nu_e \rightarrow \bar{\nu}_e) = BU_{e1}^2 P_2 (1 - e^{-T/\tau}), \quad (1.54)$$

where B is the branching ratio for ν_2 to decay to ν_1 , U_{e1} is the matrix element for LMA mixing and has a value between 0.6 and 0.8, P_2 is the probability of finding ν_2 in the solar neutrino flux after LMA-MSW oscillations, T is the time of flight from the sun to the earth (~ 500 s), and τ is the lab life time of ν_2 . The branching ratio, B, has been calculated in Ref. [31], and has a value of 2/3 in the limit of quasi-degenerate neutrino masses ($m_1 \approx m_2 \approx m_3$) in the hierarchical mass case ($m_1 < m_2 < m_3$). For the MSW-LMA oscillations, $P_2 = \sin^2 \theta_m > 0.82$, where θ_m is the MSW matter mixing angle.

Equation 1.54 can thus be rewritten in a limiting case:

$$P(\nu_e \rightarrow \bar{\nu}_e) \geq 0.328(1 - e^{-T/\tau}), \quad (1.55)$$

and the laboratory lifetime, τ , is related to the rest frame lifetime, τ_0 by the simple relationship:

$$\tau = \frac{E_2}{m_2} \tau_2. \quad (1.56)$$

Since the mass of the neutrino mass eigenstates is unknown, the relevant quantity here is the ratio of τ_2/m_2 . The current limit on this quantity for the type of decay mentioned here is 10^{-4} s/eV [30].

CHAPTER 2

DETECTOR

2.1 Detector Description

The Kamioka Liquid Anti-Neutrino Detector (KamLAND) (Fig. 2.1) is a 1 kiloton liquid scintillator detector located in the site that once housed the original Kamiokande detector deep within Mt. Ikenoyama, about 50 km east of Toyama, Japan. The detector is surrounded on all sides by > 1000 m of rock (2700 meters-water-equivalent), which reduces the cosmic muon flux by a factor of 10^5 relative to the flux at the surface.

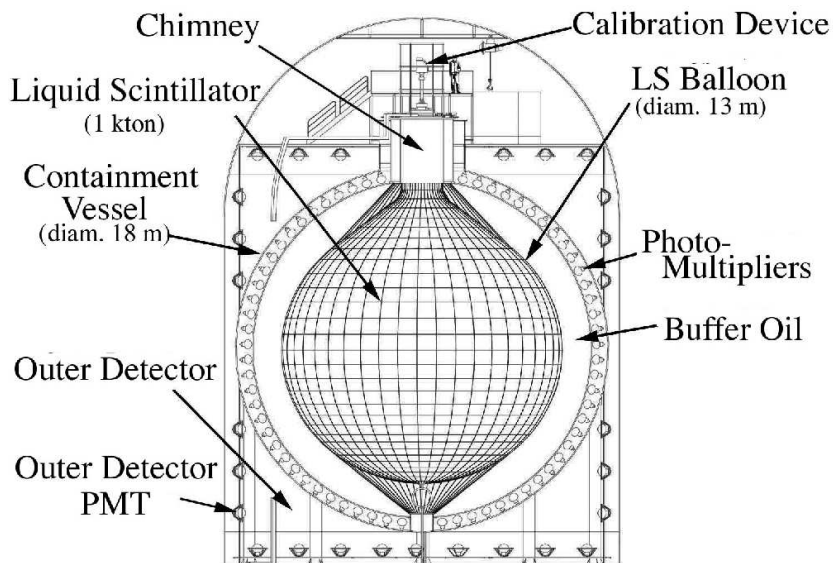


FIG. 2.1.: Schematic of the KamLAND Detector

The active volume of KamLAND consists of a 135 μm -thick Nylon/EVOH balloon, 13 meters in diameter, filled with 1 kton of liquid scintillator composed of 80% dodecane, 20% pseudocumene, and 1.5 g/liter PPO. The balloon is surrounded by a 2.5 meter thick spherical shell of paraffin oil, contained within an 18-m diameter stainless steel sphere that is equipped with 1,879 inward facing photomultiplier tubes (PMT) providing 30% coverage of the fiducial volume. Interactions of charged particles in the scintillator produce flashes of light that are collected and amplified by the PMT's. Of the 1,879 PMT's, 1,325 are fast 17" PMT's, while the remainder are 20" PMT's salvaged from the original Kamiokande detector. Acrylic sheets located in the paraffin oil shell separate the PMT's from the scintillator, providing a barrier against radon emission from the PMT glass.

The stainless steel sphere is contained within a cylindrical cavity carved in the rock of the mine. The cavity, referred to as the outer detector (OD), is filled with purified water and equipped with 225 20" PMT's. The OD is physically divided into 4 regions— the top, upper, lower, and middle. The outer detector tags cosmic muons that pass through or near to the inner detector.

A chimney provides access into the inner detector from a deck located above the detector. The scintillator balloon opens through a tube shaped neck into the area above the deck. This opening is sealed, and accessible only by means of a glove box and several gate valves. Calibration sources are exposed to the inner detector by lowering them through the neck of the balloon into the inner detector.

2.2 Trigger and Data Acquisition

When charged particles interact with the KamLAND scintillator, photons are produced. When the photons hit the surface of a PMT, they are absorbed, and photo-electrons (PE's) are produced inside the PMT by the photo-electric effect. The photo-electron signal is then amplified by the PMT. The smallest signal that a

PMT can produce corresponds to the production of a single photo-electron (SPE) by a photon incident on the PMT's surface. The KamLAND electronics include internal discriminators for each PMT that signal when a photoelectron pulse has been generated by the PMT.

Each PMT is connected to an analog-transient-waveform-digitizer (ATWD). When a PMT produces a signal with an amplitude greater than $\sim 1/3$ the amplitude of a SPE pulse, the ATWD digitizes the waveform by taking 128 samples of the waveform over an interval of 200 ns. The digitized waveform is stored in a data buffer, and a signal is sent to the trigger system to indicate that a waveform has been recorded for that PMT. The ATWD stores the waveform for up to 175 ns, after which the waveform is overwritten.

The KamLAND trigger is based on a simple “nsum” routine. If the trigger receives signals from 200 ATWD's ($\text{nsum} \geq 200$) within a 175 ns time window, it issues a command to the data acquisition system to acquire the event. Since the PE yield for KamLAND is ~ 300 PE/MeV, the KamLAND trigger threshold of $\text{nsum} = 200$ PMT's corresponds to ~ 0.7 MeV. Immediately after digitization, the trigger threshold is lowered to 120 PMT's to look for delayed coincidence events and low energy decays.

In addition to issuing the command to acquire data, the trigger supplies the DAQ system with the following data:

1. A 48-bit timestamp which indicates the number of ticks of a 40 MHz clock that have elapsed between the beginning of a run and the acquisition of the event
2. A 36-bit trigger-type that indicates the trigger conditions
3. The 12-bit ID nsum, or the total number of PMT's that have produced a signal during the event

4. A 6-bit OD nsum for each of the 4 outer detector segments

This data is combined with the PMT waveforms, and the “launch-offset” for each PMT, which is the time difference between the ATWD notifying the trigger that it has recorded a waveform and the time that the trigger issues the command to acquire an event. Since the trigger waits until at least 200 PMT’s have registered waveforms before issuing the command to acquire an event, the launch offset is important to determining the arrival time of photons at each PMT relative to the trigger time. The relative arrival time of photons at the PMT’s is used in determining the position of events inside the detector.

2.3 Calibration

The KamLAND data acquisition system records, among other things, the arrival times of photons and the waveforms produced by PMTs; however, Physics analyses rely on the knowledge of event energy and time. In order to convert the raw data into energies and times, calibrations are carried out to measure the response of the KamLAND detector to events of known energy, position, and time structure.

2.3.1 Source Deployment System

Access to the KamLAND inner detector is possible through a glove box mounted on the top of the chimney (see Fig. 2.1). Calibration sources are attached to the end of a stainless steel cable that is lowered by an electric motor to points along the central axis of the detector. The raising and lowering of the sources are controlled remotely by PC running LabVIEW.

2.3.2 Gamma Sources

The energy scale calibration is based on several γ sources deployed along the z-axis of the detector. The design and testing of the ^{60}Co and ^{65}Zn sources are

described in Appendix B. In addition to these sources, ^{68}Ge and ^{203}Hg sources have been built and deployed in the detector. Table 2.1 lists the total energies of γ -rays produced by the calibration sources.

Source	γ Energy (MEV)
^{203}Hg	.279
^{68}Ge	$.511 \times 2 = 1.022$
^{65}Zn	1.116
^{60}Co	$1.173 + 1.113 = 2.506$

TABLE 2.1.: Summary of source energies used for the calibration of the KamLAND energy scale.

All four sources discussed here are also β emitters; however, the double source encapsulation effectively absorbs all β 's produced. The encapsulation also produces minimal distortion in the γ spectrum which is easily understood by Monte Carlo simulation (see section 2.4).

In addition to finding the detector response to events of known energy, the γ sources have been used to determine the relative timing of the PMT's in the inner detector. Transit times for signals in the detector differ from PMT to PMT because of slightly different cable lengths, high voltage, and minor differences in the electronics. In order to accurately determine the arrival times for photons at PMT's relative to the trigger, the signal transit time must be subtracted for each PMT. By deploying the source at the center of the detector and acquiring on the order of 10,000 events, the signal transit time, referred to as t_0 , is measured. The arrival times of photons are used to reconstruct event positions.

2.3.3 AmBe Source

The Americium-Beryllium source (AmBe) is a compound source that produces neutrons in coincidence with a 4.4 MeV γ . Neutron captures are tagged in the detector by requiring a prompt event of 4.4 MeV, followed by the 2.2 MeV γ produced by neutron capture on hydrogen. Using this data, the neutron detection

efficiency and the spacial/time correlation between the 4.4 MeV prompt γ and the 2.2 MeV delayed capture γ are measured. This source also provides additional data points at 2.2 MeV, 4.4 MeV, and 7.65 MeV (with small branching ratio) for the energy calibration of the detector.

2.3.4 Spallation Neutrons

Neutrons are produced isotropically in the scintillator by muons passing through the detector. These neutrons, called “spallation neutrons”, provide a means of calibrating the energy scale of the detector off of the z-axis to which the other sources are confined. Figure 2.2 shows the reconstructed energy distribution of capture γ ’s from spallation neutrons throughout the KamLAND fiducial volume. The results of the fit give a central value of 2.237 MeV, which agrees at the level of 0.5% with the expected value of 2.223 MeV. The energy resolution found is 5.2% for the entire fiducial volume at 2.223 MeV.

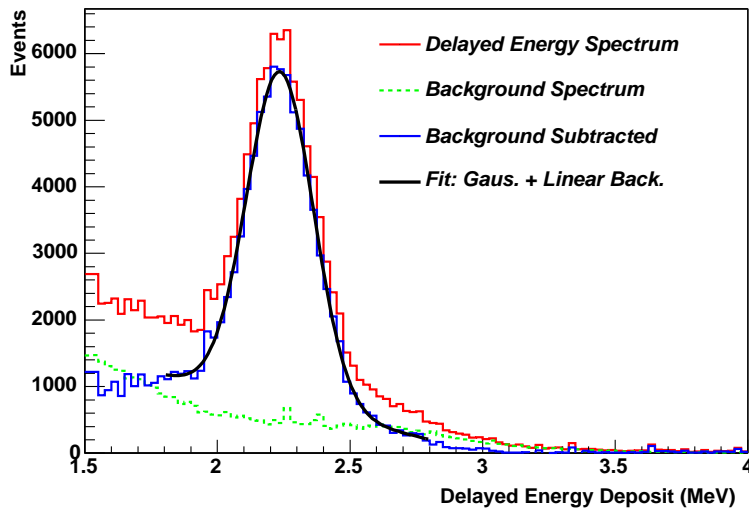


FIG. 2.2.: The reconstructed energy spectrum for spallation neutrons throughout the KamLAND fiducial volume.

2.3.5 Laser System

A laser system produces UV light that is converted within millimeters of its point of production into scintillation light. The laser, therefore, provides a point source of scintillation light. The intensity of the laser is adjustable to allow the measurement of the response of the detector over a range of light levels from the single photo-electron level to millions of photo-electrons (or keV to multi-GeV range). From this data, information about the PMT linearity, PMT gain, and the dependence of PMT timing on light level is found.

2.4 Monte Carlo Simulation

A GEANT3 based monte carlo simulation has been developed in order to estimate detection efficiencies and conduct background studies. The simulation includes the basic geometry of KamLAND (see Fig. 2.1 and Fig. 2.3), including:

- The 6.5 meter scintillator sphere, with the density and chemical composition of the actual KamLAND scintillator
- The balloon
- The 2.5 meter shell of buffer oil between the scintillator and the stainless steel sphere
- The stainless steel sphere
- The cylindrical water veto detector
- An air space above the detector, representing the cavern above the actual detector
- A 1 meter rock shell surrounding the entire detector

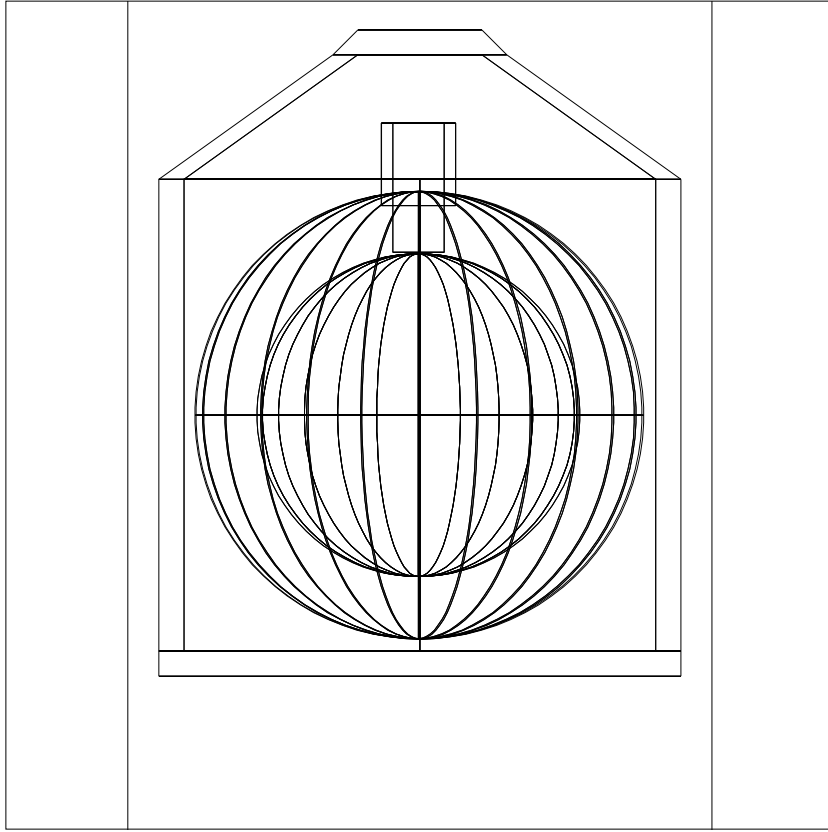


FIG. 2.3.: The simulated KamLAND geometry.

Energy and position resolution are included in the simulation. The simulated and measured spectra for ^{60}Co is shown in Fig. 2.4. The center and width of the distributions agree at the level of 1%, and the simulation correctly reproduces the low energy tail of the distribution that is due to γ -ray attenuation in the source encapsulation.

Figure 2.5 shows the capture time for simulated neutrons in KamLAND. The mean capture time of $200\ \mu\text{s}$ is in good agreement with the measured neutron capture time of $203\ \mu\text{s}$ in KamLAND.

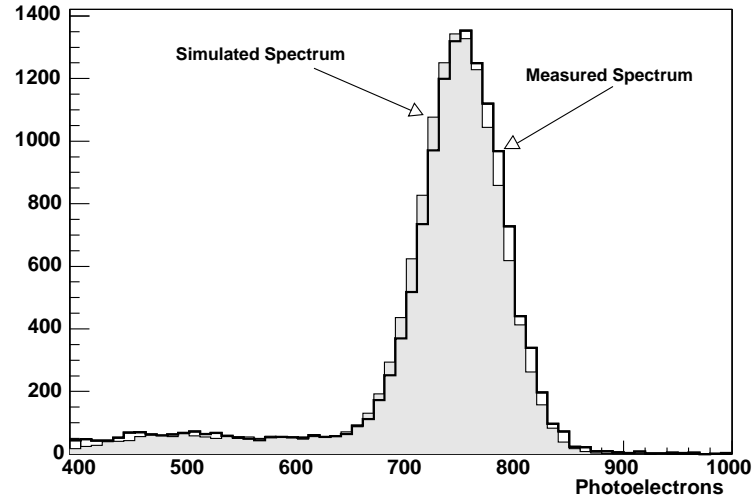


FIG. 2.4.: The simulated and measured ^{60}Co spectrum normalized to the number of events in the full absorption peaks. The heavy solid line is the measured spectrum, and the grey filled area is the simulated spectrum.

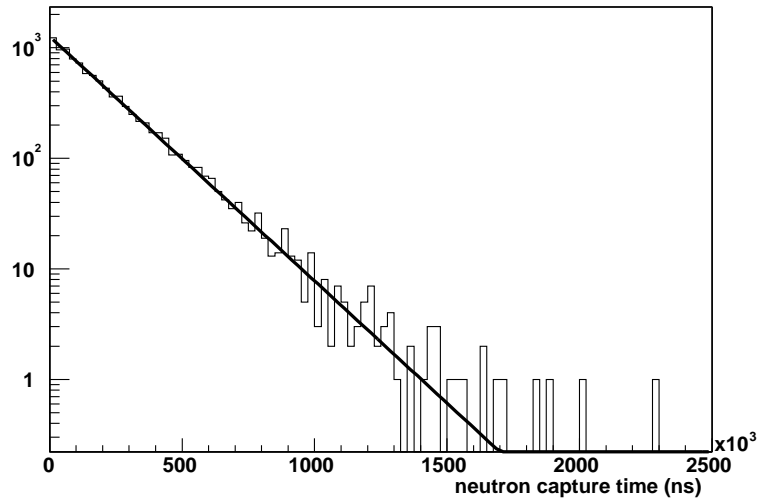


FIG. 2.5.: The neutron capture time for the GEANT3 simulation. The mean capture time is $200 \mu\text{s}$.

CHAPTER 3

EVENT RECONSTRUCTION

For each event acquired by the KamLAND DAQ system, trigger information is recorded along with the signals from each PMT that triggered in the detector (see section 2.2). The PMT signal is a 128 sample waveform whose area represents the total charge produced by the PMT, which is proportional to the light seen by that PMT. The sum of charges produced by all the PMT's during an event can be related to the energy of the event, if the position of the event is known and the particle type is known.

Algorithms have been developed to analyze the PMT waveforms to determine their total charge and arrival times, and then to find the vertex (position) of the event, and finally its energy.

3.1 Waveform Analysis

When PMT's detect light in KamLAND scintillator, they produce a pulse whose arrival time is related to the time of flight of photons from the event vertex to the PMT, and whose area, which represents a measurement of charge produced by the PMT, is related to the amount of light seen by the PMT and thus to the total energy deposited in the detector.

A full description of the KamLAND primary waveform analyzer can be found in Appendix A. Briefly, waveform analysis consists of 4 parts:

1. Pedestal subtraction – Pedestal waveforms (waveforms recorded in the absence of a signal) are acquired at the beginning of each run for each PMT. Before processing a waveform, the pedestal for that PMT is subtracted.
2. Smoothing – The waveform is smoothed using a simple 3-point running average to reduce fluctuations.
3. Pedestal renormalization – After pedestal subtraction and smoothing, there remains an offset between the waveform baseline and the 0 channel line. The pedestal is renormalized to remove this baseline.
4. TQ mapping – The charge and times of pulses in the waveform are mapped using algorithms described in Appendix A.

Figure 3.1 shows the results of the first three steps of waveform analysis. Figure 3.2 shows the results of tq mapping. The arrival time of the pulse is taken as t_{ofq} , while the charge is obtained by integrating from t_1 to t_2 .

3.2 Vertex Reconstruction

The PMT's lining the stainless steel sphere in KamLAND are arranged in diamond shaped groupings of 64 PMT's each. The KamLAND vertex fitter, or “Diamond time Fitter” (DTF) [32], uses the average arrival times of photons at the PMT diamonds to estimate the position of events in KamLAND.

The arrival time of a photon at a the i^{th} PMT relative to the trigger time is given by:

$$t_a^i = t_{trig} - t_{LO}^i + t_0^i, \quad (3.1)$$

where t_{trig} is the trigger time, t_{LO}^i is the launch offset (see section 2.2), and t_0^i is the PMT signal transit time correction (see section 2.3.2).

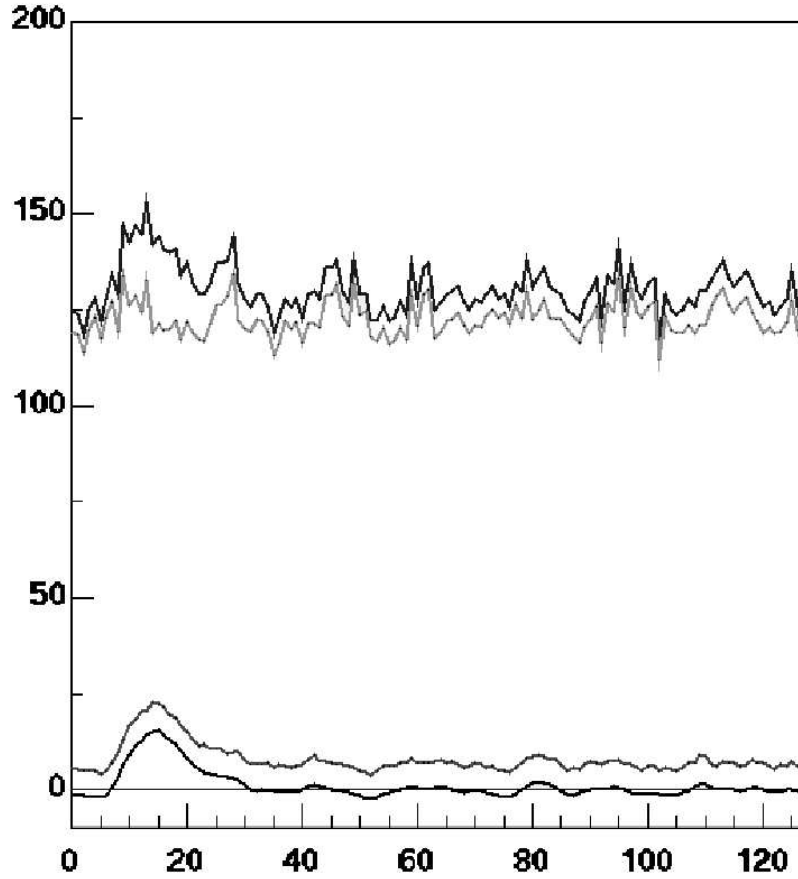


FIG. 3.1.: From top to bottom: Raw waveform, pedestal waveform, pedestal subtracted waveform, pedestal subtracted renormalized and smoothed waveform. The x-axis is time bins (~ 1.5 ns/bin), and the y-axis is ADC counts.

The diamond time fitter assumes a vertex location (at the center of the detector for the first iteration) and calculates the relative distribution of arrival times of photons at each PMT diamond. The calculation assumes that light travels in a straight line from the vertex to the PMT, without scattering. The geometry of the detector is included in the calculation, allowing for an accurate calculation the distance traveled by light in scintillator and the distance traveled by light in buffer oil, and the time of flight is simply the sum of the distance traveled divided by the speed of light in each material. In the actual detector, the speed

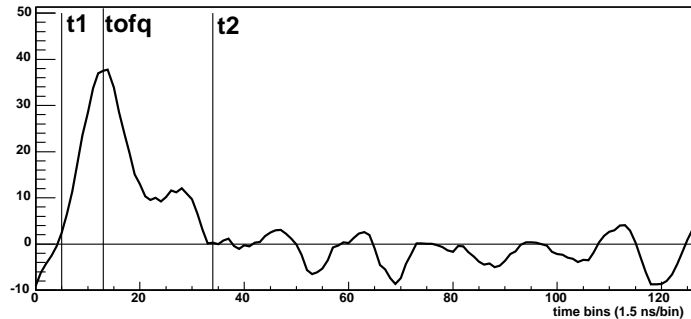


FIG. 3.2.: Vertical lines indicate the t_1 , t_2 , and tofq found for a PMT waveform.

of light is a function of photon wavelength, but here a single average value is used for each medium. The speeds of light in scintillator and buffer oil are the only tunable parameters in the routine. The relative arrival times of the photons at the PMT's are calculated from the time of flight of the photons. For each diamond, a histogram is made of the charge weighted arrival times. Only photons that fall between the 10% and 50% time integrals of the histogram are used in order to reduce the early noise hits and the late hits from scattered or re-emitted light.

The difference in the arrival times of the real data and the arrival times calculated from the vertex guess indicates whether the vertex is closer or farther away from the diamond than the guess. The vertex is shifted until the relative arrival times of photons from the guessed vertex is consistent with those observed in the real event. Once this is successful for the diamonds, the vertex is further refined by repeating the analysis using individual arrival times of photons at individual PMT's.

The accuracy of the vertex fitter has been estimated using calibration sources positioned along the z -axis of the detector. For ^{60}Co , the reconstruction is accurate to within a systematic shift of 2.2 cm (see fig. 3.3). At 7.65 MeV, the systematic uncertainty becomes 15 cm near the top and bottom of the balloon. The position

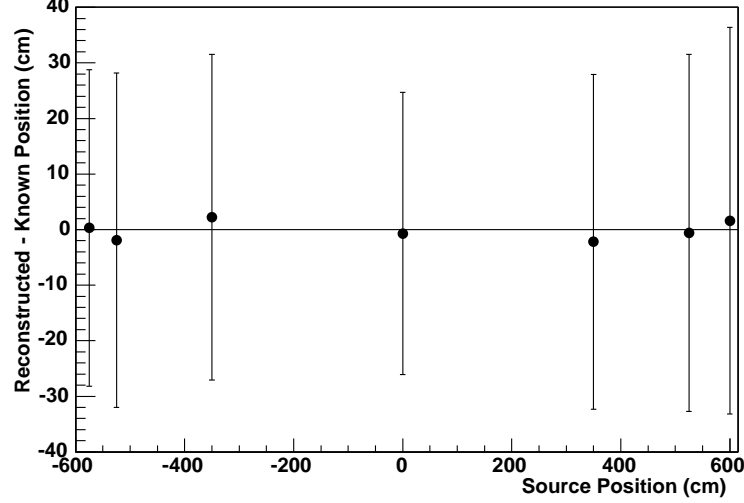


FIG. 3.3.: Performance of the Diamond Time Fitter as a function of z-position for ^{60}Co . Error bars indicate the width of the distributions, which include detector position resolution and the effects of the mean free path of ^{60}Co γ 's in scintillator.

resolution for ^{60}Co , which includes the effects of the mean free path of ^{60}Co γ 's in scintillator is ~ 30 cm.

3.3 Energy Estimation

The KamLAND energy scale is based on calibration data taken with the calibration sources at several positions along the z-axis of the detector, and Monte Carlo simulations aimed at understanding the non-linearity of the energy scale that is the result of quenching and cherenkov light production in the scintillator. A full description of the calculations can be found in the appendices of Ref. [33].

As a reference, the average total charge collected in the detector is calculated for ^{60}Co at the center of the detector. The total charge can be represented as:

$$q_0 = \sum_i^{NPMTs} \alpha \Omega_0^i E_0 T_0^i, \quad (3.2)$$

where NPMTs is the total number of PMT's in the detector, α is a constant that

includes the scintillation efficiency, light yield, PMT quantum efficiency, and gain, Ω_0^i is the solid angle, E_0 is the energy, which is a constant 2.506 MeV, and T_0^i is the light transport function that accounts for attenuation of light in scintillator and in mineral oil and absorption and re-emission of scintillation light. The constants α and E_0 can be removed from the summation.

For an event in KamLAND with a vertex located at x,y,z, the total expected charge collected for a given energy can be found by summing over all the PMT's as above:

$$q_{xyz} = \sum_i^{NHits} \alpha \Omega_{xyz}^i E_{xyz} T_{xyz}^i, \quad (3.3)$$

E_{xyz} in this case is the unknown energy, which can be removed from the summation, α is the same as in eq. 3.2, Ω_{xyz}^i is the PMT's solid angle evaluated at the event vertex, and T_{xyz}^i is the light transport function evaluated at the event vertex. The product inside the summation represents the average charge collected by the i^{th} PMT for an energy deposit, E_{xyz} at the point x,y,z. The expression for the energy of the event can now be found by dividing eq. 3.2 by eq. 3.3 and solving for E_{xyz} .

$$\frac{q_0}{q_{xyz}} = \frac{\alpha E_0 \sum_i^{NPMTs} \Omega_0^i T_0^i}{\alpha E_{xyz} \sum_i^{NPMTs} \Omega_{xyz}^i T_{xyz}^i} \quad (3.4)$$

After some cancellations and rearrangement, the event energy can be expressed as:

$$E_{xyz} = E_0 \frac{q_{xyz}}{q_0} \frac{\sum_i^{NPMTs} \Omega_0^i T_0^i}{\sum_i^{NPMTs} \Omega_{xyz}^i T_{xyz}^i} \quad (3.5)$$

where the ratio of the sum of light transport functions and solid angles is calculated using ^{60}Co data along the z-axis of the detector.

For a given real event at a point x,y,z, the quantity q_{xyz} can be replaced with

the real charge summed over all PMT's viewing light. The expression for the energy becomes:

$$E_{xyz} = E_0 \frac{q_{xyz}^{real}}{q_0} \frac{\sum_i^{NPMTs} \Omega_0^i T_0^i}{\sum_i^{NPMTs} \Omega_{xyz}^i T_{xyz}^i}, \quad (3.6)$$

where:

$$q_{xyz}^{real} = \sum_i^{NHit} q_i \quad (3.7)$$

and NHit is the number of PMT's seeing light and q_i is the charge collected by the i^{th} PMT.

This estimation assumes that the response of the scintillator is linear with respect to the particle type and energy. In truth, the light output of scintillator varies depending on the ionization density, which is a function of particle type and energy. For large ionization densities, the light output of scintillator is less than expected based on smaller ionization densities. For example, a proton depositing 1 MeV in scintillator will produce less light than an electron depositing 1 MeV in scintillator because the ionization density for protons is higher than that of electrons. A common way for modelling this behavior is referred to as Birk's Law. According to Birk's Law, the light output per unit length (dL/dX) can be represented by eq. 3.8:

$$\frac{dL}{dX} = \frac{\frac{dE}{dX}}{1 + kB \frac{dE}{dX}}, \quad (3.8)$$

where kB , called Birk's Constant, relates the density of ionization centers to dE/dX . The constant $kB = 0.012 \text{ g cm}^{-2} \text{ MeV}^{-1}$ has been measured for KamLAND scintillator using α particles.

Cherenkov light production also produces non-linearity in the scintillator light output. When particles travel faster than the speed of light in a medium, they emit Cherenkov radiation. The PMT glass is transparent to wavelengths between

350 nm and 650 nm, therefore Cerenkov photons with wavelengths below 350 nm would ordinarily be absorbed by the PMT glass, however the pseudocumene and PPO in scintillator absorb the wavelengths below 350 nm and re-emit longer wavelength photons that are visible to the PMT's. The contribution of light from Cerenkov radiation below 350 nm must, therefore, be calculated.

The formula for calculating Cerenkov light production is:

$$\frac{dN^c}{dx} = 2\pi z^2 \alpha \sin^2 \theta_c \int_{\lambda_1}^{\lambda_2} \frac{d\lambda}{\lambda^2}. \quad (3.9)$$

Taking into account the absorption and re-emission probability for PC and PPO, the Cerenkov light yield in KamLAND is given by:

$$\frac{dN^c}{dx} = 2\pi z^2 \sin^2 \theta_c (\alpha(\lambda) \int_{\lambda_1}^{\lambda_2} \frac{d\lambda}{\lambda^2} + \beta(\lambda) \int_{\lambda_3}^{\lambda_4} \frac{d\lambda}{\lambda^2}), \quad (3.10)$$

where $\alpha(\lambda)$ is the survival probability for wavelengths below λ_2 interacting with PC and PPO, and $\beta(\lambda)$ is the survival probability for photons with wavelengths between λ_3 and λ_4 .

Once the effects of quenching and Cerenkov light production are understood, they are included in the KamLAND Monte Carlo simulation and the simulation is used to determine the particle dependent energy scale. Monoenergetic positrons, electrons, and gammas with energies of 1 MeV, 3 MeV, 5 MeV, and 7 MeV have been generated at the center of the detector to obtain the particle dependent energy scale functions. For each particle type, a fit of the form:

$$E_{real} = \frac{p_0 \times Q_0}{1 + \frac{p_1}{\sqrt{Q_0}} + p_2 \times Q_0} \quad (3.11)$$

is made to the plot of energy as a function of normalized charge, where Q_0 is the event charge normalized to the total charge of ^{60}Co at the center of the detector and is given by:

$$Q_0 = \frac{Q}{Q_0^{60Co}}. \quad (3.12)$$

The plots of energy vs. charge are shown for positrons and gammas in fig. 3.4 and 3.5, respectively. The fit parameters returned for the positron energy scale are $p_0 = 2.127$, $p_1 = -0.12072$, and $p_2 = -0.00153837$. For the gamma energy scale, the constants returned are $p_0 = 2.108$, $p_1 = -0.095769$, and $p_2 = -0.0012051$.

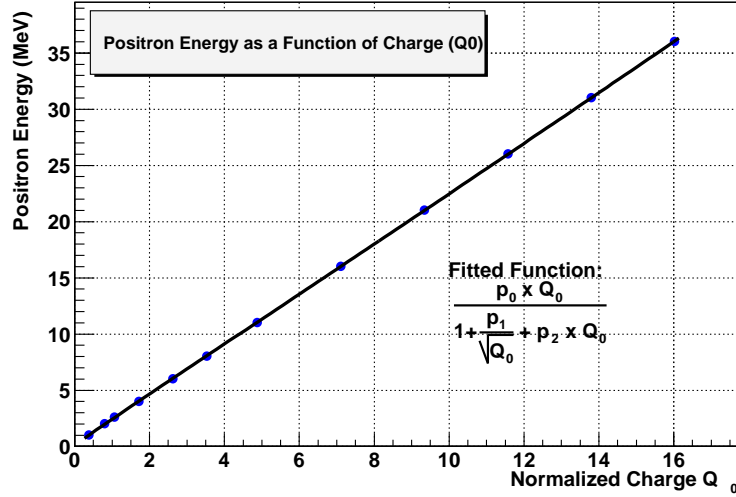


FIG. 3.4.: The positron energy scale function obtained from Monte Carlo simulation.

The accuracy of the energy estimation away from the center is shown in fig. 3.6 for ^{60}Co source reconstructed energies along the z-axis of the detector.

To apply this correction to the results of the simple energy conversion performed in eq. 3.6, we must first convert E_{xyz} back into the charge normalized to the ^{60}Co charge at the center of the detector. This is simply done by division by 2.506 MeV:

$$Q_0 = \frac{E_{xyz}}{2.506 \text{ MeV}}. \quad (3.13)$$

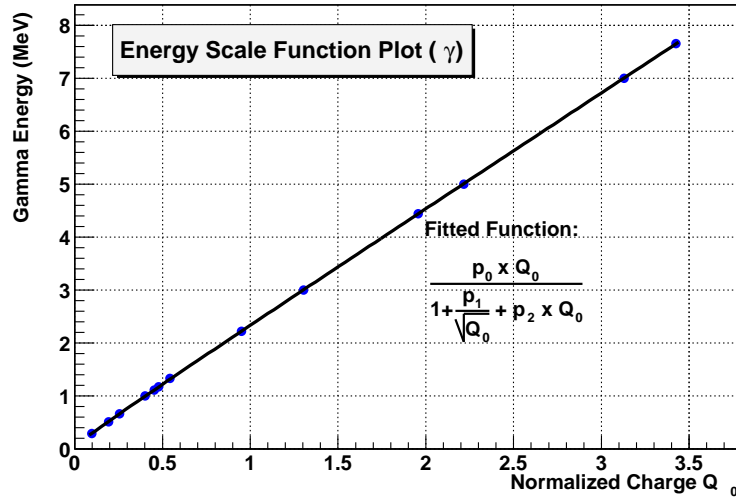


FIG. 3.5.: The gamma ray energy scale function obtained from Monte Carlo simulation.

An inverse β -decay consists of a prompt part due to a positron, and a delayed part due to a γ -ray; therefore, the energy of the prompt part of an inverse β -decay event is calculated using the fit function for positrons while the energy of the delayed part of the event is calculated using the function for γ -rays.

For calibration sources, the energy reconstruction is accurate to 1% uncertainty, with an overall systematic uncertainty of 2.07% [33]. The accuracy has been verified for high energy β 's using ^{12}B decays in the scintillator. Figure 3.7 shows the reconstructed spectrum for ^{12}B in scintillator. The reconstructed end-point energy of 13.42 ± 0.10 MeV agrees with the known value of 13.4 MeV perfectly.

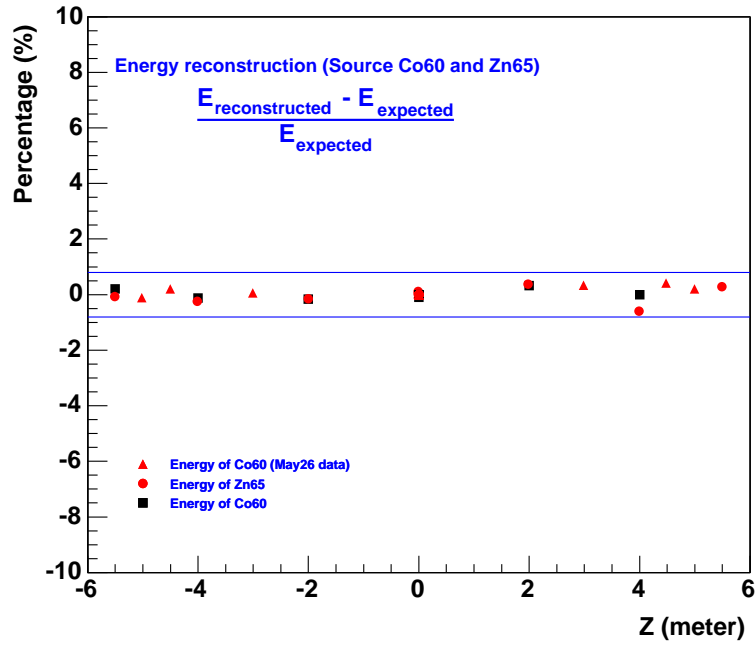


FIG. 3.6.: ^{60}Co source energy reconstruction for positions along the z-axis of the detector.

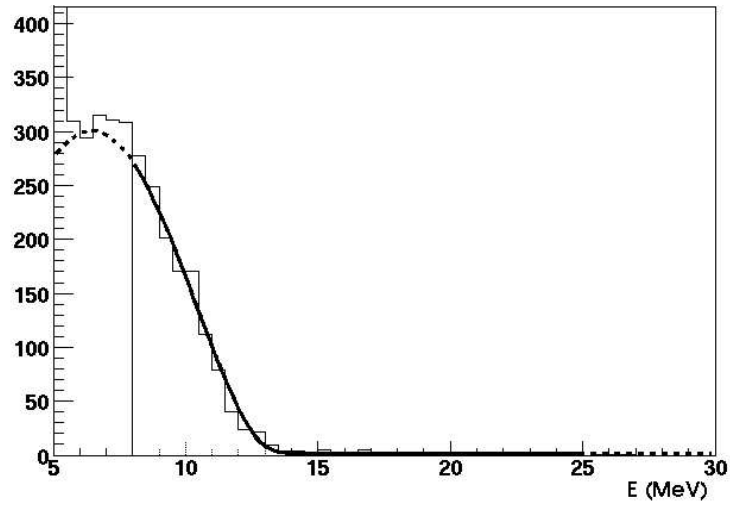


FIG. 3.7.: The energy reconstruction for ^{12}B decays in the KamLAND scintillator [34]. The solid line represents the results over the region included in the fit, while the dotted line represents an extrapolation of the fit function.

CHAPTER 4

ELECTRON ANTI-NEUTRINO DETECTION

4.1 Inverse Beta-Decay

The primary detection mechanism for $\bar{\nu}_e$'s in the KamLAND detector is the inverse β - decay (I β D) reaction shown in Eq. (4.1). The I β D signal consists of a prompt and delayed event. The prompt part includes the ionization energy of the positron combined with the energy released by the annihilation of the positron on an electron ($e^+ + e^- \rightarrow 2\gamma$ ($2 \times .511$ MeV)). This is followed by the capture of the neutron on Hydrogen with the mean capture life time of ~ 200 μ s and emission of a 2.22 MeV γ . The double coincidence structure of the I β D signal provides a powerful means of background reduction.

$$\begin{aligned}\bar{\nu}_e + p &\rightarrow e^+ + n, \\ e^+ + e^- &\rightarrow 2\gamma(2 \times .511MeV) \\ n + p &\rightarrow D + \gamma(2.2MeV)\end{aligned}\tag{4.1}$$

The threshold for I β D is determined by the relationship

$$E_{thresh} = \frac{(m_e + m_n)^2 - m_p^2}{2m_p} = 1.80MeV,\tag{4.2}$$

where m_e , m_n , and m_p are the masses of the electron, neutron, and positron, respectively. The prompt energy in the KamLAND detector is the sum of the

positron kinetic energy, two annihilation γ 's, and the kinetic energy of the neutron; however, since the neutron is almost 2000 times heavier than the electron, it is produced essentially at rest and its kinetic energy is neglected. The $\bar{\nu}_e$ energy can thus be recovered from the prompt energy deposit (assuming an infinitely massive neutron) using the relationships:

$$\begin{aligned} E_{prompt} &= T_{e^+} + 2 \times .511 MeV \\ E_{\bar{\nu}_e} &= T_{e^+} + \Delta + .511 MeV \\ E_{\bar{\nu}_e} &= E_{prompt} + \Delta - .511 MeV = E_{prompt} + .8 MeV, \end{aligned} \quad (4.3)$$

where T_{e^+} is the kinetic energy of the positron and $\Delta = m_n - m_p$ is the difference in the mass of the proton and neutron.

4.1.1 Cross Section

The first order total cross section for $I\beta D$ has the form [35, 36]:

$$\sigma_{tot} = \frac{2\pi^2 \hbar^3 c^2}{(m_e c^2)^5 f^R \tau_n} E_e p_e = (9.52 \times 10^{-44} cm^2 MeV^{-2}) E_e p_e, \quad (4.4)$$

where m_e is the electron mass in MeV/c^2 , f^R is the phase space factor, including Coulomb, weak magnetism, recoil, and outer radiative corrections, and τ_n is the lifetime of the neutron, and the positron energy and momentum are given in MeV .

Figure 4.1 shows the cross section as a function of $\bar{\nu}_e$ energy.

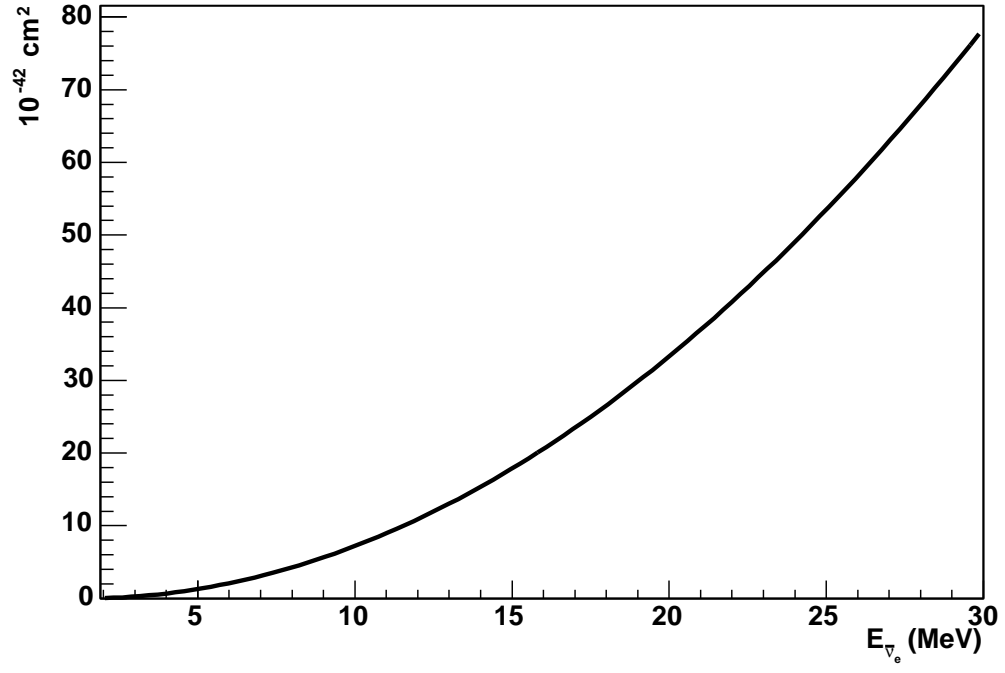


FIG. 4.1.: The cross section for inverse beta decay.

CHAPTER 5

HIGH ENERGY ELECTRON ANTI-NEUTRINO ANALYSIS

5.1 Events Selection

Data acquired during 147 livedays between March and December, 2003, were analyzed to search for Inverse β -decay events in KamLAND. Inverse β -decay events due to the interactions of high energy $\bar{\nu}_e$'s in the KamLAND scintillator are selected according to the following criteria, or “cuts”:

1. Prompt energy deposit - The search for $\bar{\nu}_e$'s from the transformation of ^8B solar ν_e 's through SFP or neutrino decay is carried out for prompt energies between 8.0 MeV and 16.2 MeV, which corresponds to neutrino energies of 8.8 MeV to 17.0 MeV. For relic supernova $\bar{\nu}_e$'s the prompt energy range of 16.2 MeV to 30 MeV ($17.0 \text{ MeV} < E_{\bar{\nu}_e} < 30.8 \text{ MeV}$) is considered.
2. Delayed energy deposit - The delayed energy deposit is required to be between 1.8 and 2.6 MeV. This corresponds to a 3.6σ cut around the 2.2 MeV neutron capture γ energy, which gives an efficiency better than 99.9% for accepting neutron capture γ s.
3. Neutron capture time - The time difference between the prompt and delayed events, which corresponds to the neutron capture time, is required to be in the range of 500 ns - 1000 μs , which is $\sim 99\%$ effective at accepting neutron captures for the estimated 200 μs capture time.

4. Prompt and delayed vertex separation - The prompt and delayed vertices are required to lie within 160 cm of each other. This requirement is designed to reduce the backgrounds due to accidental coincidences in the detector.
5. Muon Veto - Events are rejected if they occur within 4 ms of a muon passing through the inner or outer detector. This reduces the background due to spallation neutrons in the detector.
6. Muon Shower Veto - Events are rejected if they occur within 2 s of a muon shower, defined as a muon depositing at least 3 GeV in the inner detector, in order to reduce backgrounds due to the long lived spallation products ^8He and ^9Li . This background is discussed in detail in section 5.2.2.
7. Fiducial volume - The prompt and delayed vertices are required to lie within 5.5 m of the center of the detector in order to reduce backgrounds due to neutrons from the rock and outer detector. These backgrounds are discussed in detail in section 5.2.5.

The data reducing effects of successive application of the selection criteria are shown in Table 5.1 for prompt energies in the range of 8.0 MeV to 16.2 MeV.

Cut	Events Remaining
No cuts	52131135
Prompt Energy	4571
Delayed Energy	150
Capture Time	128
Vertex Separation	72
Muon Veto	22
Shower Veto	7
Fiducial Volume	1

TABLE 5.1.: Data reduction for prompt energy between 8.0 MeV and 16.2 MeV.

One event with a prompt energy of 8.07 MeV and delayed energy of 2.16 MeV passed the selection criteria for $\bar{\nu}_e$'s produced by $^8\text{B } \nu_e \rightarrow \bar{\nu}_e$ transitions. No events

passed the selection criteria for super nova relic neutrinos or WIMP annihilation neutrinos (see Fig. 5.1).

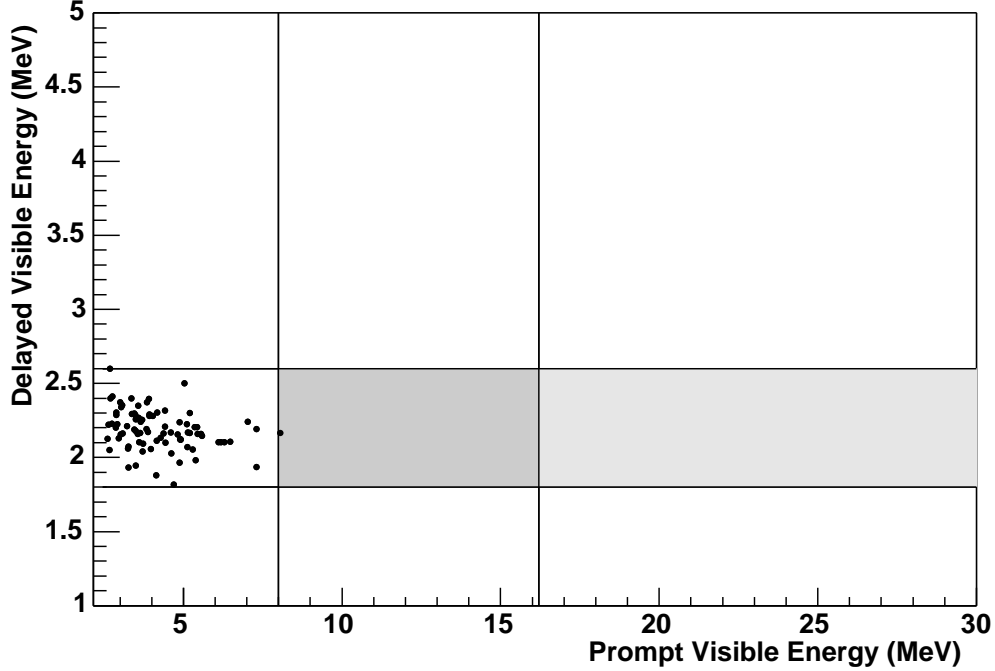


FIG. 5.1.: $\bar{\nu}_e$ candidate events with all cuts applied except the prompt and delayed energy cuts. The dark grey region, which contains one event, represents the region of interest to the search for $\bar{\nu}_e$'s from ${}^8\text{B}$ ν_e transitions. The light grey area represents the region of interest to the study of relic super nova $\bar{\nu}_e$'s and $\bar{\nu}_e$'s from WIMP annihilation. The cluster of events below 8.0 MeV are reactor $\bar{\nu}_e$'s.

5.2 Background Estimates

In order to understand the significance of the one event that passed our event selection criteria, it is important to understand what processes may contribute backgrounds to this measurement. Possible sources of background for this measurement include accidental coincidences between muons or spallation neutrons and low energy natural activity in the detector, spallation neutrons that capture

in the detector, atmospheric neutrinos, the decay of isotopes produced by muon interactions with ^{12}C in the detector, and the tail of the reactor neutrino spectrum. Each of these possibilities has been considered.

5.2.1 Uncorrelated Background

Uncorrelated backgrounds are the result of accidental coincidences between two independent processes, which just happen to fake the signature of an inverse beta-decay event. For the measurement discussed here, an event depositing at least 8 MeV in the scintillator is followed less than 1 ms later by an unrelated event that deposits energy in the scintillator consistent with neutron capture on hydrogen. The event vertices must also be reconstructed within 1.6 m of each other in order to pass the vertex separation cut.

Muons crossing the inner detector without triggering the water veto counter are a possible source of high energy singles. The inefficiency of the water veto has been estimated as 6% by measuring the ratio of the rate of muons crossing the scintillator without triggering the water veto to the rate of muons crossing the scintillator and triggering the water veto. Muons crossing scintillator typically deposit ~ 1.5 GeV; therefore, only muons that glance along the surface of the scintillator sphere will deposit less than 50 MeV (the threshold energy for tagging muons in the scintillator) in the scintillator. These events will be reconstructed very close to the surface of the balloon, and will not pass the fiducial volume cut. However, muons may pass through the oil buffer surrounding the scintillator, and produce Cerenkov light. Since Cerenkov light is not isotropic, the vertex of such an event may be reconstructed inside the fiducial volume.

Neutrons from muon spallation may also be a source of high energy deposits in the scintillator. Muons interacting in the materials in and around the detector produce neutrons with energies up to the range of GeV. These neutrons can scatter into the scintillator and deposit their kinetic energy. This, in coincidence with

some low energy source, may fake an inverse beta decay signal. Neutrons that scatter into the detector and then capture on hydrogen can imitate the prompt and delayed parts of inverse beta decay, but this background is correlated, and will be discussed in greater detail later in this chapter.

Other sources of high energy singles are the products of muon interactions in the detector. Liquid scintillator is approximately 90% carbon by mass. Muon interactions in scintillator results in the break up of carbon nuclei. The resulting lighter nuclei that have lifetimes longer than the 4 ms veto and decay energies greater than 8 MeV are shown in Table 5.2.

Isotope	Lifetime	Endpoint Energy (MeV)
¹² N	15.9 ms	17.3
¹² B	29.1 ms	13.4
⁹ C	182.5 ms	16.0
⁸ B	1.11 s	13.7
⁸ Li	1.21 s	16.0
¹¹ Be	19.9 s	11.5

TABLE 5.2.: High energy cosmogenic products.

The singles rate of events with energies greater than 8 MeV is 55 day^{-1} . No attempt has been made to determine the relative contribution of each of the high energy sources discussed above to the the total event rate.

The low energy delayed part of the accidental coincidence is primarily due to natural radioactivity in the scintillator and balloon. Uranium, Thorium, and Radon contamination results in a singles rate of 1.7 Hz in the energy range of 1.8 to 2.6 MeV.

While the high energy sources above are typically distributed uniformly in the scintillator, the low energy natural radioactivity is concentrated at the balloon, and along the z-axis, where the calibration source deployment system deposits trace amounts of activity when it is deployed. As a result of the complex distribution of activity, the accidental coincidence rate cannot be calculated

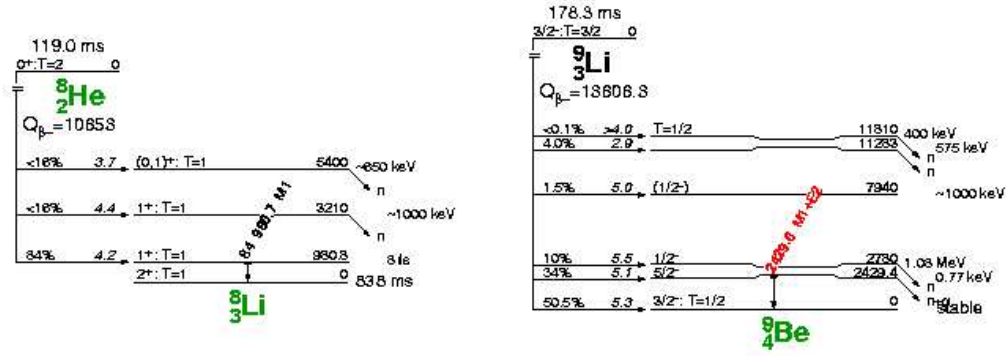
using the rates of each independent process. For this reason, the accidental coincidence rate was estimated by using an off-gate coincidence method. The full data set was used to estimate the background rate. The selection cuts described in section 5.1 were applied, but the coincidence time window was changed from 50 ns - 1 ms to 5 ms - 250 ms. The 5 ms delay ensures that no inverse beta decay events ($\sim 200 \mu\text{s}$ capture time) will pass the selection criteria ($\text{I}\beta\text{D} \int_{5000\mu\text{s}}^{250000\mu\text{s}} e^{-t/200} dt / \int_0^{1000\mu\text{s}} e^{-t/200} dt = 1.5 \times 10^{-12}$), while the 245 ms window (245 times the usual 1 ms window) should increase statistics and decrease the uncertainty in the measurement. With the modified selection cuts, no events passed. At the 90% confidence level, this result is consistent with maximum of 2.44 events. Dividing by 245 to scale to the window width of inverse beta decay gives an *upper limit* of 0.01 accidental coincidences in the 149 day sample.

5.2.2 Cosmogenic Backgrounds

In addition to the nuclei listed in 5.2, muon interactions with carbon also produce ^9Li and ^8He in the scintillator. These two unstable nuclei represent a source of correlated background, because the β^- -decay of the nucleus is followed by neutron emission. The prompt $\text{I}\beta\text{D}$ signal is imitated by the β^- , and the emitted neutron is captured on hydrogen, with the same capture time as that of an $\text{I}\beta\text{D}$ neutron, satisfying the delayed event condition. The halflives of ^9Li and ^8He are $T_{1/2} = 178 \text{ ms}$ and $T_{1/2} = 119 \text{ ms}$, respectively; therefore, the majority of these events occur outside of the usual 4 ms muon veto.

The β -decay endpoints of decays which lead to neutron emission for ^8He and ^9Li are listed in Table 5.3. Only the decays with β^- endpoints above 8 MeV will introduce background into the high energy $\bar{\nu}_e$ search, and only the solar $\bar{\nu}_e$ analysis is affected.

The first method used to eliminate these is to place a 2 second veto on the entire detector following muon showers, which are defined as muons that deposit more

FIG. 5.2.: The decay schemes for ^8He and ^9Li [1].

Isotope	β^- Endpoint Energy (keV)	Branching Ratio (%)
^8He	5258	16
	7448	16
^9Li	1796	0.1
	2323	4.0
	10826	10
	11177	34

TABLE 5.3.: Li^9 and He^8 delayed neutron β decays.

than 3 GeV in the detector. The 2 second veto is 99.9991% efficient for eliminating ^9Li decays, and 99.9582% efficient for eliminating ^8He decays. The rate of these showers is 0.017 Hz, which introduces 3% deadtime in the measurement of high energy $\bar{\nu}_e$'s. Candidate ^9Li and ^8He events can be found by looking for I β D-like events falling inside the 2 second post shower veto window. Figure 5.3 shows the prompt and delayed energies of possible ^9Li and ^8He events, with a prompt energy threshold of 2.6 MeV (the apparent 2.0 MeV threshold is due to histogram binning).

After identifying the candidate ^9Li and ^8He events, an attempt to separate the relative contribution of each isotope to the cosmogenic signal by fitting the decay time spectrum of the cosmogenic candidates was made. Since ^9Li and ^8He are

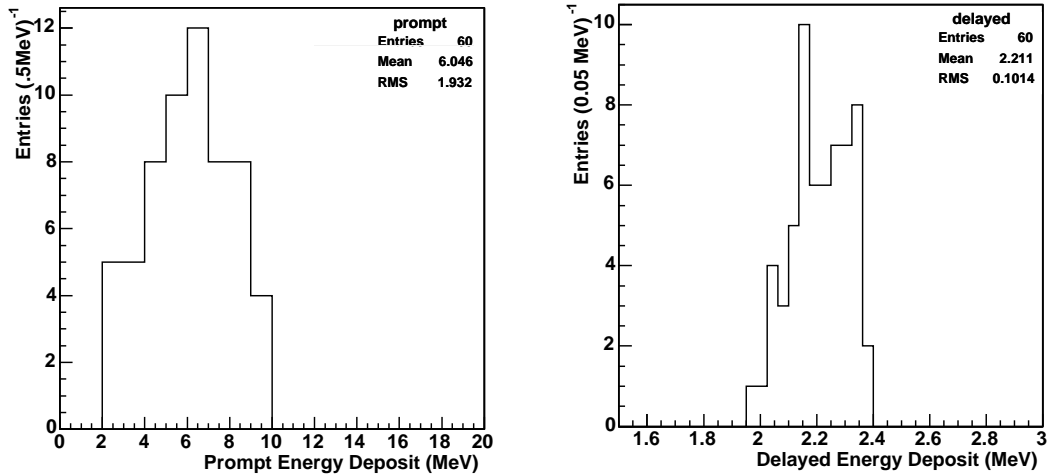


FIG. 5.3.: The left panel shows the prompt energy deposited by events that have been tagged as ${}^9\text{Li}$ or ${}^8\text{He}$ events in the scintillator. The right panel shows the energy spectrum of the delayed neutron capture, with the characteristic 2.2 MeV peak.

produced by muon passage through the detector, a histogram of the time between the passage of a muon and the decay of the produced ${}^9\text{Li}$ or ${}^8\text{He}$ nucleus should produce a distribution composed of an exponential with the decay time of ${}^9\text{Li}$ plus an exponential with the decay time of ${}^8\text{He}$. This distribution, referred to hereafter as the *time since last shower* distribution, since only ${}^9\text{Li}$ or ${}^8\text{He}$ occurring after a defined shower are tagged, was histogrammed for the events in Fig. 5.3, and is shown in Fig. 5.4. Fits to the sum of two exponentials, one with the decay time of ${}^9\text{Li}$, and the other with the decay time of ${}^8\text{He}$, were inconclusive in determining the relative contribution of ${}^9\text{Li}$ and ${}^8\text{He}$ in the data sample, due to the limited statistics; however, a qualitative comparison of the prompt energy distribution of data and the expected prompt energy distribution from ${}^9\text{Li}$ and ${}^8\text{He}$ suggests that

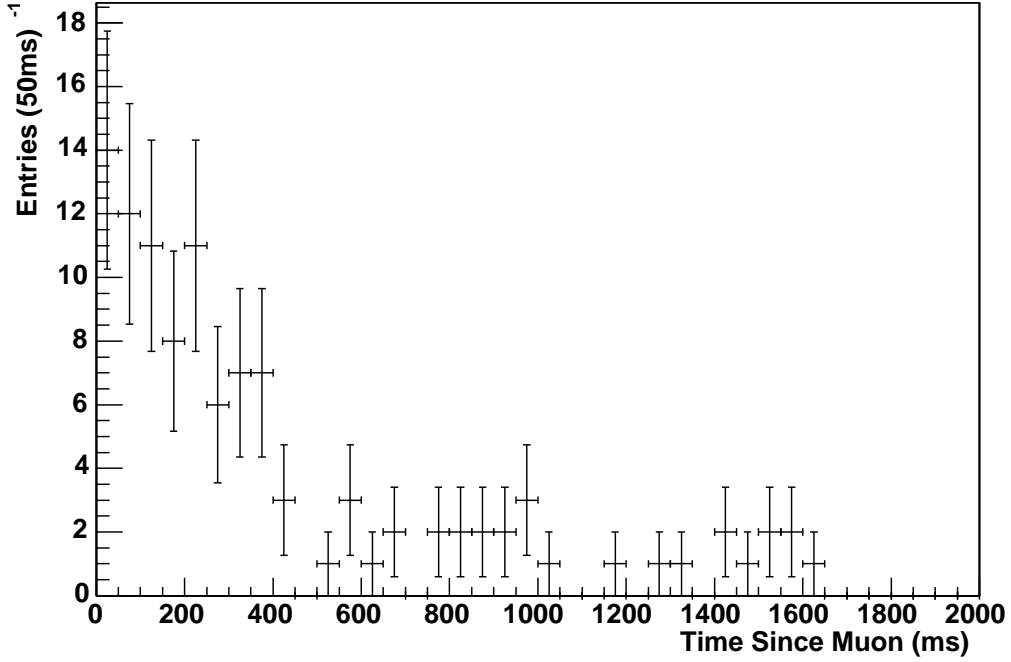


FIG. 5.4.: The time since muon shower distribution for events occurring within 2 seconds after a muon shower.

${}^9\text{Li}$ is the dominant source (see Fig. 5.5). For the remainder of this study, ${}^9\text{Li}$ is assumed to be the sole source of cosmogenic backgrounds.

The 2 second veto condition removes decays of ${}^9\text{Li}$ that are produced by muons showers, which are defined as muon events depositing more than 3 GeV in the scintillator; however, ${}^9\text{Li}$ may be produced by muons depositing less energy. To estimate this background, The threshold energy for muon showers is lowered from 3 GeV to 50 MeV in steps, and at each step the *time since last shower* distribution is made for events with prompt energy greater than 2.6 MeV. As the shower threshold energy is lowered, the shower rate increases. As this rate increases, the probability that a real $\bar{\nu}_e$ event will occur during the 2 second veto following a shower also increases. Table 5.4 summarizes the probability that a single $\bar{\nu}_e$ event will fall inside the veto time window for each muon shower threshold energy. As a

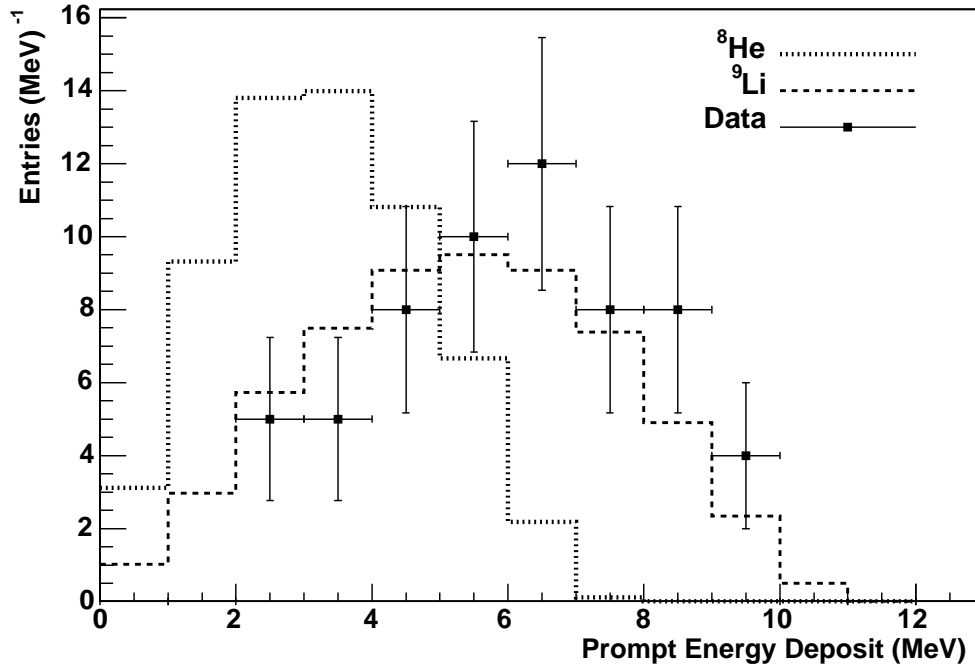


FIG. 5.5.: The prompt energy deposit from the β -decay of cosmogenics. A qualitative comparison of the data to expected ${}^9\text{Li}$ and ${}^8\text{He}$ spectra suggests the signal in KamLAND is primarily due to ${}^9\text{Li}$ decays.

result, the extracted ${}^9\text{Li}$ signal is contaminated by $\bar{\nu}_e$ events as the muon shower threshold is lowered.

To separate the ${}^9\text{Li}$ and $\bar{\nu}_e$ events in the data sample, for each threshold energy, the *time since last shower* distribution is fit to a two exponential function of the form:

$$f(t) = f_{{}^9\text{Li}}(t) + f_{\bar{\nu}_e}(t) \quad (5.1)$$

$$f_{{}^9\text{Li}}(t) = e^{(A - 3.89 \times 10^{-3}t)} \quad (5.2)$$

$$f_{\bar{\nu}_e}(t) = e^{(B - 4.02 \times 10^{-4}t)} \quad (5.3)$$

Where the time constant of $-3.89 \times 10^{-3} \text{ ms}^{-1}$ corresponds to the decay time of

Threshold Energy (MeV)	Rate (Hz)	Coincidence Probability
3000	1.7×10^{-2}	0.03
2500	2.5×10^{-2}	0.05
2000	4.9×10^{-2}	0.10
1500	0.12	0.24
1000	0.17	0.34
500	0.20	0.40
250	0.20	0.40
100	0.22	0.44
50	0.29	0.58

TABLE 5.4.: Muon shower rates for varying muon shower threshold energies. The coincidence probability indicates the probability that a real $\bar{\nu}_e$ event will be eliminated by the 2 second post shower cut, given the muon shower rate listed.

${}^9\text{Li}$, and the time constant of $-4.02 \times 10^{-4} \text{ ms}^{-1}$ represents the distribution of time differences between muon showers and randomly occurring neutrino events, which is obtained by fitting the time since muon shower distribution for singles events with energies between 8 MeV and 20 MeV (see Fig. 5.6). The contributions of ${}^9\text{Li}$ and $\bar{\nu}_e$'s to the distribution are then calculated by evaluating the expressions:

$$N_{9Li} = \frac{\int_{4ms}^{2000ms} f_{9Li}(t)dt}{\int_{4ms}^{2000ms} f(t)dt} N_{tss} \quad (5.4)$$

$$N_{\bar{\nu}_e} = \frac{\int_{4ms}^{2000ms} f_{\bar{\nu}_e}(t)dt}{\int_{4ms}^{2000ms} f(t)dt} N_{tss} \quad (5.5)$$

where N_{9Li} and $N_{\bar{\nu}_e}$ are the number of ${}^9\text{Li}$ and $\bar{\nu}_e$ events, respectively, and N_{tss} is the total number of events in the *time since last shower* distribution. Figure 5.7 shows the results of this process for each muon shower thresholds.

The total expected ${}^9\text{Li}$ background with prompt energy above 2.6 MeV and muon shower threshold of 0 MeV is then estimated by fitting a 1st order polynomial to the ${}^9\text{Li}$ events curve in Fig. 5.7. The y-intercept of the fit, which corresponds to the number of ${}^9\text{Li}$ events at a muon shower threshold of 0 MeV, is found to be 45.72 ± 1.11 events.

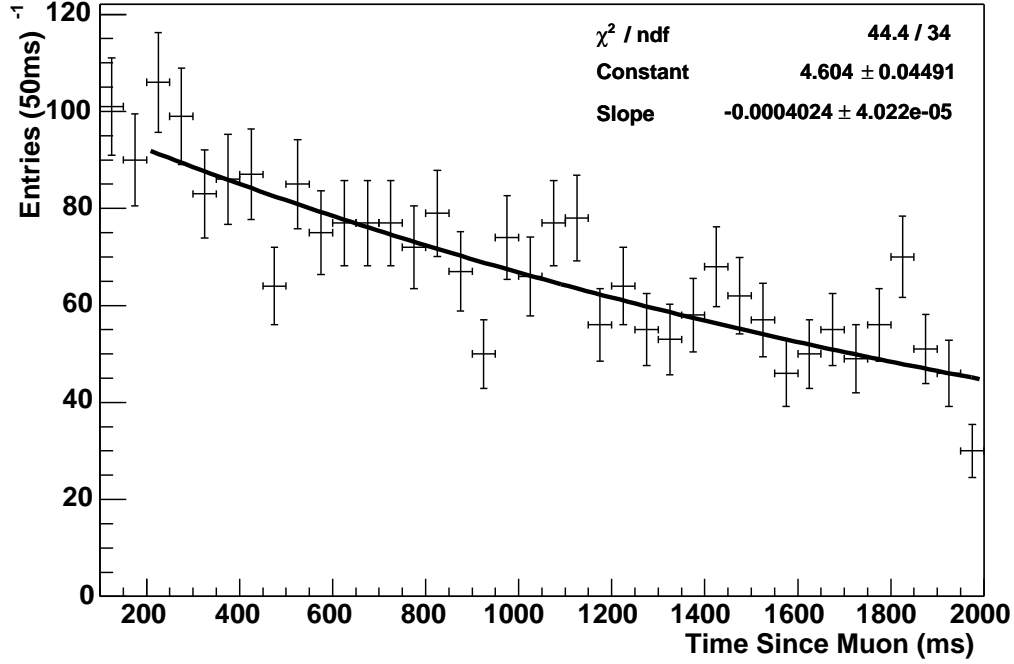


FIG. 5.6.: The time difference between muons and singles events with energies between 8 MeV and 20 MeV is fit to determine decay constant for the distribution of muon/ $\bar{\nu}_e$ time differences.

The number of ^9Li decays following showers with the 3 GeV threshold is 40.35 ± 3.86 . These events will be decayed by the 2 second post shower veto cut that is applied during events selection; Therefore, $45.72 - 40.35 = 5.37 \pm 3.19$ ^9Li decays will remain in the $\bar{\nu}_e$ data set, with prompt energies above 2.6 MeV. The expected background above 8.0 MeV prompt energy is found by scaling this number to the ratio of the number ^9Li decays above 8.0 MeV to the number of ^9Li decays above 2.6 MeV, as illustrated by eq. 5.6:

$$N_{^9\text{Li}}^{8.0\text{MeV}} = \frac{\int_{8.0\text{MeV}}^{16.2\text{MeV}} N(E)dE}{\int_{2.6\text{MeV}}^{16.2\text{MeV}} N(E)dE} N_{^9\text{Li}}^{2.6\text{MeV}} \quad (5.6)$$

where $N_{^9\text{Li}}^{2.6\text{MeV}} = 5.37 \pm 3.19$ events, and the ratio of integrals equals 0.14. The

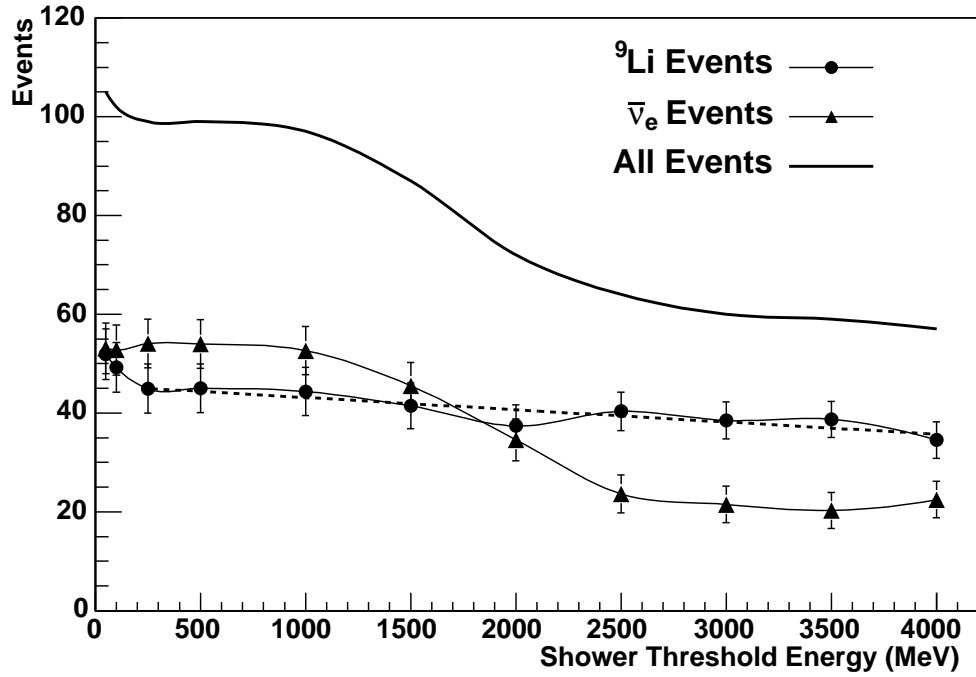


FIG. 5.7.: ${}^9\text{Li}$ and $\bar{\nu}_e$ events as a function of muon shower threshold. The dotted line indicates a linear fit to the ${}^9\text{Li}$ curve, and has a y-intercept of 45.61 events.

expected un-vetoed ${}^9\text{Li}$ contribution to the high energy neutrino measurement is, therefore, $N_{9\text{Li}}^{8.0\text{MeV}} = 0.75 \pm 0.45$ events in 149 days.

5.2.3 Atmospheric Neutrinos

Cosmic rays, composed primarily of protons and He nuclei, interact with nuclei in the atmosphere to produce charged Pions and Kaons. The decays of these mesons produce electron anti-neutrinos as illustrated by equation 3.1. The charge conjugate reactions also occur, but do not yield $\bar{\nu}_e$'s.

$$\begin{aligned}\pi^- &\rightarrow \mu^- + \bar{\nu}_\mu, K^- \rightarrow \mu^- + \bar{\nu}_\mu \\ \mu^- &\rightarrow e^- + \bar{\nu}_e + \nu_\mu\end{aligned}\tag{5.7}$$

The flux of atmospheric $\bar{\nu}_e$'s has been calculated in [37] above 50 MeV for the Kamioka mine site, and is shown in Fig. 5.8. In order to evaluate the expected signal due to the atmospheric neutrino flux at KamLAND, the flux is assumed to be flat from 0 to 40 MeV. The flux from 20 - 40 MeV is given as $3.4 \text{ (m}^2 \text{ sr s)}^{-1}$. Then in the energy range of 8.8-17 MeV the flux is simply $3.4 \times (8.2/20) = 1.4 \text{ (m}^2 \text{ sr s)}^{-1}$. The expected number of events in KamLAND can be calculated as

$$N_{atm} = \Phi_{atm} \times \bar{\sigma} \times \epsilon \times T \times N_p \quad (5.8)$$

where $\bar{\sigma} = 2.2 \times 10^{-41} \text{ cm}^2$ is the cross section averaged over the atmospheric neutrino flux between 8.8 and 17 MeV, $\epsilon = .85$ is the detection efficiency, $T = 1.3 \times 10^7 \text{ s}$ is the experimental livetime, and $N_p = 4.6 \times 10^{31}$ is the number of target protons. This leads to an expected atmospheric neutrino contribution of 2.0×10^{-5} events. The atmospheric neutrino flux is actually decreasing for lower energies, so this estimate represents a conservative upper limit, which is much smaller than the total background due to all other sources. The background due to atmospheric neutrinos is, therefore, considered insignificant.

5.2.4 Reactor Neutrinos

The main objective of the first phase of KamLAND is to measure the flux of neutrinos from reactors in Japan and Korea in order to test the LMA solution to the solar neutrino problem. The first results of this measurement, which have been recently published [15], support the LMA oscillation hypothesis. While the neutrino spectrum is nearly vanishing at neutrino energies above 8.8 MeV, the tail of the spectrum extends, with very small intensity, above this threshold. The effect of detector energy resolution may also lead to events with energy below the 8.8 MeV threshold being reconstructed with energies above the threshold. Since there are more actual events below the threshold than above it, the net effect of detector resolution will be an increase in the number of events above the threshold.

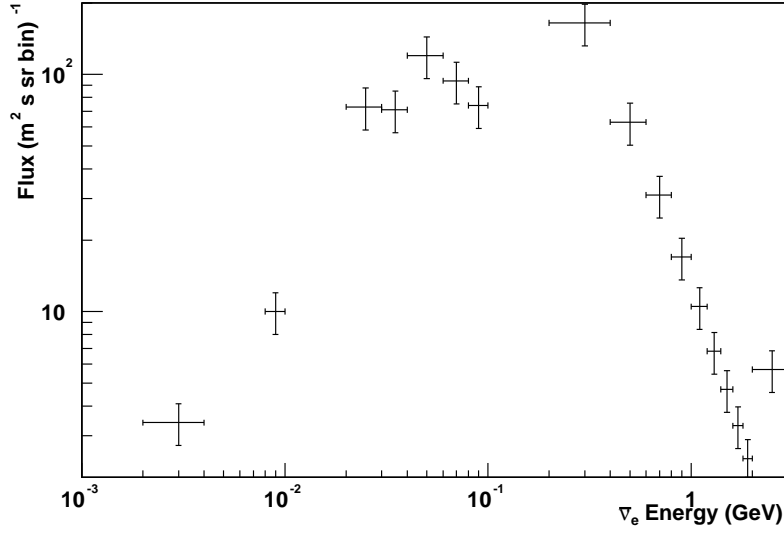


FIG. 5.8.: The flux of atmospheric $\bar{\nu}_e$'s at the Kamioka site. Error bars represent the 20% uncertainty in the flux normalization, and do not include model uncertainties.

To determine the expected background from reactor anti-neutrinos, the anti-neutrino flux from all Japanese and Korean reactors was evaluated. The fission rates for ^{235}U , ^{238}U , ^{239}Pu , and ^{241}Pu have been provided for each Japanese reactor by the Japanese power companies. This data is provided on a weekly basis during regular reactor running, and on an hourly basis during reactor power on/off cycles. The anti-neutrino production, based on the reactor fission rates, is integrated over the life time of the measurement for each reactor to find the anti-neutrino output from each reactor.

The flux at KamLAND is then found by reducing the flux at the reactor by the factor $4\pi/r^2$, where r is the distance to the reactor from KamLAND. To account for neutrino oscillations, The flux is adjusted by the $\bar{\nu}_e \rightarrow \bar{\nu}_e$ probability ($\bar{\nu}_e$ survival probability),

$$P(\bar{\nu}_e \rightarrow \bar{\nu}_e) = 1 - \sin^2 2\theta \sin^2 \left(\frac{1.27 \Delta m^2 L}{E} \right), \quad (5.9)$$

where $\sin^2 2\theta$ is the mixing parameter, Δm^2 is the difference of the squared masses of the neutrino eigenstates, L is the distance from the source to the detector, and E is the neutrino energy.

Figure 5.9 shows the expected anti-neutrino spectrum at KamLAND for the 149 day livetime of this measurement assuming the LMA neutrino oscillation global best fit values of $\sin^2 2\theta = 0.85$ and $\Delta m^2 = 5.5 \times 10^{-5} \text{ eV}^2$.

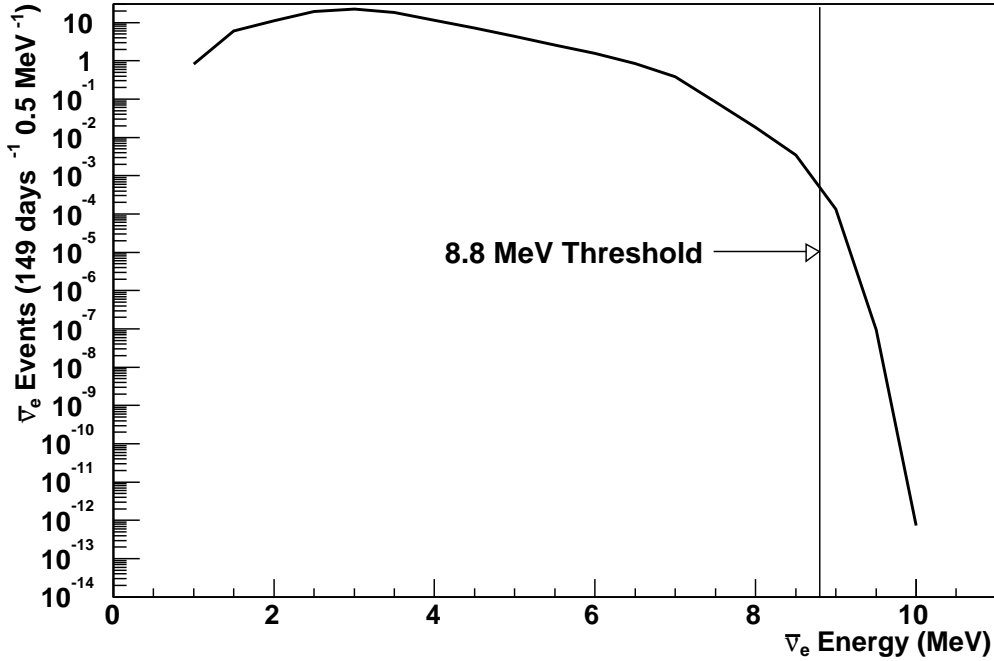


FIG. 5.9.: The reactor $\bar{\nu}_e$'s spectrum at KamLAND assuming LMA oscillations. The log scale is used in order to visualize the the extremely small signal above 8.8 MeV.

To account for the uncertainties in the LMA oscillation parameters, the calculation is repeated for values of Δm^2 and $\sin^2 2\theta$ that cover the 90% C.L. region of the LMA solution. For each point in the the rectangle defined by

$3.0 \times 10^{-5} eV^2 < \Delta m^2 < 2.5 \times 10^{-4} eV^2$ and $0.75 < \sin^2 2\theta < 1.0$, the number of events with energies above 8.8 MeV, including detector energy resolution, is calculated. The results of this calculation are shown in Fig. 5.10. The result of each trial is histogrammed (see Fig. 5.11), and the mean of the distribution is taken as the expected background to the high energy $\bar{\nu}_e$ measurement, and an error is assigned to include the entire range of possible background values. The resulting value of 0.015 ± 0.010 is obtained for the background due to reactor anti-neutrinos.

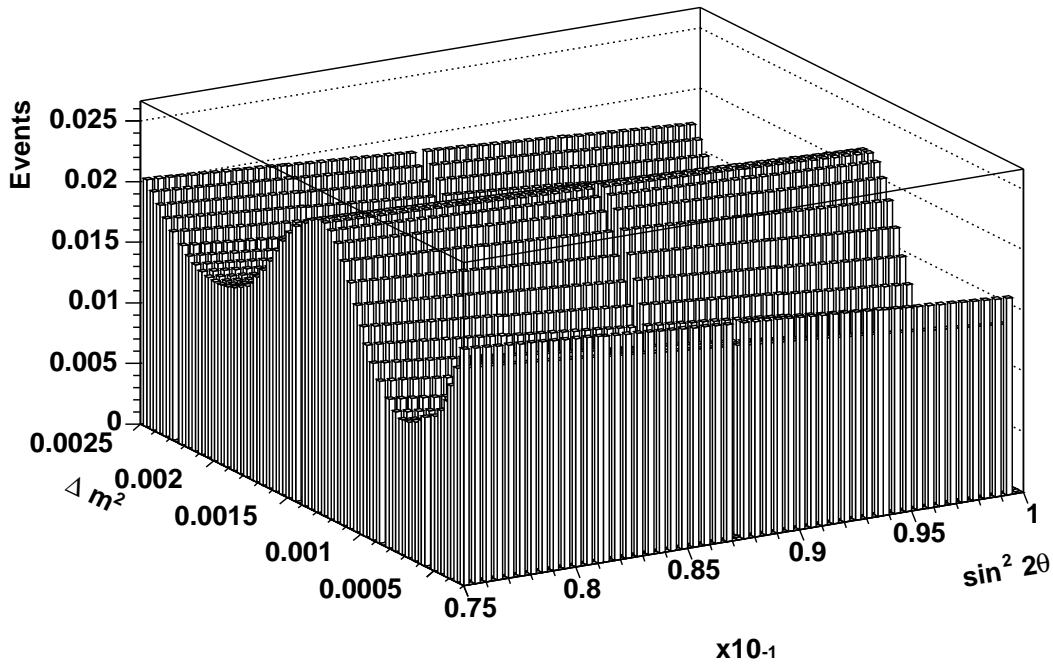


FIG. 5.10.: The background expected above the anti-neutrino energy of 8 MeV from reactor $\bar{\nu}_e$'s at KamLAND as a function of neutrino mixing parameters.

5.2.5 Neutrons from Cosmic Muons

Neutrons from cosmic neutrons are a source of background for $\bar{\nu}_e$ searches because the neutron signal is indistinguishable from inverse beta decay. Neutrons

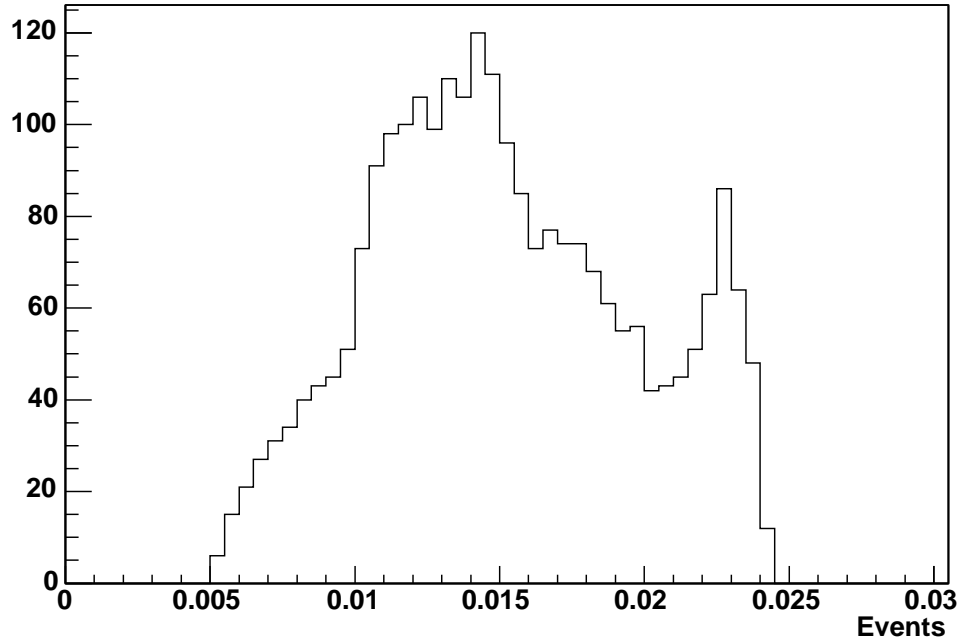


FIG. 5.11.: The background expected above the prompt energy of 8 MeV from reactor $\bar{\nu}_e$'s at KamLAND, histogrammed for the entire range of mixing parameters. The mean of the distribution is taken as the expected background contribution. An error is assigned which includes the entire range of possible background values.

in scintillator deposit their kinetic energy quickly, imitating the prompt portion of $I\beta D$. The neutrons then capture on hydrogen, with a mean capture time of ~ 200 μs , which is the capture time of the neutron produced in $I\beta D$.

Muon interactions with matter in and around the detector produce neutrons through the following processes:

1. Muon spallation is the process by which nuclear disintegrations are initiated by the exchange of a virtual photon between the muon and nuclei in matter. The products of the nuclear disintegrations include neutrons, which are produced in the detector, and travel into the detector from the surrounding material.

2. Photo-nuclear interaction produce neutrons and pions through photo-production in nuclei. Neutrons are generated through the (γ, n) reaction, and multiple neutrons are produce in the (γ, in) reaction.
3. Elastic scattering of muons with nuclei results in the liberation of neutrons from nuclei.
4. Nuclear capture of muons, which converts a nuclear proton into a neutron which may be ejected from the nucleus.
5. Secondary and Tertiary neutrons are produced through interactions of neutrons produced in the above ways with nuclei in matter.

A detailed study of the production of neutrons at KamLAND has been carried and reported in [33].

KamLAND's outer water detector is 94% efficient at tagging muons that pass through it, while the inner detector is $\sim 100\%$ efficient. Tagging muons in the outer and inner detector allows us to ignore inverse beta decay-like events that occur soon after the passage of a muon, since these events are most likely due to neutrons produced by muon interactions. There is, however, still 6% of neutrons produced in water without being tagged by the water detector. Also, any neutrons produced in the rock by muons that do not pass through the water detector cannot be tagged, and may travel into the inner detector and produce background events.

In order to estimate the contribution of neutrons to the measurement of high energy $\bar{\nu}_e$'s, GEANT3 based monte carlo simulations have been performed using the simulation described in Section 2.4.

The energy distribution of neutrons produced by cosmic muons is parametrized by the expression $N(E) = E^{-1.86}$ [38], with production rates of $5.8 \times 10^3 \text{ day}^{-1}$ and $1.6 \times 10^4 \text{ day}^{-1}$ in rock and water, respectively [33].

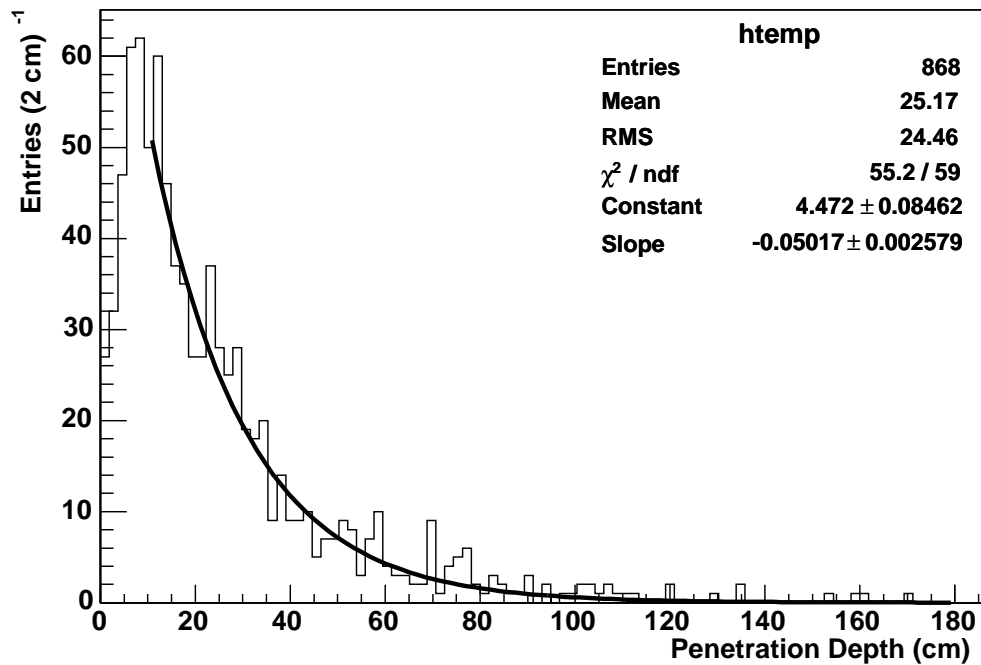


FIG. 5.12.: Penetration into scintillator for neutrons generated in water. The fit results shown are for a simple $\exp(\text{constant} + \text{slope} \times x)$.

5.2.5.1 Neutrons from Water

To estimate the background contribution to inverse beta decay in the scintillator from neutrons produced in the water veto, twenty million neutrons were generated in water. When neutrons traveled into the scintillator, selection cuts for inverse beta decay were applied: prompt energy deposit greater than 8.0 MeV and less than 16.2 MeV (corresponding to neutrino energies between 8.8 and 17.0 MeV) followed 50 ns to 1 ms later by a delayed energy deposit between 1.8 MeV and 2.6 MeV. The prompt and delayed vertices are required to be within 1.6 m of one another. These cuts represent the values used in the search for solar ^8B $\nu_e \rightarrow \bar{\nu}_e$ transitions. Of the 20 million events generated in water, 868 passed the selection cuts.

Parameter	Value	Error
Constant	4.472	0.08462
Slope	-0.05017	0.002579
N_{hist}	868	29.4

TABLE 5.5.: Fit parameters for neutron penetration in scintillator.

Figure 5.12 shows the distribution for neutron penetration depth in scintillator ($x = 650\text{cm} - r_{prompt}$). The distribution is fit with a simple exponential, $\exp(\text{constant} + \text{slope} \cdot x)$, with the fit parameters and errors given in Table 5.5 with the number of entries in the histogram, and its statistical uncertainty.

The number of events inside the fiducial volume can be calculated as:

$$N_{r < 550\text{cm}} = \frac{\int_{550\text{cm}}^{650\text{cm}} e^{(\text{constant} - \text{slope} \cdot x)} dx}{\int_{0\text{cm}}^{650\text{cm}} e^{(\text{constant} - \text{slope} \cdot x)} dx} N_{hist} \quad (5.10)$$

where N_{hist} is the number of entries in the histogram, and has an uncertainty of $\sqrt{N_{hist}}$ (see Table 5.5).

The uncertainty in $N_{r < 550\text{cm}}$ is calculated using a Monte Carlo technique. A value for N_{hist} is taken at random from a Gaussian distribution with center equal to N_{hist} and width equal to $\sqrt{N_{hist}}$. Since the slope and constant of the exponential fit function are not independent, their correlation must be considered when choosing values. For the case of two dependent variables, each having a Gaussian error, the probability distribution is represented by the 2-dimensional Gaussian function [39]:

$$f = \frac{1}{2\pi\sigma_1\sigma_2\sqrt{1-\rho^2}} \exp\left\{\frac{-1}{2(1-\rho^2)}\left[\frac{(x_1-\mu_1)^2}{\sigma_1^2} - \frac{2\rho(x_1-\mu_1)(x_2-\mu_2)}{\sigma_1\sigma_2} + \frac{(x_2-\mu_2)^2}{\sigma_2^2}\right]\right\} \quad (5.11)$$

Where x_1 and x_2 are the central value for the constant and slope, respectively, and σ_1 and σ_2 are their respective uncertainties. $\rho_{ij} = V_{ij}/\sigma_i\sigma_j$, and V_{ij} are the covariance matrix elements calculated by the fitter, with the values:

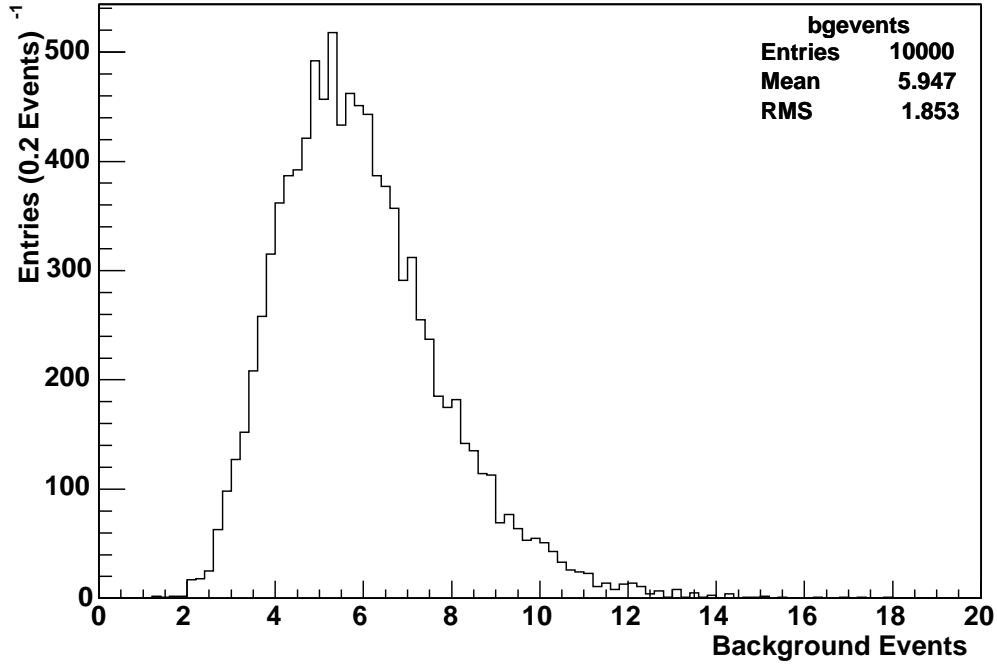


FIG. 5.13.: The calculated number of events inside the 550 cm fiducial volume, for 20 million events generated in water.

$$V = \begin{pmatrix} 7.16037 \times 10^{-3} & -1.90326 \times 10^{-4} \\ -1.90326 \times 10^{-4} & 6.6497 \times 10^{-6} \end{pmatrix}.$$

Values for the exponential constant' and slope' are generated according to eq.5.11, and a “guess”, $N'_{r<550cm}$ is calculated for the number of events in the fiducial volume by inserting N'_{hist} , constant', and slope' into eq. 5.10.

This process is repeated 10,000 times, and the distribution of $N'_{r<550cm}$ is histogrammed. The mean value of the distribution is taken as the value for $N_{r<550cm}$ and its RMS is taken as the error in this quantity.

The number of events inside the fiducial volume is calculated as 5.9 ± 1.9 . This number must now be scaled to the experimental livetime and the veto inefficiency. The number of background events expected from neutrons produced by muons in water is then given by:

$$N_{n \text{ from water}} = N_{r < 550 \text{ cm}} \frac{\text{Neutron Production Rate In Water}}{\# \text{ of neutrons generated}} \times (\text{experimental lifetime})(\text{veto inefficiency}). \quad (5.12)$$

Recall that the neutron production rate in water is $1.6 \times 10^4 \text{ day}^{-1}$, and the veto inefficiency is 6%. The expected background from neutrons produced in the water veto for the measurement of high energy $\bar{\nu}_e$'s ($8.8 \text{ MeV} < E_{\bar{\nu}_e} < 17.0 \text{ MeV}$) in the KamLAND 5.5 meter fiducial volume is 0.0425 ± 0.0133 .

This analysis has been repeated for prompt energies between 16.2 MeV and 35 MeV in the scintillator, for the purpose of estimating the background expected in searches for higher energy $\bar{\nu}_e$'s such as super nova relic neutrinos, and neutrinos from WIMP annihilations. In this energy range, the expected background is 0.68 ± 0.05 events in 149 days in the 5.5 meter fiducial volume.

5.2.5.2 Neutrons from Rock

The calculation of background contribution of neutrons from muons in the rock surrounding the detector is identical to the calculation for neutrons produced in water, with 100% veto inefficiency, since muons passing through the rock cannot be vetoed. The GEANT simulation was used to generate 40 million events in the rock surrounding the detector. The penetration depth of neutrons travelling into scintillator from rock is shown in Fig. 5.14 for neutrons depositing between 8.0 and 16.0 MeV in scintillator.

The distribution was again fit with the function $\exp(\text{constant} + \text{slope} \cdot x)$, with the results shown in Table 5.6. The covariance matrix which describes the correlation between the constant and slope parameters of the fit is given by:

$$V = \begin{pmatrix} 1.69262 \times 10^{-2} & -4.30349 \times 10^{-4} \\ -4.30349 \times 10^{-4} & 1.44333 \times 10^{-5} \end{pmatrix}$$

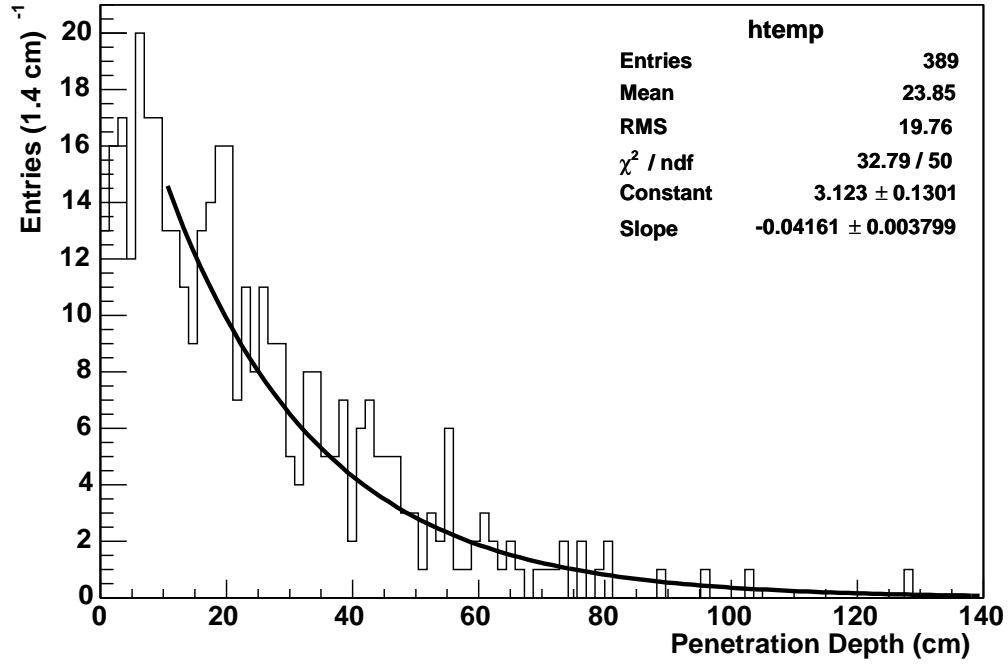


FIG. 5.14.: Penetration into scintillator for neutrons generated in rock. The fit results shown are for a simple $\exp(\text{constant} + \text{slope} \cdot x)$.

The analysis described in the section above was repeated to determine the number of events inside the 5.5 meter fiducial volume. The results are shown in Fig. 5.15 for prompt energy deposit between 8.0 MeV and 16.2 MeV. The number of events expected in the 5.5 meter fiducial volume for 40 million neutrons produced in the rock is $N_{r < 550} = 6.524 \pm 2.811$. The expected number of background events from neutrons from rock in our 149 day data sample is then given by:

$$N_{n \text{ from rock}} = N_{r < 550 \text{ cm}} \frac{\text{Neutron Production Rate In Rock}}{\# \text{ of neutrons generated}} \times (\text{experimental livetime})(\text{veto inefficiency}), \quad (5.13)$$

where the neutron production rate in rock is 5.8×10^3 , and the veto inefficiency is 100%. The expected background from this source is 0.1410 ± 0.0607 events in

Parameter	Value	Error
Constant	3.123	0.1301
Slope	-0.04161	0.003799
N_{hist}	389	19.72

TABLE 5.6.: Fit parameters for neutron penetration in scintillator.

149 days with prompt energy between 8.0 and 16.2 MeV.

The analysis has been repeated for prompt energies in the range of 16.2 MeV to 30 MeV. In this case, the expected background is 1.038 ± 0.117 events in 149 days.

5.2.6 Summary of Backgrounds

The summary of calculated backgrounds is shown in Table 5.7 for the solar $\bar{\nu}_e$ analysis, and other analyses with higher prompt energy thresholds. The total expected backgrounds are 0.95 ± 0.45 events in the 8.0 - 16.2 MeV neutrino energy range, and 1.72 ± 0.12 events in the 16.2 - 30 MeV neutrino energy range.

Source	Solar	Higher Energy
Accidentals	< 0.01	< 0.01
^9Li	0.75 ± 0.45	0.0
Atmospheric $\bar{\nu}_e$'s	$<< 0.01$	$<< 0.01$
Reactor $\bar{\nu}_e$'s	0.02 ± 0.010	0.0
Fast Neutrons	0.18 ± 0.06	1.72 ± 0.12
Total	$0.95 \pm .45$	1.72 ± 0.12

TABLE 5.7.: Summary of backgrounds for the solar $\bar{\nu}_e$ analysis, with prompt energies of 8.8 - 17.0 MeV, and higher energy analyses, with prompt energies of 17.0 - 30.0 MeV.

5.3 Electron Anti-Neutrino Flux Calculation

The expected number of neutrino events observed in KamLAND can be written as:

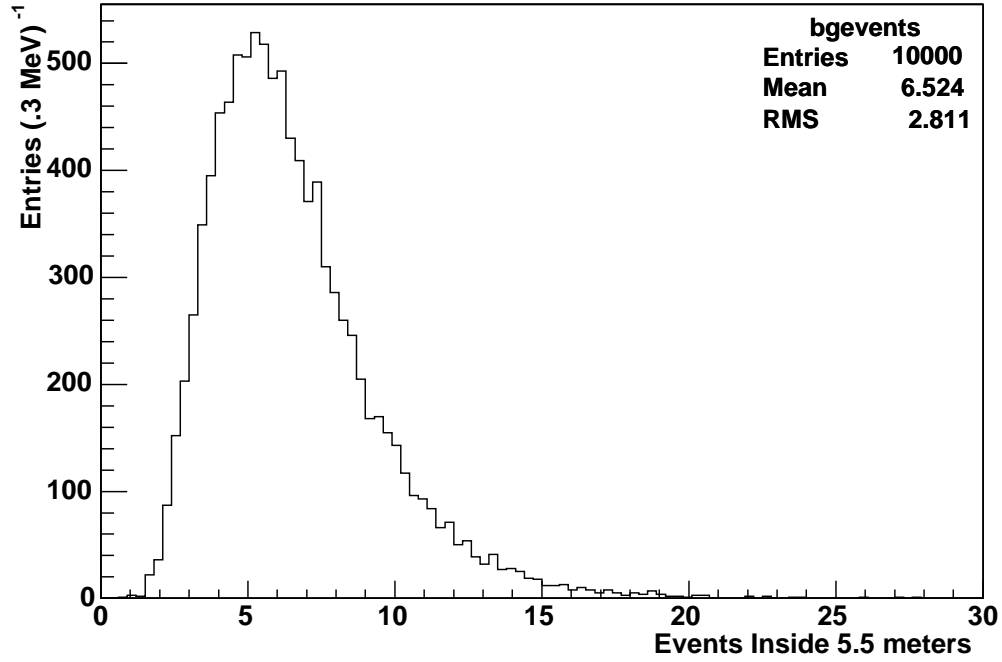


FIG. 5.15.: The calculated number of events inside the 550cm fiducial volume, for 40 million events generated in rock.

$$N_{signal} = \int \Phi_{\bar{\nu}_e}(E) \epsilon(E) \sigma(E) dE \times N_p \times f_v \times T, \quad (5.14)$$

where $\Phi_{\bar{\nu}_e}(E)$ is the energy dependent $\bar{\nu}_e$ flux, $\epsilon(E)$ is the detection efficiency, $\sigma(E)$ is interaction cross section, $N_p \times f_v$ is the number of protons in the fiducial volume, T is the detector live time, and the integral is taken over the energy range of interest to this study. It will be shown in section 5.3.2 that $\epsilon(E) \simeq \bar{\epsilon}$ can be treated as a constant in the energy range of this study, therefore eq. 5.14 can be rewritten as:

$$N_{signal} = \int \Phi_{\bar{\nu}_e}(E) \times \sigma(E) dE \times \bar{\epsilon} \times N_p \times f_v \times T. \quad (5.15)$$

and we can use the definition of the average value of $\sigma(E)$ to write

$$\bar{\sigma} = \frac{\int_{E_1}^{E_2} \Phi_{\bar{\nu}_e}(E) \sigma(E) dE}{\int_{E_1}^{E_2} \Phi_{\bar{\nu}_e}(E) dE}, \quad (5.16)$$

where $\Phi_{\bar{\nu}_e}^{total} = \int_{E_1}^{E_2} \Phi_{\bar{\nu}_e}(E) dE$ is simply the total $\bar{\nu}_e$ flux with energies between E_1 and E_2 . Then

$$\int_{E_1}^{E_2} \Phi_{\bar{\nu}_e}(E) \sigma(E) dE = \Phi_{\bar{\nu}_e}^{total} \times \bar{\sigma}. \quad (5.17)$$

This allows us to rewrite eq. 5.15 as:

$$N_{signal} = \Phi_{\bar{\nu}_e}^{total} \bar{\sigma} \times \bar{\epsilon} \times N_p \times f_v \times T, \quad (5.18)$$

or

$$\Phi_{\bar{\nu}_e}^{total} = \frac{N_{signal}}{\bar{\sigma} \times \bar{\epsilon} \times N_p \times f_v \times T}. \quad (5.19)$$

If the energy dependence of the nuebar spectrum is known, the value of $\bar{\sigma}$ can be calculated according to eq. 5.16, while the other quantities in the denominator are known. The total flux of $\bar{\nu}_e$'s in some energy range can then be determined from the number of observed IBD events in KamLAND according to eq. 5.19.

5.3.1 $\bar{\sigma}$ Calculations

The average cross sections have been calculated using 5.16 for the case of the $\bar{\nu}_e$ spectrum having the spectral shape of the solar ^8B ν_e spectrum [40], and the case of the $\bar{\nu}_e$ spectrum have the shape of the relic super nova neutrino spectrum [41] within the prompt energy limits of this study. For neutrino energies between 8.8 and 17.0 MeV distributed according to the solar ^8B spectrum, the average cross section is $7.94 \times 10^{-42} \text{ cm}^2$. For neutrino energies between 17.0 and 30.0 MeV distributed according to the relic super nova $\bar{\nu}_e$ spectrum, the average cross section is $3.64 \times 10^{-41} \text{ cm}^2$. Neglecting the outer radiative corrections introduces a systematic uncertainty of 3-4% in the average cross section [42].

5.3.2 Detection Efficiency

The detection efficiency for $I\beta D$ in KamLAND has been estimated using the GEANT3 based Monte Carlo described in section 2.4. The effects of detector energy and position resolution are included in the simulation. The positron and neutron from $I\beta D$ are generated uniformly throughout the KamLAND scintillator. The results are shown in Fig. 5.16 as a function of positron energy (recall from section 4.1 that the $\bar{\nu}_e$ energy is simply related to the positron energy by the relationship $E_{\bar{\nu}_e} = E_{e^+} + \Delta$ for the case of an infinitely massive neutron). The error bars represent the statistical uncertainty in the efficiency resulting from the finite number of events generated in the Monte Carlo. The plot is consistent with a constant value, taken as the average of all the data points at 0.856. The uncertainty in the calculated mean is 0.005; however, the assumption that the detection efficiency does not depend on the energy may be incorrect. For this reason, a systematic uncertainty has been assigned which includes the 1 sigma errors on the efficiency calculation at each energy. The total error is indicated by the grey region in Fig. 5.16. The resulting value for the detection efficiency of $I\beta D$ in KamLAND is 0.856 ± 0.021 in the energy range of this study.

5.3.3 Target Protons: $N_p \times f_v$

The number of protons in the fiducial volume can be calculated from the known density and chemical composition of KamLAND scintillator. The scintillator in KamLAND is composed of 80% paraffin, 20% pseudocumene, and 1.5 g/L PPO, with a density of 0.778 g/cm³ and H/C ratio of 1.969. In the 5.5 meter spherical fiducial volume, there are 4.60×10^{31} hydrogen nuclei that are potential targets for $I\beta D$.

The systematic uncertainty in the number of target protons, which is an effect of biases in the vertex fitter, has been estimated by analyzing the anisotropy of

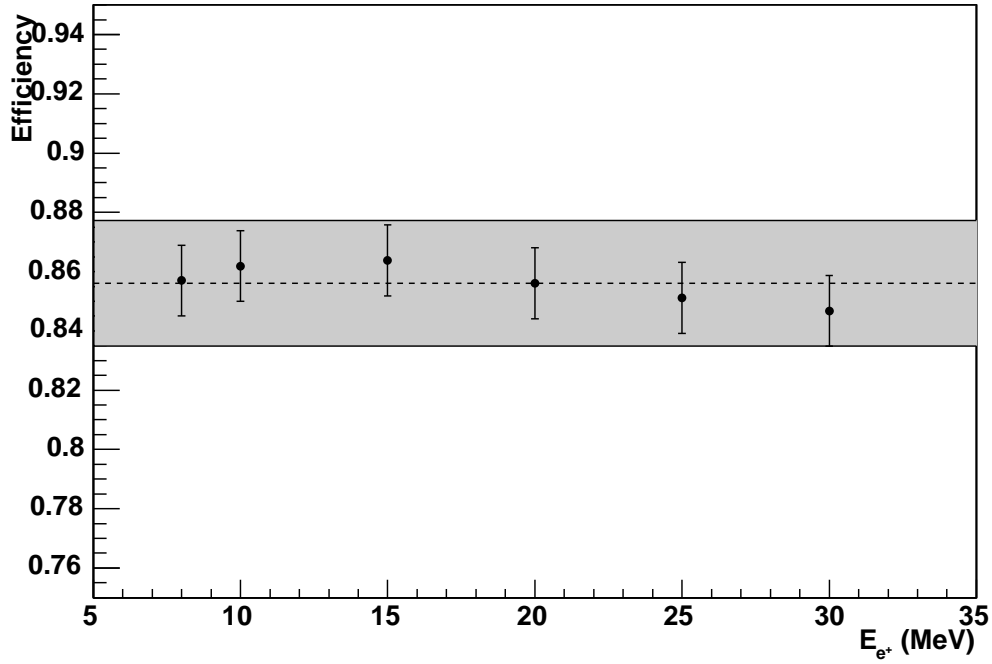


FIG. 5.16.: The detection efficiency for inverse beta decay in KamLAND as a function of positron energy. The dotted line represents the average value, and the grey region indicates the uncertainty.

muon spallation products in the detector. ^{12}B nuclei are produced isotropically throughout the detector by cosmic muon interactions with ^{12}C . Since the production rate has no radial dependence, the number of neutron captures in a sphere with radius r will be given by:

$$N_B = \frac{4}{3}\pi r^3 RT, \quad (5.20)$$

where R is the ^{12}B production rate per unit volume and T is the run time of the measurement. Since the ^{12}B production is independent of the radius, and R and T are constants, a plot of N_B vs. r^3 should be a line with zero slope. If, however, there are biases in the vertex fitter for events occurring away from the z -axis (which is where the vertex fitter is calibrated), the plot of N_B vs. r^3 will

be non-linear, or will have a slope. Figure 5.17 shows the distributions of r^3 , $\cos\theta$, and ϕ for ^{12}B decays in scintillator. The distributions show uniformity in $\cos\theta$ and ϕ , but there is an apparent bias towards larger values of r^3 .

The overall uncertainty in the number of target protons due to the bias in r^3 has been evaluated by counting events in spheres with radii of 7.0 m, 6.5 m, 6.0 m, 5.5 m, 5.0 m, and 4.5 m. The event density, or number of events per unit volume, is calculated for each sphere. the uncertainty in the number of protons for each sphere can be estimated by comparing the event density for each sphere with the event density for the entire detector with no fiducial volume cut. Table 5.8 shows the ratio of the number of events inside each fiducial volume to the number of events with no fiducial volume cut. Based on this study, the number of target protons should be decreased by 8.5% to account for the vertex fitter bias. The remaining uncertainty is due to finite statistics. The result for the number of target protons is $(4.20 \pm .12) \times 10^{31}$.

Fiducial Volume	Observed Ratio	Expected Ratio	Observed/Expected
5.0	0.424 ± 0.012	0.447 ± 0.008	0.947 ± 0.033
5.5	0.544 ± 0.012	0.595 ± 0.011	0.915 ± 0.028
6.0	0.727 ± 0.011	0.773 ± 0.015	0.941 ± 0.023
6.5	0.960 ± 0.005	0.982 ± 0.018	0.977 ± 0.019
7.0	0.990 ± 0.002	0.995 ± 0.019	0.995 ± 0.019

TABLE 5.8.: The ratio of the number of ^{12}B events inside the fiducial volume to the number of events inside the entire detector for various fiducial volume cuts. A value of the ratio of the observed to expected not equal to 1 indicates a bias in the vertex fitter.

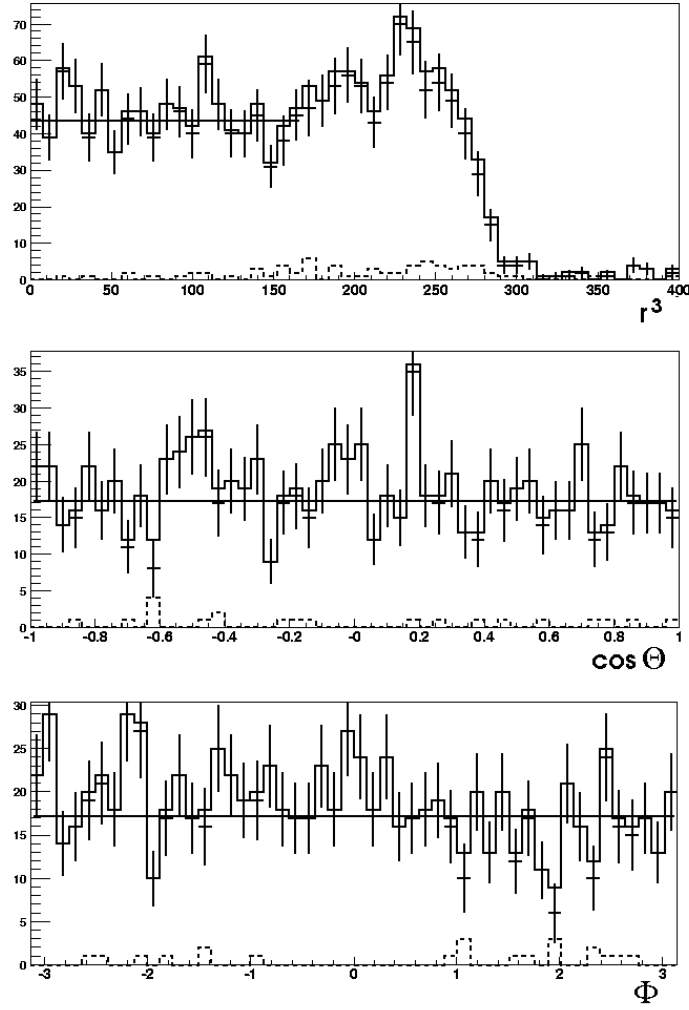


FIG. 5.17.: Event distributions in r^3 , $\cos \theta$, and ϕ for ^{12}B decays in the scintillator. The solid lines represent all events, dotted lines are backgrounds, and points with error bars are all events minus backgrounds [34].

5.3.4 Experimental Livetime (T)

Data from 152.9 detector live days (1.32×10^7 seconds) were analyzed in this study. The muon veto and shower veto cuts of 4 ms and 2 s, respectively, introduced dead-time into the measurement. Over the 152.9 days, 3.82×10^6 muons were vetoed in the inner and outer detector, resulting in 15,280 s deadtime. During the same period, 2.3×10^5 showers were vetoed, resulting in 4.6×10^5 s deadtime. The total experimental livetime is, therefore, 1.27×10^7 seconds. The systematic uncertainty in the livetime has been estimated to be 0.07% [15].

5.3.5 N_{signal}

The upper limit on N_{signal} has been evaluated in Ref. [44] for the case of known backgrounds between 0 and 5 events in 0.5 event steps. For our backgrounds, the upper limit on N_{signal} can be found by interpolation. The results of are shown in Fig. 5.18 for one observed event, as found in our solar $\bar{\nu}_e$ search. The interpolation is based on a second order polynomial fit of the form $p_0 + p_1x + p_2x^2$ with coefficients $p_0 = 4.367$, $p_1 = -1.088$, and $p_2 = 0.0083$. For one signal event in the presence of 0.90 expected background events, this yields and 90% C.L. upper limit of 3.17 signal events; however, this estimate does not account for the presense of uncertainty in the background estimate.

5.3.6 Calculation of the Flux Limit

Recall from section 5.1 that one event passed the selection criteria for inverse beta-decay in scintillator in the energy range expected for $\bar{\nu}_e$'s from ^8B ν_e conversion ($8.8 \text{ MeV} < E_{\bar{\nu}_e} < 17.0 \text{ MeV}$), and zero events passed the selection criteria in the energy range pertinent to the search for relic super nova neutrinos ($17.0 \text{ MeV} < E_{\bar{\nu}_e} < 30.0 \text{ MeV}$). In section 5.2, it was determined that the expected number of events from background processes should be 0.95 ± 0.45 and 1.72 ± 0.12 for the measurements of neutrinos from the sun and from relic super nova, respec-

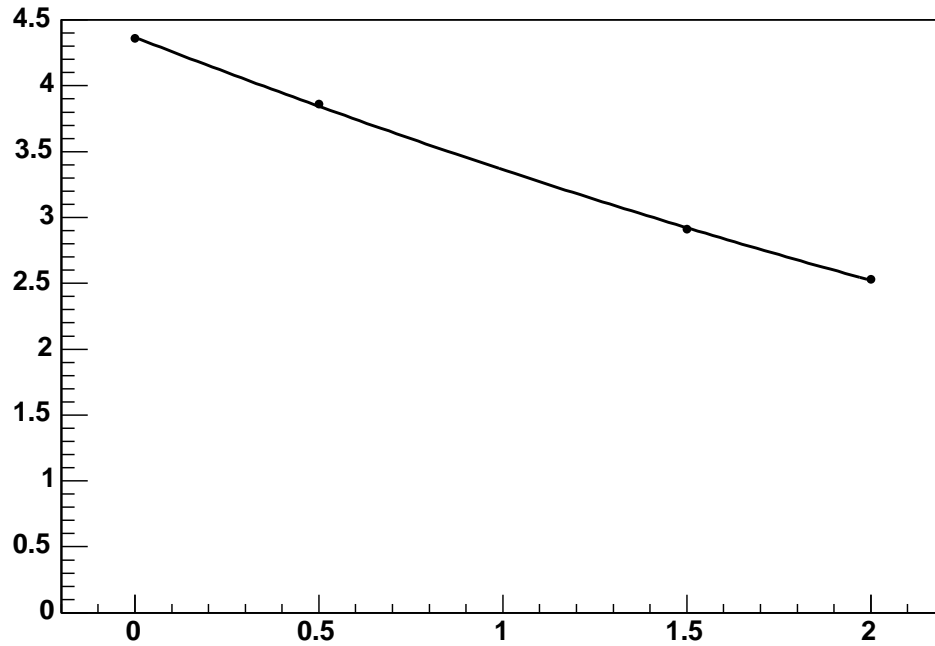


FIG. 5.18.: Points indicate the Feldman & Cousins 90% C.L. upper limit on number of signal events for one observed event in the presence of known background. The line represents a fit to a second order polynomial which is used to interpolate to this studies values of the expected background.

tively. The observed number of events is, therefore, consistent with the expected background, which implies the absence of signal events; however, due to the finite sensitivity of the detector we can only set an upper limit on the number of signal events, and hence the flux of $\bar{\nu}_e$'s. Two methods were used to derive the upper limit.

In the first method, a Monte Carlo technique was used to determine the upper limit on the $\bar{\nu}_e$ flux. In this technique it is assumed that the distributions of values obtained for $\bar{\sigma}$, $\bar{\epsilon}$, $N_p \times f_v$, and T by an ensemble of identical experiments would be Gaussian, with mean values equal to those obtained in sections 5.3.1, 5.3.2, 5.3.3, and 5.3.4, with widths equal to the estimated uncertainties in these quantities.

	Value	Uncertainty (%)
$\bar{\sigma}$ (cm ²)	7.94×10^{-42}	3.0
$\bar{\epsilon}$	0.856	2.45
$N_p \times f_v$	4.20×10^{31}	2.86
T (s)	1.27×10^7	0.07

TABLE 5.9.: Summary of quantities used in the calculation of the solar $\bar{\nu}_e$ flux and their uncertainties.

Table 5.9 summarizes the means and percent uncertainties in the quantities used for the flux calculation. The background estimates obtained in the ensemble are also assumed to be Gaussian with mean equal to our obtained value and width equal to the uncertainty in our estimate.

For each simulated experiment, a value for the background is taken from a Gaussian distribution with mean equal to the expected background and width equal to the uncertainty in the background. Using the results of section 5.3.5, the 90% upper limit on the number of signal events is determined. Values for $\bar{\sigma}$, $\bar{\epsilon}$, $N_p \times f_v$, and T are taken from Gaussian distributions as described above, and the upper limit on the flux for that simulated experiment is calculated according to eq. 5.19. A histogram is made of the upper limit on the flux for 100,000 experiments, and the value of the flux limit that is greater than that calculated in 90% of the simulated experiments is taken as the 90% upper limit on the flux of $\bar{\nu}_e$'s. Figure 5.19 shows the results of this calculation for the measurement of $\bar{\nu}_e$'s from ^8B ν_e transitions.

The flux limit resulting from the search for $\bar{\nu}_e$'s from the transition of ν_e 's from solar ^8B is $\phi_{\bar{\nu}_e} \leq 1.11 \times 10^3 \text{ cm}^{-2} \text{ s}^{-1}$. This represents a transition probability of $P(\nu_e \rightarrow \bar{\nu}_e) \leq 0.0914\%$ for solar ^8B ν_e 's with energies above 8.8 MeV. This improves on the previous limit by a factor of 9 [28].

A similar analysis has been completed for the search for relic super nova $\bar{\nu}_e$'s, with zero observed events. In this case, the flux of relic super nova neutrinos is

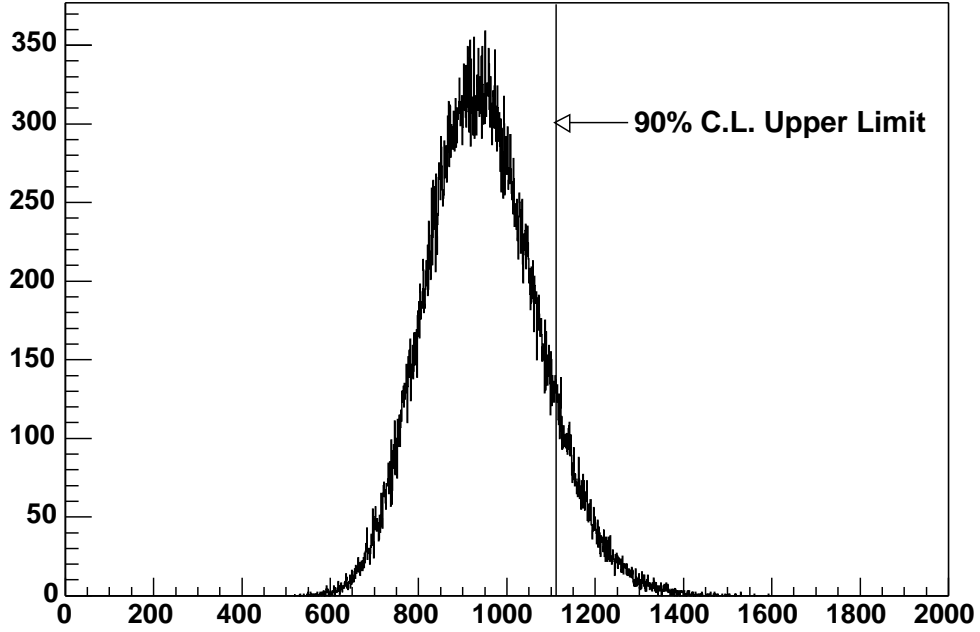


FIG. 5.19.: Histogram showing the flux limits obtained in 100,000 simulated measurements. The line at $1111 \text{ cm}^{-2} \text{ s}^{-1}$ indicates the value for which 90% of the experiments measure a smaller value.

found to be $\Phi_{\bar{\nu}_e} \leq 84 \text{ cm}^{-2} \text{ s}^{-1}$. This limit does not compete with the current best limit of $1.2 \text{ cm}^{-2} \text{ s}^{-1}$ reported in Ref. [25], which is based on 1496 days of data from the Super-Kamiokande detector; however, with longer livetime, KamLAND's sensitivity should become competitive in this search.

The limits produced using this method are considered to be very conservative since the 90% confidence level is applied twice—first to determine the limit on the number of signal events, and secondly when picking the value for which 90% of experiments measure a smaller flux. In order to more accurately determine the limit, a second method was developed [43] based on the calculation of upper limits reported in Ref. [44], with systematic uncertainties incorporated from Ref. [45], and modifications made in accordance with Ref. [46].

The probability of measuring n events for μ expected signal events in the presence of a known background of b events is given by the expression:

$$P(n|\mu) = \frac{(\mu + b)^n \exp[-(\mu + b)]}{n!}. \quad (5.21)$$

For each value of n , there is a value μ which maximizes the quantity $P(n|\mu)$. This value, μ_{best} , is required to be physically allowed (here, non-negative), and in this example has the value $\mu_{best} = \max(0, n-b)$. For a given value of μ , $P(\mu|n)$ and $P(\mu_{best}|n)$ are calculated over a range of values for n . The quantity

$$R = \frac{P(\mu|n)}{P(\mu_{best}|n)} \quad (5.22)$$

is calculated for each value of n . The acceptance interval is found by adding n 's to the interval in order of decreasing R until the sum of the $P(\mu|n)$ exceeds the confidence level desired (i.e. .90 for 90% C.L.). This process must be repeated over a range of μ large enough to include the upper and lower limits.

For example, for the known background $b=3$ events, we may consider the $\mu=0.5$, and determine the range of n consistent at the 90% confidence level. Table 5.10 indicates the resulting values for $P(n|\mu)$, μ_{best} , $P(n|\mu_{best})$, and R over a range of n .

According to the results listed in Table 5.10, values of n should be added to the interval in the order of $n=4,3,2,5,1,0,6,7,8,9,10,11$. The sum of $P(n|\mu)$ in the given order exceeds 90% after the 6th n is added, and includes the range $n=[0,6]$. The 90% confidence belt for n given $\mu=0.5$ and $b=3$ is, therefore $n=[0,6]$.

This calculation is repeated for a relevant range of μ to obtain the confidence belt the μ as a function of n . Once completed, the confidence interval for μ given a measured value of n is found by the intersection a vertical line which passes through n on the x-axis and the lower and upper limits on the confidence belt

n	$P(n \mu)$	μ_{best}	$P(n \mu_{best})$	R
0	0.030	0.0	0.050	0.607
1	0.106	0.0	0.149	0.708
2	0.185	0.0	0.224	0.826
3	0.216	0.0	0.224	0.963
4	0.189	1.0	0.195	0.966
5	0.132	2.0	0.175	0.753
6	0.077	3.0	0.161	0.480
7	0.039	4.0	0.149	0.259
8	0.017	5.0	0.140	0.121
9	0.007	6.0	0.132	0.050

TABLE 5.10.: Example calculation of confidence level belt for a Poisson distribution of $\mu=0.5$, and background $b=3$ [44].

plot. For a lower boundary of zero, the upper boundary represents an upper limit on the quantity μ .

In the case of KamLAND, the calculation is more difficult due to uncertainties in the background and in quantities used to calculate the flux. The expected number of events seen in KamLAND is given by:

$$\mu = \mu_s + \mu_b \quad (5.23)$$

where μ_s is the expected number of real $\bar{\nu}_e$ interactions and μ_b is the expected background. The quantity μ_s is related to the $\bar{\nu}_e$ flux by

$$\mu_s = \bar{\sigma} \times \bar{\epsilon} \times T \times N_p \times f_\nu \times \Phi \equiv z \times \Phi. \quad (5.24)$$

where the quantities have been defined in 5.3. The values of z and μ_b have been calculated in previous sections, and for the solar $\bar{\nu}_e$ measurement have the values:

$$z = (3.63 \pm 0.17) \times 10^{-3} cm^2 s \quad (5.25)$$

$$\mu_b = 0.95 \pm 0.45. \quad (5.26)$$

The number of observed events in KamLAND is expected to obey Poisson statistics, therefore, for a given value of z and μ_b , the probability of observing n events is given by

$$P(n|\Phi, z, \mu_b) = \frac{(z\Phi + \mu_b)^n}{n!} \exp[-(z\Phi + \mu_b)]. \quad (5.27)$$

The uncertainties in μ_b and z are represented by truncated Gaussians with the form:

$$p(\alpha|\bar{\alpha}, \sigma_\alpha) = \begin{cases} \frac{1}{\sqrt{2\pi}\sigma_\alpha} \exp[-(\alpha - \bar{\alpha})^2/2\sigma_\alpha^2] & \text{if } \alpha > 0 \\ 0 & \text{otherwise} \end{cases} \quad (5.28)$$

where $\alpha = \bar{\alpha} \pm \sigma_\alpha$ and α is z or μ_b . Since z and μ_b are determined independantly, this distribution can be used to build the likelihood function:

$$L(\Phi, z, \mu_b) = P(n|\Phi, z, \mu_b)P(z|\bar{z}, \sigma_z)P(\mu_b|\bar{\mu}_b, \sigma_{\mu_b}). \quad (5.29)$$

Typically, the parameters z and μ_b are integrated out, and the total probability distribution becomes:

$$P(n|\Phi) = \int_0^\infty dz \int_0^\infty d\mu_b P(n|\Phi, z, \mu_b)P(z|\bar{z}, \sigma_z)P(\mu_b|\bar{\mu}_b, \sigma_{\mu_b}). \quad (5.30)$$

The likelihood ratio can then be written:

$$R = \frac{\int_0^\infty dz \int_0^\infty d\mu_b P(n|\Phi, z, \mu_b)P(z|\bar{z}, \sigma_z)P(\mu_b|\bar{\mu}_b, \sigma_{\mu_b})}{P(n|\hat{\Phi}, \hat{z}, \hat{\mu}_b)P(\hat{\mu}_b|\bar{\mu}_b, \sigma_{\mu_b})P(\hat{z}|\bar{z}, \sigma_z)}, \quad (5.31)$$

where $\hat{\Phi}$, \hat{z} , and $\hat{\mu}_b$ are the values that maximize the denominator. The confidence intervals can then be calculated using the method described above for simple Poisson statistics with an exactly known background.

The results of the calculations are shown for the solar $\bar{\nu}_e$ analysis in Fig. 5.20 [43]. For the solar $\bar{\nu}_e$ search, upper limit obtained is $9.4 \times 10^2 \text{ cm}^{-2} \text{ s}^{-1}$. This

corresponds to a $P(\nu_e \rightarrow \bar{\nu}_e) \leq 0.077\%$. This improves on the previously reported limit by a factor of 10 [28].

For the relic supernova $\bar{\nu}_e$ search, the limit obtained is $7.4 \times 10^1 \text{ cm}^{-2} \text{ s}^{-1}$. This result does not compete with the previously reported limit of $1.2 \text{ cm}^{-2} \text{ s}^{-1}$ reported in Ref. [25].

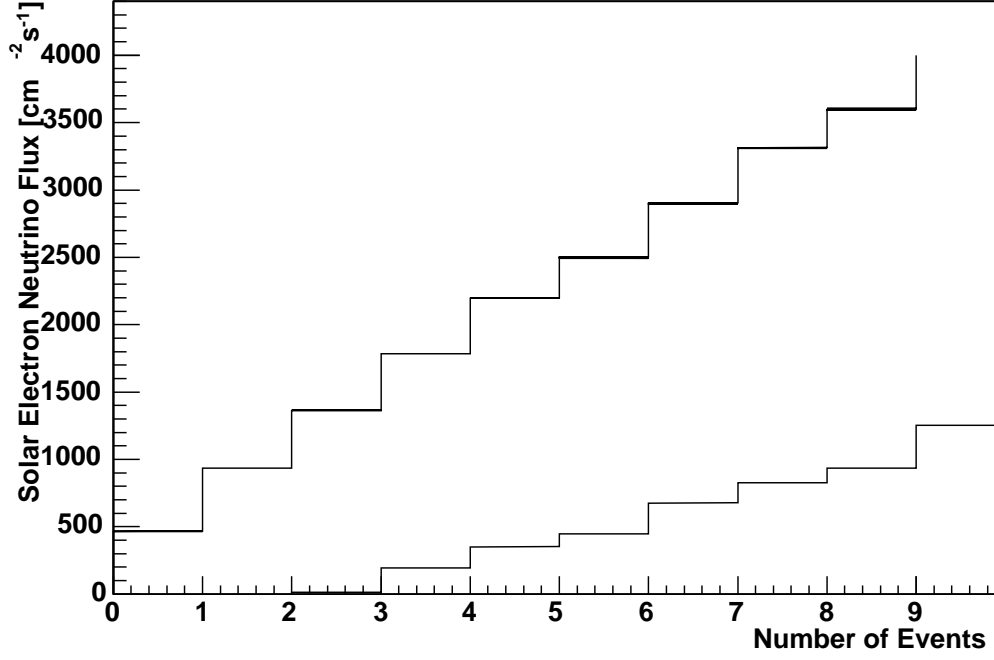


FIG. 5.20.: 90% confidence belts for the solar $\bar{\nu}_e$ calculated according to the method of Ref. [44], with statistical uncertainties included according to Ref. [45] and Ref. [46]. The observation of one events leads to an upper limit on the $\bar{\nu}_e$ flux of $\Phi_{\bar{\nu}_e} \leq 9.4 \times 10^2 \text{ cm}^{-2} \text{ s}^{-1}$.

CHAPTER 6

INTERPRETING THE FLUX LIMIT

In section 5.3.6, we obtained a limit many times better than the previous best limit on the flux of $\bar{\nu}_e$'s from the sun. This limit can be interpreted in the context of the physical models described in section 1.3.

According to the theory of resonant spin flavor precession discussed in section 1.3.3.1, the transition probability for $\nu_e \rightarrow \bar{\nu}_e$ is given by the following expression:

$$P(\nu_e \rightarrow \bar{\nu}_e) = 1.8 \times 10^{-10} \sin^2 2\theta_s \left[\frac{\mu_\nu}{\mu_B} B_\perp \left(\frac{0.05 R_s}{10 kG} \right) \right]^2. \quad (6.1)$$

The value of $\sin^2 2\theta_s$ is taken from the best fit to the solar neutrino oscillation parameters, which is found for $\sin^2 2\theta_s = 0.833$. Substituting these values along with the upper limit on the transition probability of 0.00077 obtained in section 5.3.6 into eq. 6.1, the upper limit on the product of the transverse magnetic field and the neutrino magnetic moment is:

$$\left[\frac{\mu_\nu}{10^{-12} \mu_B} B_\perp \left(\frac{0.05 R_s}{10 kG} \right) \right] \leq 2.4 \times 10^3 \quad (6.2)$$

This is a factor of 4 improvement on the previous best limit of 1.0×10^4 which was calculated in Ref. [26] based on the results of Ref. [28].

In section 1.3.3.2, the life time of ν_2 is related to the solar $\bar{\nu}_e$ flux by the equation:

$$P(\nu_e \rightarrow \bar{\nu}_e) = 0.328(1 - e^{-T/\tau}). \quad (6.3)$$

With $T = 500$ s is the lime of flight for neutrinos between the sun and the earth, and the lab frame life time τ is related to the rest frame lifetime of ν_2 by the relationship:

$$\tau = \frac{E_{\nu_2}}{m_{\nu_2}} \tau_{\nu_2}. \quad (6.4)$$

For the case of a quasi-degenerate neutrino mass scale with the neutrino mass of 1 eV, and neutrino energy on the order of 10 MeV (for ^8B neutrinos) and a $\nu_e \rightarrow \bar{\nu}_e$ transition probability ≤ 0.00077 , the rest frame life time of ν_2 is determined to be:

$$\tau_2 \geq 0.021 \text{ s/eV}. \quad (6.5)$$

This represents a factor of 200 improvement on the current limit of 10^{-4} s/eV.

CHAPTER 7

CONCLUSIONS

In summary, a high sensitivity search for astrophysical $\bar{\nu}_e$ has been conducted using 149 days of data from the KamLAND detector. The single candidate event found in the energy range relevant to a search for $\bar{\nu}_e$ from the transition of ^8B solar ν_e was found to be consistent with the expected background of 0.95 ± 0.45 events in the energy range of 8 - 16.2 MeV. The limit on the ^8B $\bar{\nu}_e$ flux in the energy range of 8 - 16.2 MeV was found to be $\phi_{\bar{\nu}_e} \leq 9.4 \times 10^2 \text{ cm}^{-2} \text{ s}^{-1}$, which corresponds to a $\nu_e \rightarrow \bar{\nu}_e$ transition probability of 0.00077 assuming no spectral deformation in the $\nu_e \rightarrow \bar{\nu}_e$ transformation. This new limit represents a factor of 10 improvement over the current best limit. The limit on the transition probability was used to improve the limit on the product of the neutrino magnetic moment and the transverse magnetic field in the sun by a factor of 4. The life time of the neutrino for non-radiative decays was improved by a factor 200 relative to the previous best limit.

The search for $\bar{\nu}_e$ with energies between 16.2 and 30 MeV from relic super nova yielded a flux limit of $\Phi_{\bar{\nu}_e} \leq 74 \text{ cm}^{-2} \text{ s}^{-1}$. While this limit does not compete with the current limit of $1.2 \text{ cm}^{-2} \text{ s}^{-1}$ reported in Ref. [25] after several years of operation, it does demonstrate the sensitivity of KamLAND to high energy $\bar{\nu}_e$'s, even with limited statistics.

APPENDIX A

WAVEFORM ANALYSIS

At the beginning of each run, pedestal values are taken for each PMT. Each pedestal consists of a 128 sample waveform that is acquired when no trigger conditions are met within the detector. Fifty pedestal waveforms are acquired for each PMT channel, and the average over the 50 waveforms is found in each of the 128 bins. This average pedestal waveform is subtracted bin by bin from each waveform that is acquired on that PMT channel during data taking.

Each waveform is then smoothed using a simple 3-point averaging technique to remove high frequency noise.

$$\phi_i = (\phi_{i-1} + \phi_i + \phi_{i+1})/3 \quad (\text{A.1})$$

After pedestal subtraction and smoothing, each waveform must be renormalized so that the baseline will lie at zero ADC counts before charge and time information can be extracted from the waveform. An trial and error method has been developed to determine a waveform's offset from the baseline.

1. The absolute value of each waveform channel (ϕ_s) is taken, and the sum over the 128 samples is calculated.

$$S_0 = \sum_{i=0}^{127} |\phi_i| \quad (\text{A.2})$$

2. The waveform is adjusted by a small amount, α , and the process is repeated.

$$S_j = \sum_{i=0}^{127} |\phi_i + \alpha_j| \quad (\text{A.3})$$

3. A minimum in the plot of S as a function of α is found.

$$S_{j-1} > S_j < S_{j+1} \quad (\text{A.4})$$

4. The value of α that minimized S is taken as the offset.

The trial and error method described above is effective but inefficient. A completely equivalent method was developed by an analytical evaluation of the previously described method. The offset is the value of α that minimizes the sum over the absolute value of the waveform samples:

$$\frac{\partial}{\partial \alpha} \left(\sum_{i=0}^{127} |\phi_i - \alpha| \right) = 0 \quad (\text{A.5})$$

which can be rewritten as

$$\frac{\partial}{\partial \alpha} \left(\sum_{n^+} (\phi_i - \alpha) + \sum_{n^-} (\alpha - \phi_i) \right) = 0 \quad (\text{A.6})$$

where n_+ and n_- indicate the indices for which $\phi_i - \alpha$ is positive and negative, respectively. Summing the α s gives

$$\frac{\partial}{\partial \alpha} (N_- * \alpha - N_+ * \alpha + \sum_{n^+} \phi_i - \sum_{n^-} \phi_i) = 0. \quad (\text{A.7})$$

Where N_- and N_+ are the number of samples for which $\phi_i - \alpha$ is negative and positive, respectively. Differentiating with respect to α results in the condition

$$N_- = N_+. \quad (\text{A.8})$$

The value of α that minimizes the area under the absolute value of the waveform is, therefore, the value for which $\phi_i - \alpha$ has the same number of negative samples as positive samples. This is true when α is equal to the median of ϕ_i .

In order to quantitatively evaluate the effectiveness of this method pedestal renormalization, the values of all 128 waveform samples are histogrammed for several hundred waveforms. Figure A.1 shows the results. Since the single photo-electron pulse, which dominates the pmt signals in the energy range of interest, spans only about 25% of the waveform, most of the entries in the histogram are due to bin-to-bin fluctuations of the baseline. The peak in the histogram, therefore, is composed of the baseline amplitudes. If the pedestal renormalization routine works perfectly, the peak will be centered on zero, since the number of positive and negative fluctuations will be the same. The value obtained using our technique for baseline renormalization is -0.4 ADC channels. A typical pulse spans ~ 30 bins, and produces an integrated charge of 300 charge units. Baseline renormalization will introduce approximately -8 charge unit bias (-3%) in the total integrated charge.

The final step in waveform analysis is the extraction of time and charge data. This is accomplished via a routine which has become known as the “contiguous area method”. In this method, after pedestal subtraction, smoothing, and pedestal renormalization, the points where the waveform crosses the zero baseline are identified. The integrals between every two consecutive crossings are calculated, and each positive area is stored as a potential photo-electron pulse. In order to distinguish between pulses due to positive fluctuations of the baseline, an artificial threshold is placed on the minimum area of a photo-electron pulse. This is accomplished by summing the areas of all the pulses which have positive integrals, and examining the relative contribution of each pulse to the total area. Figure A.2 shows the distribution of the ratio of individual pulse charge to total charge.

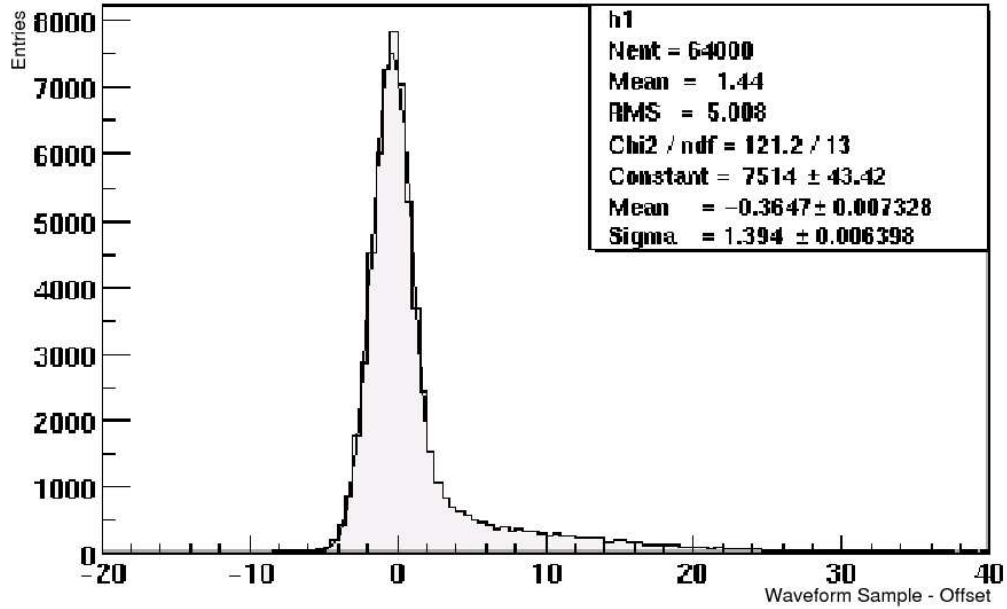


FIG. A.1.: The residual bias due to the pedestal renormalization scheme used in the KamLAND waveform analysis.

A waveform with a single photo-electron pulse with no positive baseline fluctuations will provide an entry at the value of 1 in Fig. A.2 since the ratio of the pulse charge to the total positive charge will be 1 to 1. Since we are dominated by single photoelectrons with only small fluctuations of the background, the distribution shows a cluster of events with ratio near 1. Small fluctuation, on the other hand, produce small charges relative to the sum of the entire waveform. As a result, the ratio for fluctuations of the baseline are clustered with ratios near zero. A naive fit of the distribution of baseline fluctuations to an exponential indicates that $> 99.9\%$ of all baseline fluctuations contribute less than 15% to the total positive area of a waveform. A cut of at least 15% of the total positive is, therefore, applied to each pulse to determine which are due to actual photoelectrons. Six well separated single photoelectron pulses can be identified using this method. Since the width of a pulse is usual ~ 30 channels, and a waveform

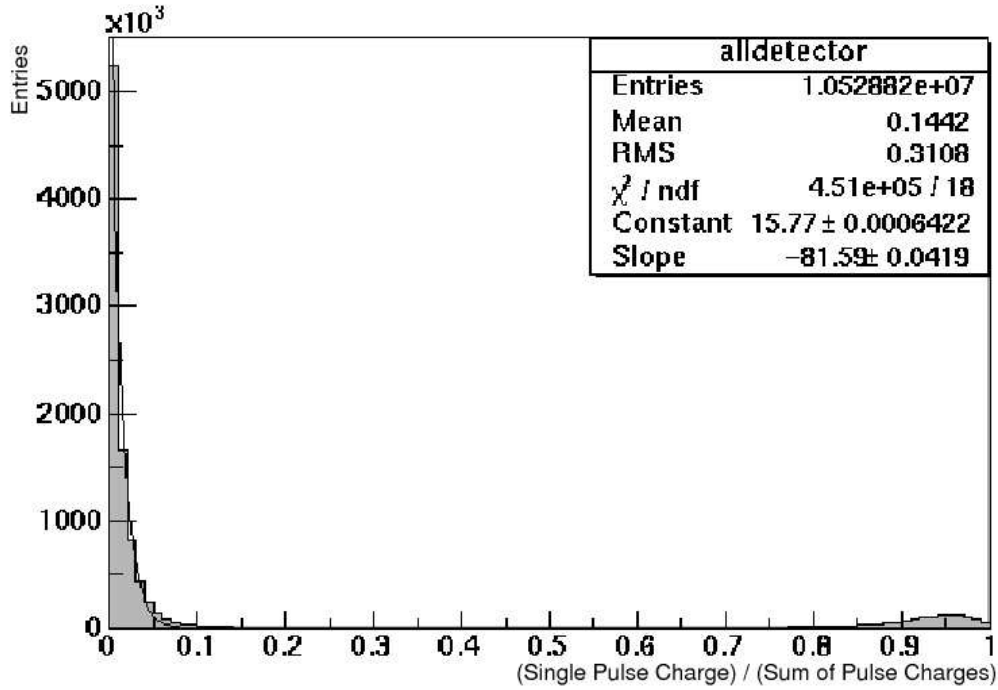


FIG. A.2.: The relative contribution of individual pulses within a waveform to the sum of all positive pulses.

contains only 128 channels, it is highly unlikely that more than 4 pulses could ever be non-overlapping in a single waveform.

Lastly, the pulse arrival time is taken as the bin number corresponding to the peak of a positive pulse, multiplied by the bin width in ns. The usual value for the bin width is ~ 1.5 ns, although this value is measured for each ATWD by digitizing a clock signal with known period, and comparing the period in time bins to the known period in ns.

APPENDIX B

GAMMA CALIBRATION SOURCES

The primary uses the KamLAND gamma sources are to set the energy scale of the detector, measure the detector's energy resolution, provide a means to check the Monte Carlo estimates of e/γ detection efficiency, and measure the effective e/γ pulse shape for n/γ discrimination. In addition, these sources are used to cross-check measurements of the detector linearity and position reconstruction, as well as measure the light transport properties of the scintillator. The design of these sources also takes into account the requirements on source integrity and ability to characterize the sources. In addition, the sources have been designed to allow convenient deployment on the fishline and 4π system.

Design choices have been made on the basis of detector simulation using GEANT3. For each isotope studied, the β and γ emission spectra were modeled in detail. In addition to the usual processes simulated by GEANT once the materials, geometry, and initial state particles are specified, scintillator light shadowing by the source materials was taken into account. The source was taken to be positioned at the center of the detector. In converting scintillation light to the number of detected photoelectrons, we assumed that the correspondence of PMT pulse height to number of photoelectrons is exactly known, and that an average of 150 photoelectrons are detected per MeV of energy deposited. Scintillator light quenching was not simulated as it was not expected to influence source design.

Given the intended use of the sources, we apply the following requirements to their design:

1. The detected energy spectrum of the source should have a simple structure in order to ease interpretation and limit systematics. More specifically, the sources should be effectively mono-energetic, and effects such as energy loss in the source (dead) materials and scintillator shadowing should not be so severe as to broaden or shift peaks significantly.
2. The sources should be adequately calibrated and characterized to allow tests of efficiency estimates at the few percent level. At the procurement level, we require that the contained activity of the source be known with an uncertainty not larger than 2%. For characterization, we require that the source has a geometry that allows ready testing in our counting setup.
3. The source energies should lie at several points spanning the energy range of interest. Further, the source energies should be chosen, where possible, to lie in regions where the energy spectrum and/or response of the detector varies rapidly.
4. For sake of source integrity, we require two things: First, the source should be doubly encapsulated with the outer layer of encapsulation being stainless steel or some other material which is inert in scintillator. Second, each source should be a $\beta - \gamma$ source, with the β 's kinetic energy deposited completely in the encapsulation. In this way, coincidence counting can be used to check for source leaks. The source capsule will be placed in a cell of liquid scintillator for some time, and then removed. The scintillator will then be measured for residual source material by using a germanium detector to detect the γ signal, and a PMT coupled to the scintillator cell to measure the energy deposited in the scintillator by β particles.

Isotope	Half-life	E_γ	Branching ratio	β endpoint	Mean free path
^{203}Hg	46.6 d	279.2	81.5%	212	8.4 cm
^{137}Cs	30.0 y	661.7	85.2%	1175	14.3 cm
^{65}Zn	244.1 d	1115.5	50.8%	1351	18.1 cm
^{60}Co	5.3 y	1173.2	99.9%	1491	
		1332.5	100.0%		20.2 cm

TABLE B.1.: KamLAND γ sources (energies in keV).

Four gamma sources have been selected. They are ^{203}Hg , ^{137}Cs , ^{65}Zn , and ^{60}Co . The principal gamma lines, endpoint energy, and half-life for each of these isotopes are listed in Table B.1. It should be noted that a neutron-moderated Am-Be source will provide additional calibration points at 4.439 MeV and 2.222 MeV. ^{65}Zn provides a calibration point near the minimum energy for inverse beta decay. Given the finite energy resolution of the detector, the trigger threshold for inverse beta decay should lie at 700–800 keV, and the ^{137}Cs source provides a calibration near this range. The combined energy of the ^{60}Co gammas lies near the peak of the prompt visible energy spectrum of inverse beta decay induced by reactor neutrinos and it also coincides with the upper end of the energy range for which terrestrial anti-neutrinos are expected to make a significant contribution. The ^{203}Hg source was chosen mainly for understanding the detector response at the lower end of the energy range of interest experimentally for detection of solar neutrinos. The energies of these sources are also well-spaced for linearity checks and probing a range of mean free paths (see Table B.1 for approximate values).

The nominal activity of each source is 500 Bq. Given the design of the front-end electronics and the mean occupancy, substantial statistics can be collected in a few minutes with little deadtime. Except for ^{203}Hg , this activity is very large compared to the global background singles rate expected from the detector. In the case of ^{203}Hg , a loose position cut can be applied, if necessary, to reduce the background rate to a manageable level. Another use of the gamma sources will be

to test the accuracy of the Monte Carlo simulation of e/γ detection efficiency by comparing measured source rates to Monte Carlo predictions. Toward this end, a requirement on the source fabrication is that the contained activity be calibrated to an accuracy better than 2%. Source characterization at UA will be used to check the integral of the contained activity and the effects of source materials on the emitted spectrum.

The detected energy spectrum from a source is unavoidably altered by gamma scattering from the encapsulation materials and shadowing of the scintillation light by the encapsulation and deployment system. The main problem then is to adequately control these effects so that the source requirements are met. In the source design, it was taken as given that double encapsulation was required to ensure source integrity. Given these constraints, we used simulation to investigate different choices for inner encapsulation material, outer encapsulation material, and overall geometry. The design we have chosen is shown schematically in Fig. B.1. The outer encapsulation is stainless steel, which provides mechanical strength, chemical inertness to scintillator, and β stopping power. The inner encapsulation is polyethylene, which is impervious to scintillator, and has a low density which results in little γ scattering. A $\sim 1 \text{ mm}^3$ bead of source material is implanted at its center. The wall thickness of the outer stainless steel encapsulation is 1 mm. The length of the capsule is large compared to its diameter in order to reduce the solid angle subtended by the endcap, which contains a large amount of stainless steel compared to the walls, thus reducing the number of γ 's scattered before leaving the source material. (A study has shown the average capsule thickness integrated over all solid angles is reduced by 30% compared with a design in which the inner capsule is 4 mm in length.) One end of the source capsule is machined and fitted with a stainless steel rod 10 cm long and 1 mm in diameter. This will have the appropriate fixture, yet to be designed in detail, for connecting to the deployment

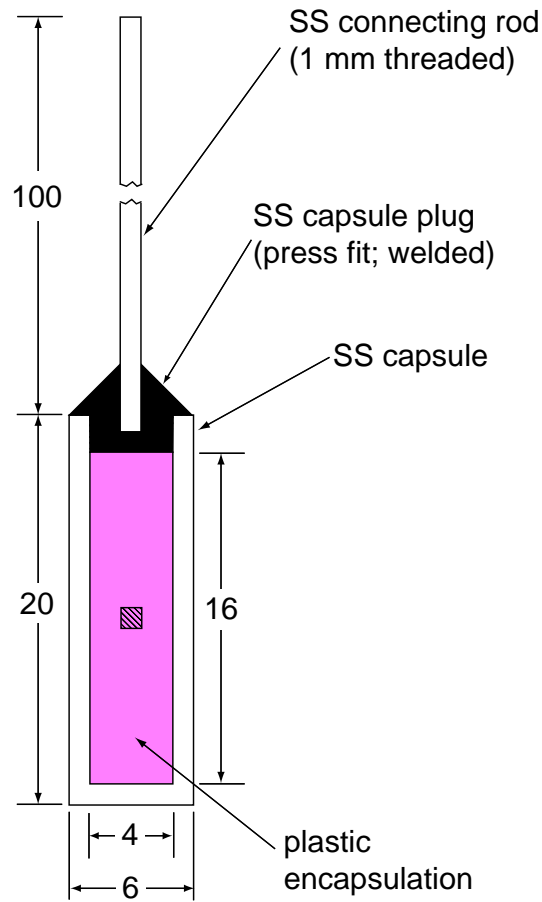


FIG. B.1.: Cutaway view of source capsule. Dimension units are mm.

system. The length of the connecting rod is constrained by the size of the shielded volume of the Ge detector that we will use for source characterization.

The spectra of the detected number of photoelectrons (taking into account all effects but light quenching in the scintillator and shadowing by the deployment system) are shown in Fig. B.2 for the sources positioned at the center of the detector. The spectra have the expected shape: a clear peak due to gammas practically unscattered by the source materials, a substantial tail on the low-energy side of the peak due to scattering in the source materials, and a small tail on the high-energy side due to residual penetration of betas which is essentially obscured by the energy smearing, and in the case of ^{65}Zn , a small high energy

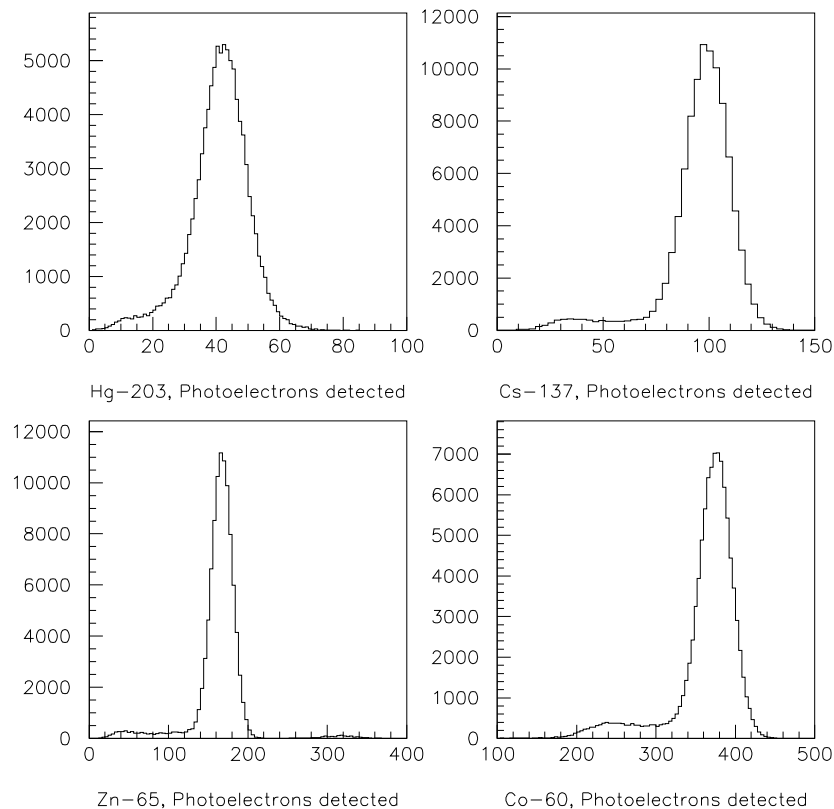


FIG. B.2.: Spectra of KamLAND gamma sources.

peak due to positron annihilation γ 's. Because of the small size of the sources, the effect of shadowing is small, much less than 1%.

Simulated spectra include 100000 events, which corresponds to only 200 seconds of data taking (at 100% efficiency), while still producing good statistics. As a measure of how much the peak is distorted by scattering one can fit a gaussian to the peak and compare its peak center, peak width, and area to the expected center, width, and number of unscattered events, respectively. The number of unscattered events can be determined from GEANT. We have fit the spectra with a gaussian and a background function to assess the accuracy to which the center, width, and peak statistics (% of events that are not scattered inside the source

capsule), can be determined. The results for one background function and set of fit ranges are shown in Table B.2. Systematics were studied by varying the background function and fit range. In all cases the results agreed with expectations to within 1.5% for center, 3.3% for resolution, and 3.0% for peak statistics, with the largest uncertainties occurring for ^{203}Hg . An example of a fitted spectrum is shown in Fig. B.3. The good agreement between the values taken from the gaussian fit and those expected indicates that the spectrum remains relatively easy to understand. Thus, the energy scale, energy resolution, and detection efficiency can be well modeled.

The effect of peak distortion on the determination of the energy scale can be studied in another way by using values obtained from the gaussian fit to calculate number of photoelectrons produced, and comparing that calculation to the number obtained by multiplying the source energy by 150 photoelectrons per MeV. The average number of photoelectrons produced by the energy deposit of a source can be calculated using the relationship:

$$N_{PE}^{SRC} = (center/\sigma)^2, \quad (\text{B.1})$$

which is valid if the width of the peak is due solely to photostatistics. The center is the center of a gaussian fit to the channel number spectrum and σ is the width of the gaussian. For our study, we fit the photoelectron spectra, and used eq. 1 to calculate the number of photoelectrons observed. Results are shown in Table B.2. In all cases except for ^{203}Hg , the energy scale can be determined by this method to better than the target accuracy of 2%. As for ^{203}Hg , its energy range is pertinent to the study of solar neutrinos; whether or not the same requirement on knowledge of energy scale applies as for reactor neutrinos has not been studied.

The sources were obtained from AEA Technology, and examined at the University of Alabama in order to confirm their calibrated contained activities, ensure

		Center	Resolution	f_p	N_{PE}^{SRC}
^{60}Co	fit	$375.50 \pm .07$	$19.43 \pm .06$	$.847 \pm .005$	373.5
	expected	375.90	19.39	.841	375.9
	% difference	.1	.2	.7	.7
^{65}Zn	fit	$167.40 \pm .05$	$13.05 \pm .04$	$.897 \pm .005$	164.5
	expected	167.40	12.94	.892	167.4
	% difference	.0	.9	.6	1.7
^{137}Cs	fit	$99.41 \pm .04$	$9.96 \pm .03$	$.897 \pm .005$	99.6
	expected	99.2	10.0	.893	99.2
	% difference	.2	.0	.4	.4
^{203}Hg	fit	$42.15 \pm .03$	$6.71 \pm .03$	$.820 \pm .005$	39.5
	expected	41.8	6.5	.802	41.8
	% difference	1.0	3.1	1.7	6.4

TABLE B.2.: Energy scale, resolution, and peak statistics (f_p) are compared for fit values and known values. The fit values shown were taken from a gaussian + 2^{nd} order polynomial, fit to the largest range studied.

the integrity of the encapsulation, and to check for the presence of unexpected lines in the sources' output spectra.

Leak testing was performed by exposing each source to scintillator composed of 2/3 mineral oil, 1/3 pseudocumene, and 1.5 g/L PPO. The sources were placed with scintillator in cylindrical acrylic cells with an outer (inner) diameter of 5.0 (3.8) cm, and a length of 3.4 (2.44) cm.

After varying exposure times, the sources were removed from the cells, which were then coupled to a two inch PMT, placed in front of a 5 inch Bicron NaI

Source	Half-life	Activity (Bq)	E_γ	Branching	β endpoint
^{60}Co	5.272 yr	509	1173.2	99.9%	318
			1332.5	100.0%	
^{65}Zn	244.1 d	521	1115.5	50.8%	330 (1.5%)
^{137}Cs	30.17 yr	578	661.7	85.2%	514

TABLE B.3.: University of Alabama sealed gamma sources. Energies are given in keV. Activities quoted are contained activities and were calibrated to $\pm 3\%$ at 95% C.L. on 1 July 2001 by AEA Technology.

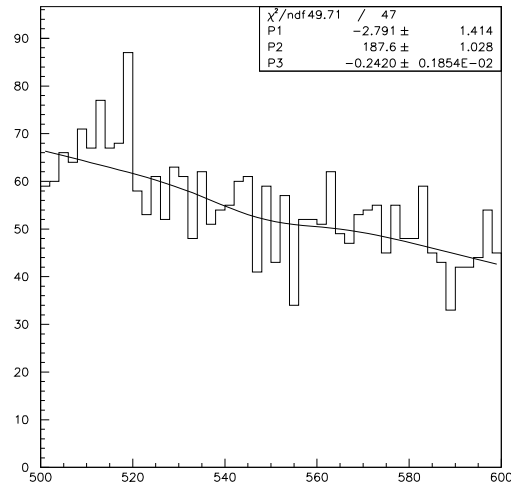


FIG. B.3.: The ^{137}Cs peak is fit with a gaussian, while the background is fit to a 2nd order polynomial. In this study, 2nd and 3rd order polynomials were used to fit the background, and the range of the fit was varied.

detector, and counted to search for decays of source activity that may have leaked into the scintillator from the sealed source. Since every ^{60}Co and ^{137}Cs decay produces an energetic β (see Table B.3) which will deposit most or all of its energy in the scintillator cell, a coincidence was required between the beta energy deposit in scintillator and the gamma energy deposit in NaI in order to reduce the background due to natural radioactivity and cosmics. For ^{65}Zn , β 's are only emitted in 1.5% of decays, therefore no coincidence was required and only NaI data is considered. Fig. B.4 shows a schematic of the counting setup.

The response of the NaI detector was measured using ^{60}Co , and ^{137}Cs calibrated plastic disk sources from Isotope products, and the KamLAND ^{65}Zn source. A large fraction of gammas which enter the NaI crystal are fully absorbed by the detector. The center and width of the full absorption line must be known to search for very small activities in the leak cell; therefore, the ^{137}Cs 662 keV line and the ^{65}Zn 1115 KeV line were fit with a gaussian + 1st order polynomial (to account

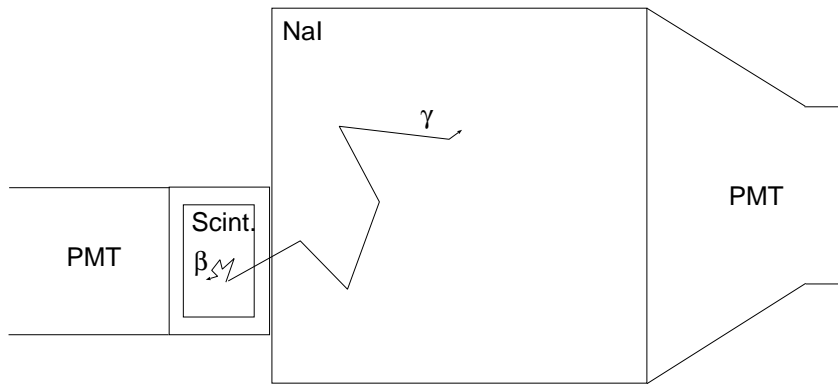


FIG. B.4.: Leak test experimental setup. A The setup is the same for both the coincidence and non-coincidence measurements, although no scintillator data is taken for the ^{65}Zn measurement.

for peak offset due to the compton scattered events under the peak) to find the center and width of their distributions. For ^{60}Co , the spectrum was fit to $g+g+p1$ in order to find the center and width of both the 1173 and 1332 keV lines (see Fig. B.5). Table B.4 shows the center and width obtained for each gamma full absorption line.

The threshold of the liquid scintillator must be known in order to calculate the detection efficiency for decays in the scintillator cell. To this end, ^{22}Na , ^{60}Co , and ^{137}Cs sources were placed near the cell and data was taken. The small size of the liquid scintillator cells results in compton spectra, the edge (corresponding to 180 degree backscattering of the incident gamma) of which was fit with a truncated gaussian in order to determine the detector response. For ^{60}Co , the

Source	E_γ	Center (channels)	Width (channels)
^{60}Co	1173.2	780.2	11.81
	1332.5	846.3	12.54
^{65}Zn	1115.5	1485	30.93
^{137}Cs	661.7	548.4	10.84

TABLE B.4.: NaI detector response for full absorption of gammas. Note that a different high voltage was used for the ^{65}Zn measurement.

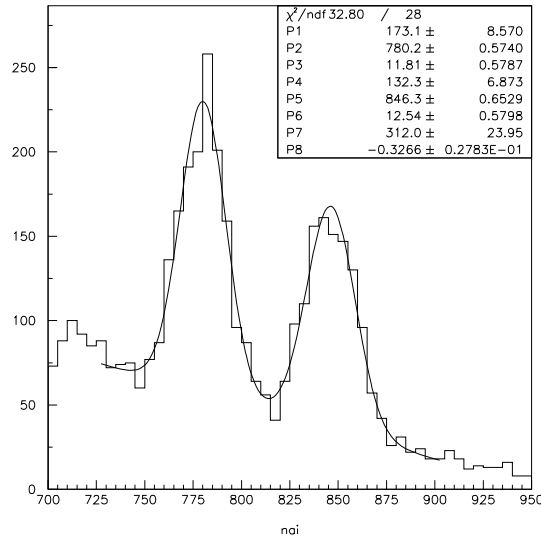


FIG. B.5.: The ^{60}Co spectrum was fit to a gaussian + gaussian + 1st order polynomial in order to find the center and width of the absorption lines.

source was placed between the liquid scintillator detector and the NaI detector and a coincidence was required for digitizing events. In this way, the 1332 keV compton spectrum was separated from the 1173 keV spectrum in the liquid scintillator cell by placing cuts on the NaI detector spectrum for the full absorption of the 1173 keV gamma, leaving only the compton scattering of the 1332 keV gamma in the liquid scintillator. The energy response of the liquid scintillator cells is shown in Fig. B.6. The energy threshold of the liquid scintillator detector was calculated as 258 keV.

The efficiency for detecting gammas in the NaI detector from decays in the scintillator was estimated using a Geant 3 based Monte Carlo. The full geometry shown in Fig. B.4 was included, and 50,000 decays were generated uniformly in the scintillator for each source. For ^{65}Zn , the efficiency was calculated by integrating a gaussian fit to the NaI full absorption peak and dividing by the number of events. For ^{60}Co and ^{137}Cs a minimum energy deposit of 258 keV is also required in the

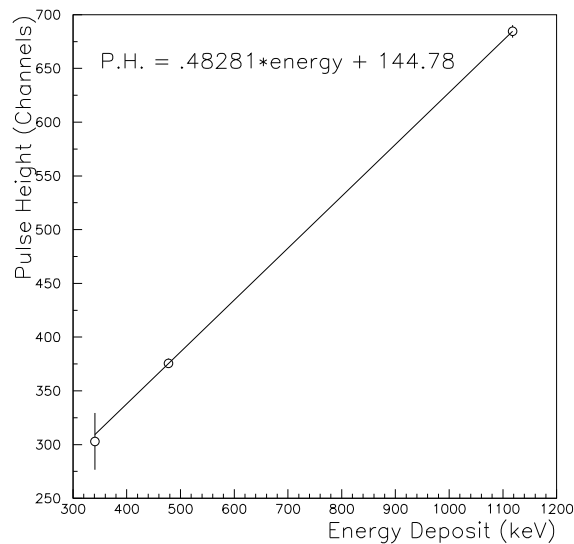


FIG. B.6.: The energy response of the liquid scintillator cells for backscattered 511 keV, 662 keV, and 1332 keV gammas with compton edges at 341 keV, 478 keV, and 1118.1 keV, respectively.

liquid scintillator, and for ^{60}Co both peaks are integrated. Detection efficiencies of 0.327%, 1.3%, and 0.796% are found for ^{60}Co , ^{65}Zn , and ^{137}Cs respectively. Since the β -endpoint energies of ^{60}Co and ^{137}Cs are small relative to the liquid scintillator threshold, the efficiency is reduced significantly by the coincidence requirement. This effect is responsible for the small detection efficiencies of ^{60}Co and ^{137}Cs relative to ^{65}Zn , which is based only on the NaI spectrum.

Leak cells were exposed to sources and then counted using a single NaI trigger in the case of ^{65}Zn , and a coincidence trigger for ^{60}Co and ^{137}Cs . Exposure times and counting times (see Table B.5) varied.

The NaI spectra obtained were fit with gaussians + 1st order polynomials, with the center and width of the gaussians fixed to those values obtained above (see Table B.4), and the amplitude was found. Fig. B.7 and Fig. B.8 show the

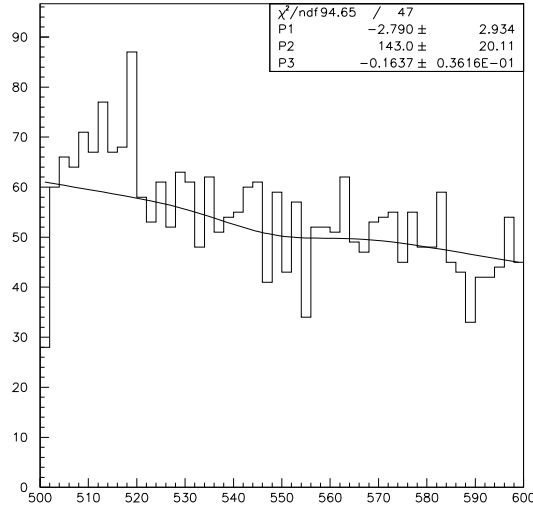


FIG. B.7.: The NaI fit to search for ^{137}Cs decays. P1 is the amplitude of the gaussian, P2 and P3 are coefficients of the polynomial intended to fit the background.

^{137}Cs and ^{60}Co fits. The amplitude and uncertainty in the fit amplitude were used to find the upper limit on the leak rate in the following way:

$$N_{\max} = \frac{\sqrt{2\pi} * A_{\max} * \sigma}{W} \quad (\text{B.2})$$

$$(\text{LeakRate})_{\max} = \frac{N_{\max}}{(\text{Count time (s)})(\text{Exposure time (d)})(\text{Efficiency (\%)})} \quad (\text{B.3})$$

where A_{\max} is determined from the amplitude and uncertainty in the amplitude of the gaussian using the Feldman - Cousins prescription described in Ref. [44], ΔA is the uncertainty in the amplitude, N_{\max} is the maximum number of events under the gaussian, σ is the width of the gaussian from Table B.4, and W is the bin width of the fitted spectrum. The results of these fits and the upper limits on the leakage rate of each source is given in Table B.6.

The maximum safe exposure time for the KamLAND detector can be calcu-

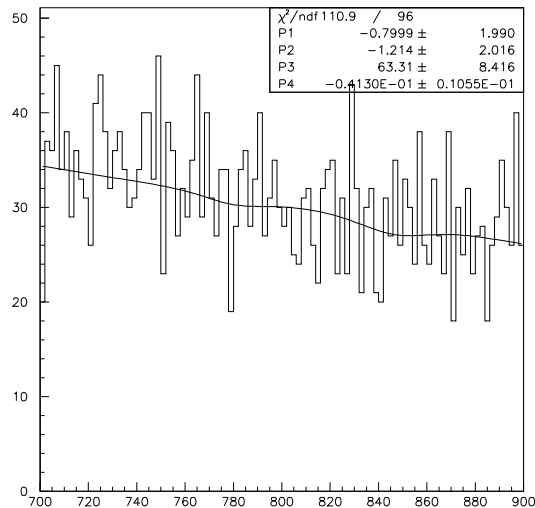


FIG. B.8.: The NaI fit to search for ^{60}Co decays. P1 is the amplitude of the first gaussian, P2 is the amplitude of the second gaussian, P3 and P4 are coefficients of the polynomial intended to fit the background.

lated based on the leak rates calculated here and given in Table B.6. Assuming that through source leakage we should add no more than 5% to the total singles rate at a given energy, then over the lifetime of the detector we should add no more than .25 Bq of activity from ^{60}Co and ^{65}Zn , and no more than 20 decays/day from ^{137}Cs . Based on this assumption, the maximum safe exposure times for ^{60}Co

Source	Exposure time (d)	Count time (s)
^{60}Co	7.066	526580
^{65}Zn	1.005	146634
^{137}Cs	15.79	526580

TABLE B.5.: Exposure time and counting times for the sealed sources. ^{60}Co and ^{137}Cs were exposed at different times to the same cell. The cell was counted only once.

Source	A	ΔA	A_{max} (95% C.L.)	W	L.R. _{max}
^{60}Co	-.79958	1.9820	3.13	2	7.88 mBq/day
	-1.2132	2.1047	3.01	2	
^{65}Zn	-0.05453	.1541	0.25	1	10.4 mBq/day
^{137}Cs	-2.790	2.934	3.34	2	685. $\mu\text{Bq/day}$

TABLE B.6.: Maximum leak rates for the KamLAND sealed gamma sources based on the Feldman & Cousins 95% C.L. interval for the gaussian amplitudes. For ^{60}Co , both peaks were fit and the sum was used.

and ^{65}Zn are 31.64 days and 24.04 days, respectively. For ^{137}Cs , the maximum safe exposure time is 8.1 hours with the current limits.

Addition testing of the ^{137}Cs was carried out using a high purity germanium detector to count a mild acid solution after exposure to the source. The source was soaked in 0.1 M HNO_3 for 20 hours. The 100 ml soad acid sample was counted using a calibrated low background germanium detector to detect the single 662 keV gamma emitted in the ^{137}Cs decay. The count time for the soak sample was 4.844 days.

The only peak which clearly exceeded the background was a line at 159 keV, which is shown in Fig. B.9. The time dependence of the rate of the peak was analyzed to determine its half-life, and its source. The half-life of 182 ± 85 days, combined with the energy of 159 keV, indicated that the peak may be due to surface contamination of ^{123m}Te ($T_{1/2} = 119.7$ days) which decays by emission of a 158.97 keV γ with an 84% branching ratio. This unexpected source of surface contamination is most likely the result of mis-handling of the source by the vendor who did the final source assembly. This contamination does not constitute a background for KamLAND since the energy is very low. However, it does indicate the need for careful testing of the KamLAND calibration sources for other sources of contamination.

The energy spectrum has been examined for contributions from 137 decays by fitting with a gaussian function with the center and width fixed to those of the

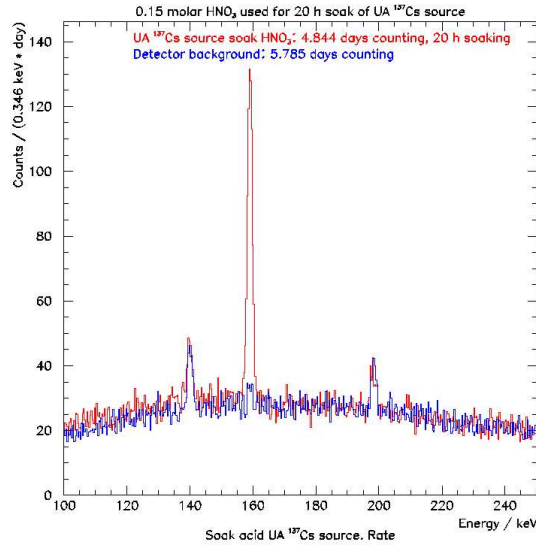


FIG. B.9.: The unexpected peak a 159 keV.

known ^{137}Cs peak. The results are shown in Fig. B.10. The fit indicates a strong likelihood for the presence of ^{137}Cs decays, and it was determined that an activity of 15 ± 4 mBq of 137 was present on the surface of the source. Analysis of the detector background showed no evidence for the presence of the 662 keV peak (see Fig. B.11).

The results of the acid soak tests indicate the presence of ^{123m}Te and ^{137}Cs in the soak acid samples. Although the ^{123m}Te signal is likely due to external contamination of the source capsule, it is unclear whether the ^{137}Cs signal is due to surface contamination (that could be cleaned), or due to leakage of the source material. The source of these signals can be determined by further cleaning and repeated counting. At present, the ^{137}Cs source is not deployed as a calibration source in KamLAND.

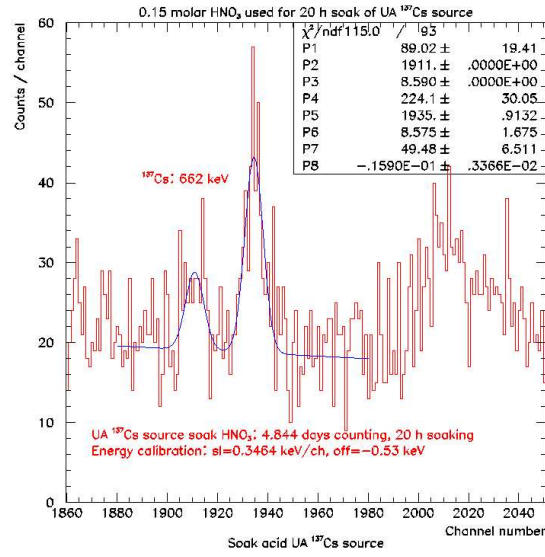


FIG. B.10.: The energy spectrum is fit with a gaussian with center and width fixed to the known values of ¹³⁷Cs.

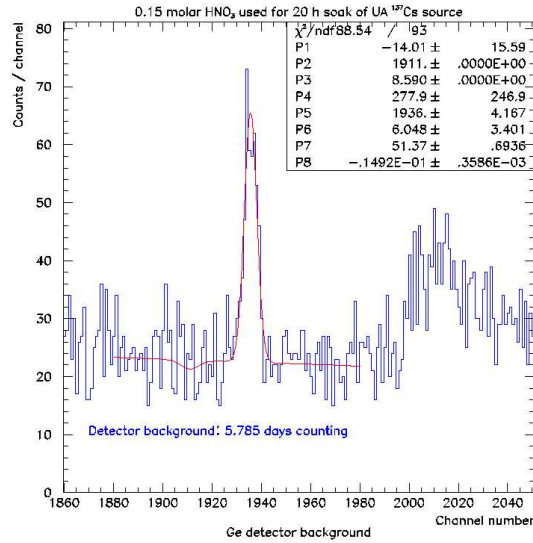


FIG. B.11.: The background energy spectrum is fit with a gaussian with center and width fixed to the known values of ¹³⁷Cs.

BIBLIOGRAPHY

- [1] <http://nucleardata.nuclear.lu.se/NuclearData/toi/>
- [2] C. Cowan *et al.*, Science **124**, 103 (1956).
- [3] J.-M. Danby *et al.*, Phys. Rev. Lett. **9**, 36 (1962).
- [4] J.F. Donoghue, E. Golowich, and B.R. Holstein, *Dynamics of the Standard Model* (Cambridge Univ. Press, New York, 1992).
- [5] G. Steigman, D.N. Schramm, and J.E. Gunn, Phys. Lett. **B66**, 202 (1978).
- [6] R. Davis, D.S. Harmer, and K.C. Hoffman, Phys. Rev. Lett. **20**, 1205 (1968).
- [7] P. Anselmann *et al.*, Phys. Rev. B **285**, 376 (1992).
- [8] A.I. Abazov *et al.*, Phys. Rev. Lett. **67**, 3332 (1992).
- [9] K.S. Hirata *et al.*, Phys. Rev. D **38**, 448 (1988).
- [10] S. Fukuda *et al.*, Phys. Rev. Lett. **86**, 5651 (2001).
- [11] Q.R. Ahmad *et al.*, Phys. Rev. Lett. **87** 071301 (2001).
- [12] J. Bahcall, M.H. Pinsonneault, and S. Basu, Astrophys. J. **555**: 990-1012, 10 July 2001.
- [13] R.C. Svoboda *et al.*, Nucl. Phys. **B38** (1995).
- [14] K.S. Hirata *et al.*, Phys. Lett. **B280**, 146 (1992).
- [15] Eguchi *et al.*, Phys. Rev. Lett. **90**, 021802 (2003).
- [16] F. Boehm *et al.*, Phys. Rev. Lett. **84**, 3764 (2000).
- [17] M. Apollonio *et al.*, Phys. Lett. **B466**, 415 (1999).

- [18] C. Arnaboldi *et al.*, hep-ex/0302021
M. Danilov *et al.*, Phys. Lett. **B480**, 12 (2000)
C. Tomei, A. Dietz, I. Krivosheina, and H.V. Kapdor-Kleingrothaus, Nucl. Instrum. Meth. **A508**, 343 (2003)
C.E. Aalseth *et al.*, hep-ex/0201021
H. Ejiri *et al.*, Phys. Rev. Lett. **85**, 2917 (2000).
- [19] K. Hagiwara *et al.*, Phys. Rev. D **66**, (2002).
- [20] D.N. Spergel *et al.*, astro-ph/0302209 (2003).
- [21] M. Mori *et al.*, Phys. Rev. D **48**, 5505 (1993).
- [22] J. Edsjo, hep-ph/9504205 (1995).
- [23] G.V. Domogatskii, Sov. Astron. **28**(1), (1984).
- [24] <http://www.to.infn.it/~giunti/NU/pap/0211462/node26.html>
- [25] M. Malek *et al.* hep-ex/0209028, (2002).
- [26] E.Kh. Akhmedov and J. Pulido, Phys. Lett. **B553**, 7, (2003).
- [27] C.-S. Lim and W.J. Marciano, Phys. Rev. D **37**, (1988) 1368.
- [28] Y. Gando *et al.*, hep-ex/0212067, (2002).
- [29] M. Aglietta *et al.*, JETP Lett. **63** No. 10, 791 (1996).
- [30] J.F. Beacom and N.F. Bell, hep-ph/0204111, (2002).
- [31] C.W. Kim and W.P. Lam, Mod. Phys. Lett. **A5**, 297 (1990).
- [32] <http://kamland.stanford.edu/~yoshiu/DTF>
- [33] D.M. Mei, Ph.D. thesis, University of Alabama, 2003.
- [34] <http://general.krl.caltech.edu/KamLAND/analysis/HEspall/>
- [35] P. Vogel, Phys. Rev. D **29**, 1918.
- [36] P. Vogel and J.F. Beacom, Phys. Rev. D **60**, 053003.
- [37] T.K. Gaisser, G. Barr, and S. Todor, Phys. Rev. D **38**, 85 (1988).

- [38] F.F. Khalchukov, A.S. Mal'gin, V.G. Ryassny, and O.G. Ryazhskaya, *Nuovo Cimento* **6C**, 320(1983).
- [39] <http://pdg.lbl.gov/2002/probrpp.pdf>
- [40] J.N. Bahcall *et al.*, *Phys. Rev. C* **54**, 411 (1996).
- [41] S. Ando, K. Sato and T. Totani, arXiv:astro-ph/0202450 v2 April, 2002
- [42] A. Kurylov, M.J. Ramsey-Musolf, and P. Vogel, hep-ph/0211306
- [43] G.J. Feldman and R.D. Cousins, *Phys. Rev. D* **57**, 3873 (1998).
- [44] B.F. Fujikawa, (unpublished).
- [45] J. Conrad, O. Botner, A. Hallgren, and C. Perez de los Heros, *Phys. Rev. D* **67**, 012002, (2003).
- [46] G.C. Hill, *Phys. Rev. D* **67**, 118101, (2003).